Research Square

Preprints are preliminary reports that have not undergone peer review.
They should not be considered conclusive, used to inform clinical practice,
or referenced by the media as validated information.

Neural stem cell loss of chromatin regulator Ankrd11 leads to hydrocephalus via ependymal and microglial cell dysfunction

Anastassia Voronova

voronova@ualberta.ca

University of Alberta https://orcid.org/0000-0001-7504-1905

Kara Goodkey

University of Alberta

Danyon Harkins

University of Toronto

Scott Yuzwa

University of Toronto https://orcid.org/0009-0004-6791-4445

Article

Keywords:

Posted Date: November 24th, 2026

DOI: https://doi.org/10.21203/rs.3.rs-11211242/v1

License: This work is licensed under a Creative Commons Attribution 4.0 International License.
Read Full License

Additional Declarations: There is **NO** Competing Interest.

Neural stem cell loss of chromatin regulator Ankrd11 leads to hydrocephalus via ependymal and microglial cell dysfunction

Kara Goodkey[1,2], Danyon Harkins[3], Scott A. Yuzwa[3], Anastassia Voronova[1,2,4-5*]

[1] Department of Medical Genetics, Faculty of Medicine & Dentistry, University of Alberta, Edmonton, AB T6G 2H7, Canada

[2] Women and Children's Health Research Institute, 5-083 Edmonton Clinic Health Academy, University of Alberta, 11405 87 Avenue NW Edmonton, Alberta, Canada, T6G 1C9

[3] Department of Laboratory Medicine & Pathobiology, Temerty Faculty of Medicine, University of Toronto, Toronto, ON M5S 1A8, Canada

[4] Department of Cell Biology, Faculty of Medicine & Dentistry, University of Alberta, Edmonton, AB T6G 2H7, Canada

[5] Neuroscience and Mental Health Institute, Faculty of Medicine and Dentistry, University of Alberta, Edmonton, Alberta, T6G 2E1, Canada

* Corresponding author – Dr. Anastassia Voronova (voronova@ualberta.ca)

Abstract

ANKRD11 (Ankyrin Repeat Domain 11) is a chromatin regulator that is frequently mutated in monogenic neurodevelopmental disorders. Here we show that conditional knockout of Ankrd11 in late embryonic neural stem and progenitor cells (Ankrd11^{nscKO}) results in progressive postnatal hydrocephalus. Ankrd11^{nscKO} ependymal cells show altered cell polarity, motile cilia function and gene expression. We further show that Ankrd11^{nscKO} brains display regional disease-associated microgliosis. Functional experiments demonstrate that ablation of microglia worsens, whereas attenuation of microglia activation improves hydrocephalus severity. Finally, we show that Ankrd11-deficient neural progenitor cells aberrantly communicate with microglia and increase their proliferation and activation. Thus, Ankrd11 deficiency in neural progenitor cells leads to abnormal ependymal and microglia cell functions, which contribute to hydrocephalus onset and severity. These results identify Ankrd11 as a critical regulator of ependymal and microglial cell biology and shed light on the mechanism of brain ventricle phenotypes in patients harbouring *ANKRD11* variants.

Introduction

Hydrocephalus (ventriculomegaly) is characterized by abnormal accumulation of cerebrospinal fluid (CSF) in the brain ventricular system (lateral, third, and fourth ventricles as well as cerebral aqueduct) and is often accompanied by progressive stretching of the surrounding brain tissue. When progressive hydrocephalus is not treated, ongoing ventricular enlargement and/or abnormal intracranial pressure can cause irreversible brain injury, severe disability, and in severe cases death (1-3). Hydrocephalus can be classified as obstructive (non-communicating) or non-obstructive (communicating) (4). Obstructive hydrocephalus is caused by a physical blockage within the ventricular system, such as aqueduct stenosis, resulting in increased pressure in the ventricles due to the accumulation of CSF (5, 6). The most common cause of non-obstructive hydrocephalus is aberrant formation and/or function of ependymal cells, though aberrant embryonic neurogenesis, congenital absence of microglia, viral infections, and brain injury have also been shown to contribute to this type of hydrocephalus (7-10).

Ependymal cells, which line the walls of the brain ventricular system forming a barrier between parenchyma and the CSF, and subventricular zone neural stem and progenitor cells (SVZ NPCs), located directly adjacent to the ependymal cells, share a common embryonic origin. Both ependymal cells and SVZ NPCs are derived from forebrain embryonic day (E)14-E16 radial glia (11-14). Ependymal cells in the brain lateral ventricles are the most well-characterized. In early postnatal development, these ependymal cells undergo several steps of multiciliogenesis to acquire multiple motile cilia, which beat in sync to distribute the CSF throughout the ventricular system (11, 15). Shortly after birth, immature ependymal cells display multiple motile cilia that are broadly dispersed across the apical cell surface (11). After postnatal day (P)5, the basal bodies of the motile cilia condense together and shift in polarity to be offset from the center of the ependymal cell (16). This drives cell orientation, also known as translational cell polarity (16-18). The rotational polarity ensures that the basal foot (anchoring structure of the cilium's basal body) of each individual motile cilium is oriented in the same direction; together, they drive the synchronized beating of cilia (19). Defects in ependymal cell formation, translational and/or rotational polarity cause disruptions in the coordinated beating of motile cilia, resulting in abnormal CSF flow and contribute to hydrocephalus onset (20-23).

SVZ NPCs, which maintain life-long neurogenesis and gliogenesis, project a single non-motile primary cilium into the CSF space (24, 25). The ependymal cells surround the ventricular end feet of SVZ NPCs in pinwheel-like arrangements permitting specialized apical signalling for SVZ NPCs and contributing to their structural and paracrine regulation (26, 27). In an aging brain or after a mild ependymal injury, some SVZ NPCs can form ependyma-like cells (28). Although SVZ NPCs exhibit limited, context-dependent ependymogenic capacity, there is currently no compelling evidence that endogenous SVZ NPCs substantially alter ventriculomegaly in hydrocephalus models. Consequently, their direct contribution to hydrocephalus severity or progression remains unresolved.

An important emerging mechanism in congenital hydrocephalus is chromatin dysregulation. Chromatin regulators contribute to the maintenance of the ventricular system by orchestrating developmental gene-expression programs, including ependymal differentiation and maturation. For example, pathogenic variants in *SMARCC1* and *CHD4* are associated with ventriculomegaly and/or hydrocephalus in human neurodevelopmental disorders, while conditional loss of *Smarca4* (Brg1) in mouse NPCs produces severe hydrocephalus, collectively implicating chromatin-regulatory pathways in ventricular homeostasis; however, the relevant cell types and molecular mechanisms remain incompletely defined (29-31). ANKRD11 (Ankyrin Repeat Domain 11), which controls global gene expression by interacting with histone deacetylases (HDACs), acetyltransferases (HATs) and nuclear receptors (32-34), is one of the most frequently *de novo* mutated genes in monogenic neurodevelopmental disorders (35). Brain structural anomalies in patients with pathogenic variants in *ANKRD11* include enlarged ventricles (36-41). However, the role and mechanism of Ankrd11 in ventricular homeostasis is not known.

Here, we identify a spatiotemporal mechanism linking *Ankrd11* loss in embryonic NPCs to progressive postnatal ventriculomegaly. *Ankrd11* deletion in E14.5 murine NPCs disrupts translational polarity and gene expression programs in NPC-derived ependymal cells. In parallel, *Ankrd11*-deficient SVZ NPCs exhibit aberrant immune gene expression *in vivo* and *in vitro* and activate microglia in co-culture. We further identify a region-specific, non-cell autonomous enrichment of activated microglia that correlates with hydrocephalus severity. Manipulation of microglia bidirectionally modifies disease severity: microglial ablation exacerbates, whereas microglial activity attenuation reduces hydrocephalus severity. Together, our findings reveal cell-

type specific roles for Ankrd11 in the development and maintenance of the brain ventricular system, linking ependymal dysfunction associated to hydrocephalus onset as well as aberrant SVZ NPC-microglial axis linked to disease severity. They further implicate SVZ NPCs as active contributors to hydrocephalus progression and provide mechanistic insight into ventricular abnormalities associated with *ANKRD11*-related neurodevelopmental disorders.

RESULTS

Knockout of Ankrd11 in E14.5 NPCs causes progressive postnatal hydrocephalus

To study how loss of Ankrd11 in NPCs affects brain ventricular system, we utilized a tamoxifen-inducible NPC-specific (NestinCre^{ERT2}) Ankrd11 conditional knockout (Ankrd11^{nscKO}) model as described in (42). Briefly, Ankrd11$^{fl/fl}$;RosaYFP$^{stop/stop}$ females, where exon 7 of *Ankrd11* and the stop cassette in the *Rosa* locus were both flanked by the loxP sites (42-44), were time mated with Ankrd11$^{fl/fl}$;RosaYFP$^{stop/stop}$;NestinCre^{ERT2} males, which expressed tamoxifen-inducible Cre in Nestin+ NPCs (42, 45). In this model, tamoxifen (TMX) injections induce Cre-mediate recombination in NPCs as well as their progeny (42, 45). Since ependymal cells and SVZ NPCs are specified from E14 - E16 forebrain NPCs (11-14), we injected TMX into pregnant dams at E14.5, giving rise to Ankrd11^{Ctrl} and Ankrd11^{nscKO} offspring (Fig. 1A). Fig. 1B confirms *Ankrd11* loss in E15.5 forebrain Ankrd11^{nscKO} NPCs, which were enriched via a primary neurosphere assay (46, 47). To confirm cell specificity, we immunostained Ankrd11^{WT} (Ankrd11$^{wt/wt}$;RosaYFP$^{stop/stop}$;NestinCre^{ERT2}; Fig. 1A), Ankrd11^{Ctrl}, and Ankrd11^{nscKO} embryonic forebrains for YFP and Sox2 (NPC marker (48)) 6h after TMX injection (Fig. S1A-B). As expected, Ankrd11^{Ctrl} did not express YFP (Fig. S1B-C). In Ankrd11^{nscKO} embryos, the density of YFP+ cells in the ventricular (VZ) and subventricular (SVZ) zones was comparable to Ankrd11^{WT} samples, with VZ displaying a higher YFP+ cell density compared to the SVZ in both genotypes (Fig. S1B, D). This is not surprising as VZ is primarily composed of Sox2+ NPCs (49). In agreement, ~94% of YFP+ cells in the VZ region and ~60-70% in the SVZ region of both Ankrd11^{nscKO} and Ankrd11^{WT} expressed Sox2 (Fig. S1F). Notably, the density of Sox2+ NPCs in VZ and SVZ of Ankrd11^{nscKO} forebrains was similar to Ankrd11^{WT} (Fig. S1E). Finally, none of the YFP+ cells overlapped with Iba1, a marker of microglia (50, 51), or IB4, a marker of endothelial cells (52) (Fig. S1C), both of which are derived from non-neuroepithelial sources

(53, 54). These results confirm *Ankrd11* knockout in NPCs as well as the NPC identity of the recombined cells.

Magnetic Resonance Imaging (MRI) of P15 Ankrd11^{Ctrl} (n=7) and Ankrd11^{nscKO} (n=10) brains revealed enlarged lateral ventricles with variable severity (Fig. 1C-E). Furthermore, Ankrd11^{nscKO} brains demonstrated decreased olfactory bulb size in comparison to Ankrd11^{Ctrl} (Fig. 1E, S1G), validating a finding we have previously reported in KBG syndrome mouse model and patients (42), while hippocampus volume was unchanged (Fig. S1H). To characterize ventricle abnormalities, we measured the total internal volume of the lateral ventricles as well as the caudal 3rd ventricles (d3V and v3V). On average, the lateral ventricles of P15 Ankrd11^{nscKO} mice were enlarged by ~41-fold (pvalue [p]=0.0086), whereas the 3rd ventricle was enlarged by ~1.6-fold (p=0.0028) compared to Ankrd11^{Ctrl} (Fig. 1E-G). Interestingly, lateral ventricle volume in the Ankrd11^{nscKO} mice segregated into 3 distinct groups with average volume of ~7 mm^3 (p=0.936; mild hydrocephalus, red triangle), ~53 mm^3 (~34-fold change, p=0.0028; moderate hydrocephalus, red square) and ~129 mm^3 (~83-fold change, p<0.0001; severe hydrocephalus, red diamond) compared to the Ankrd11^{Ctrl}, which had an average volume of ~2 mm^3 (Fig. 1F). Next, we measured brain area (mm^2) in the coronal plane for both rostral and caudal brain regions as shown in representative images in Fig. 1C-D. Ankrd11^{nscKO} mice displayed a significantly larger rostral (~1.2-fold change, p=0.005) and caudal (~1.3-fold change, p=0.001) coronal brain area compared to Ankrd11^{Ctrl} mice (Fig. 1H, J). Furthermore, both rostral (R^2=0.8060, p<0.0001) and caudal (R^2=0.8183, p<0.0001) coronal brain areas significantly positively correlated with the lateral ventricle volume (Fig. 1I, K). We also assessed rostral and caudal cortical thickness. Ankrd11^{nscKO} mice had significantly reduced rostral (~1.3-fold change p<0.0001) and caudal (~1.2-fold change, p=0.001) cortical thickness compared to Ankrd11^{Ctrl} mice (Fig. 1L, N). Caudal cortical thickness had a higher negative correlation with lateral ventricle volume (R^2=0.7823, p<0.0001) compared to the rostral cortical thickness (R^2=0.4466, p=0.0034) (Fig. 1M, O). To confirm that cortical thinning in the P15 Ankrd11^{nscKO} samples was not due to aberrant cortical neurogenesis, we assessed cortical tissues at E18.5, when cortical neurogenesis is largely completed (55). Fig. S1I-M shows that the density and cortical layer patterning of neuronal markers Satb2, Tbr1, and NeuN showed no significant changes between E18.5 Ankrd11^{nscKO} and Ankrd11^{Ctrl} rostral cortices. There was a small (~1.2-fold change, p=0.002) decrease in Ctip2+ neuronal density specifically in layer 5 of Ankrd11^{nscKO} cortex

compared to control (Fig. S1N). However, this small change in Ctip2+ cells did not lead to a thinner cortex in the Ankrd11^{nscKO} embryos (Fig. S1O). Taken together, these data indicate that postnatal cortical thinning in Ankrd11^{nscKO} mice results from mechanical tissue stretching due to enlarged ventricles rather than aberrant embryonic neurogenesis. This expansion of the postnatal cortex area and concomitant thinning of the postnatal cortex mimics the structural changes characteristic of other hydrocephalus models (56).

Next, we wanted to determine the onset of the hydrocephalus. We utilized postnatal caudal cortical area expansion and thinning as qualitative measures of hydrocephalus onset and severity (Fig. 1N-O). For example, mildly expanded caudal cortex was designated as mild hydrocephalus, significantly expanded caudal cortex as moderate hydrocephalus and overt swelling of the cortex accompanied by cortex collapse upon dissection as severe hydrocephalus (see Fig. S1P for representative images). At P3, Ankrd11^{nscKO} mice did not present with hydrocephalus (Fig. 1P). At P5, ~41% of Ankrd11^{nscKO} mice exhibited hydrocephalus with visible mild thinning of the caudal cortex. Starting from P7, hydrocephalus in Ankrd11^{nscKO} mice was >90% penetrant and showed progressive severity with age (Fig. 1P). At P7, ~42% Ankrd11^{nscKO} mice presented with mild, ~42% with moderate and ~10% with severe hydrocephalus (Fig. 1P). At P10-P15, ~24-26% of Ankrd11^{nscKO} mice showed severe hydrocephalus, while at P30 this proportion rose to ~57% (Fig. 1P). Notably, we observed partial lethality in Ankrd11^{nscKO} mice starting from P20 (Fig. S1Q). Importantly, none of the Ankrd11^{Ctrl} mice showed hydrocephalus or lethality at any timepoint. In agreement with MRI data, P10 and P15 Ankrd11^{nscKO} mice had significantly reduced rostral cortical column size (~1.2-fold change, $p=0.025$ and $p=0.0076$, respectively) compared to Ankrd11^{Ctrl} mice, with specific reduction in the cortical grey matter, but not corpus callosum (Fig. 1Q). Together, these data indicate that loss of Ankrd11 in E14.5 NPCs resulted in progressive postnatal hydrocephalus.

Ankrd11^{nscKO} mice exhibit decreased ependymal cell density and increased ependymal cell area

To determine the type and cause of hydrocephalus onset in the Ankrd11^{nscKO} mice, we first explored aqueduct stenosis, one of the most common causes of obstructive hydrocephalus (5, 6). Fig. S2A-D shows no change in the cerebral aqueduct diameter and area in P10 Ankrd11^{Ctrl} and Ankrd11^{nscKO} mice. We also injected Evans blue dye intracardially at P10 and

assessed Evans blue penetration in the ventricles and surrounding tissues. Both Ankrd11^{Ctrl} and Ankrd11^{nscKO} brains showed blue dye in the expected vascularized meninges and choroid plexus, with no difference in the pattern of dye in the brain parenchymal tissue (Fig. S2E). Moreover, we did not observe ependymal sloughing, which can contribute to obstructive hydrocephalus (57, 58), in Ankrd11^{nscKO} mice in MRI data as well as lateral ventricle whole mount and scanning electron microscopy assays (Figs. 1-2). Therefore, enlarged lateral ventricle formation in the Ankrd11^{nscKO} mice is not caused by aqueduct stenosis, ependymal sloughing, or blood brain barrier defects.

Next, we characterized the formation of ependymal cells as well as their cilia, as defects in ependymal cell and/or motile cilia formation are one of the most common mechanisms of non-obstructive hydrocephalus (56, 59, 60). Whole mount lateral ventricle wall preparations from P5 and P7 mice were immunostained for β-catenin (βcat) to label the apical cell boundary and γ-tubulin (γTub) to identify the basal body of cilia structures (20) (Fig. 2A-B). Ependymal cells located in the lateral ventricle have a large βcat+ apical area (>100 μm^2) and are multiciliated as identified by a cluster of multiple γTub+ puncta (Fig. 2B, arrowheads). At P5 (hydrocephalus onset; Fig. 1P), Ankrd11^{nscKO} samples showed a trending non-significant decrease in the density of ependymal cells compared to Ankrd11^{Ctrl} (Fig. S2F). This was accompanied by a slight trending non-significant increase in average apical area of ependymal cells in Ankrd11^{nscKO} samples (Fig. S2G). Binning of ependymal cells by cell size revealed a statistically significant reduction (~1.5-fold change, p=0.0025) in the proportion of small multiciliated ependymal cells (<150 μm^2) in Ankrd11^{nscKO} samples compared to Ankrd11^{Ctrl} (Fig. S2H). At P7 (~94% penetrance of hydrocephalus; Fig. 1P), there was a significant decrease in density of total ependymal cells (~1.7-fold change, p=0.0003) in the Ankrd11^{nscKO} lateral ventricle wall compared to Ankrd11^{Ctrl} (Fig. 2B-C). To understand whether decreased ependymal cell density was driven by cell death or ventricle enlargement, we immunostained samples for CC3 (cleaved caspase 3), a marker of apoptosis (61). Fig. S2J-K shows comparable density of CC3-positive cells in dorsal SVZ of Ankrd11^{nscKO} and Ankrd11^{Ctrl} mice at P5. Previous reports have demonstrated that ependymal cell area increases to accommodate larger ventricle size (62). In agreement, we observed a significantly increased mean apical ependymal cell area (~2-fold change, p=0.0078) in Ankrd11^{nscKO} mice compared to Ankrd11^{Ctrl} mice (Fig. 2D). Binning of P7 ependymal cells per area revealed a significant loss (~4-fold change, p<0.0001) of small (<150

μm^2) ependymal cells and a concomitant increase (~6-fold change, p=0.0011) in moderate size (301-450 μm^2) ependymal cells in Ankrd11^{nscKO} mice compared to Ankrd11^{Ctrl} mice (Fig. S2I). Together, these data demonstrate an overall decrease in ependymal cell density and concomitant increase in ependymal cell area in P7 Ankrd11^{nscKO} mice, which most likely arise due to enlarged ventricular wall area.

Ankrd11^{nscKO} mice exhibit aberrant ependymal cell polarity and motile cilia function

Next, we investigated the role of Ankrd11 in ependymal cell multiciliogenesis. In P7 lateral ventricle whole mount preparations, Ankrd11^{Ctrl} ependymal cells showed ~50 motile cilia per cell, in agreement with a previous report (63) (Fig. 2E). Surprisingly, we found no change in the number of motile cilia per ependymal cell in Ankrd11^{nscKO} samples when compared to Ankrd11^{Ctrl} (Fig. 2E). Using scanning electron microscopy (SEM), we assessed micrographs of the lateral ventricle wall from P10 Ankrd11^{Ctrl} and Ankrd11^{nscKO} brains. We observed no visible changes in the motile cilia ultrastructure between Ankrd11^{Ctrl} and Ankrd11^{nscKO} ependymal cells (Fig. 2F). However, there was a significant decrease (~1.4-fold change, p=0.0011) in the density of motile cilia bundles in Ankrd11^{nscKO} samples compared to Ankrd11^{Ctrl} (Fig. 2G), mirroring the decrease in the density of ependymal cells at P7 (Fig. 2C). Together, these data demonstrate that postnatal Ankrd11^{nscKO} mice display ependymal cells with larger apical areas but unchanged number of normal appearing motile cilia.

To characterize motile cilia formation and function in greater depth, we first analyzed the formation of ependymal cell cilia patch, or basal body (BB), which is tightly regulated during ependymal cell differentiation and maturation (16, 62). To assess changes in BB formation (cluster of γTub puncta), we further analyzed the P7 lateral ventricle whole mounts immunostained for βcat and γTub (Fig. 2H). The percent area of the BB within the total apical cell area was significantly increased (~1.3-fold change, p=0.0061) in Ankrd11^{nscKO} samples compared to Ankrd11^{Ctrl} (Fig. 2I). Next, we investigated ependymal cell planar cell polarity (PCP). PCP is the organization of motile cilia on the apical surface of ependymal cells; this coordinated orientation drives the synchronized beating of ependymal cell cilia and CSF flow throughout the ventricle (19, 20). There are two key aspects of PCP - rotational and translational polarity, both of which are critical for synchronous movement of the CSF (20). We explored

translational polarity by assessing the angle of orientation of the basal body (BB) patch in P7 whole mount preparations according to (20). The angle was determined by mapping the centroid of the apical surface and the centroid of the BB patch, a vector was applied to measure angle and distance between the two centroids (Figs. 2H, S2L). The length of the vector was not significantly different between P7 Ankrd11^{nscKO} and Ankrd11^{Ctrl} ependymal cells (Fig. S2M). Next, the average angle per image was calculated and denotated as 0°, each cell angle was then measured in relation to the relative 0° point for every image. A large majority (~81%) of BB patches in the Ankrd11^{Ctrl} were located within ±45° of the images relative 0°, whereas only ~54% of BB patches in Ankrd11^{nscKO} where within ±45° of the images relative 0° ($p<0.0001$) (Figs. 2J, S2N). This indicates a decrease in the coordinated orientation of the BB patch in Ankrd11^{nscKO} ependymal cells, which is indicative of disrupted translational polarity.

Changes in BB patch development and PCP formation in the ependymal cells of Ankrd11^{nscKO} mice prompted us to assess overall cilia function. We performed live imaging of the P6 *ex vivo* Ankrd11^{Ctrl} and Ankrd11^{nscKO} lateral ventricle wall tissue (64) (Fig. 2K). To track the flow generated by ependymal cilia beating we added a suspension of fluorescent beads to the mid rostro-caudal region of the lateral ventricle whole mounts and recorded bead movement and migration towards the rostral region of the lateral ventricle (Fig. 2K). Ankrd11^{Ctrl} ependymal cells directed the beads at an average velocity of ~3 μm/sec (Fig. 2L-M, Supplemental video S1). In contrast, beads added to the Ankrd11^{nscKO} lateral ventricle were propelled at a significantly slower (~2.8-fold decrease, $p=0.012$) average velocity of ~1.1 μm/sec (Fig. 2L-M, Supplemental video S2). Notably, there was no change in the relative direction of the bead flow between Ankrd11^{Ctrl} and Ankrd11^{nscKO} samples (Fig. 2N), further supporting deficient translational, but not rotational, polarity.

Taken together, these data indicate that ependymal cells in the Ankrd11^{nscKO} lateral ventricle fail to generate proper CSF flow due to aberrant motile cilia maturation and function, thus contributing to the hydrocephalus onset.

Ependymal cells in the Ankrd11^{nscKO} brain are transcriptionally distinct

Since Ankrd11 regulates global gene expression (34), we next asked whether ependymal cells in the Ankrd11^{nscKO} and Ankrd11^{Ctrl} samples are transcriptionally different. We subjected the microdissected P15 Ankrd11^{Ctrl} and Ankrd11^{nscKO} lateral wall containing ependymal layer and

lateral SVZ (herein referred to as snL-SVZ) as well as periventricular white matter containing dorsal ependymal layer, dorsal and dorsolateral SVZ as well as overlaying corpus callosum (herein referred to as snCC) to single nucleus RNA sequencing (snRNAseq) (Fig. S3). After filtering out low-quality nuclei, we retained a total of 76,139 nuclei, with 32,393 nuclei from two Ankrd11^{Ctrl} samples (no visible hydrocephalus) and 43,746 nuclei from two Ankrd11^{nscKO} samples (one with mild hydrocephalus and one with moderate hydrocephalus) in snL-SVZ dataset (Fig. S3A). Following the same processing pipeline, we retained a total of 24,863 nuclei, with 15,642 nuclei from two Ankrd11^{Ctrl} samples (no visible hydrocephalus) and 9,221 nuclei from two Ankrd11^{nscKO} samples (one with mild hydrocephalus and one with moderate hydrocephalus) in the snCC dataset (Fig. S3D). Since snL-SVZ and snCC datasets were obtained from different biological cohorts using slightly different kits (please see Materials and Methods for more details), snRNA-seq datasets were analyzed independently; concordant results across independent biological cohorts were interpreted as evidence of reproducibility.

Genes with high variability in expression between clusters were used to separate cell populations and visualized on uniform manifold approximation and projection (UMAP) graphs, which resulted in multiple clusters. To better characterize these populations, we grouped clusters sharing similar cell identities, defined by validated marker genes, and assigned a unified cellular label (Fig. S3A-B, D-E). In both datasets, we identified the expected cell populations including NPCs, neuroblasts, neurons, astrocytes, oligodendrocyte precursor cells (OPCs), oligodendrocytes, microglia, endothelial cells, epithelial and ependymal cells (Fig. S3A, D). Comparison of datasets revealed several population changes, including a decrease in the proportion of NPCs as well as an increase in the proportion of microglia in Ankrd11^{nscKO} samples compared to Ankrd11^{Ctrl} (discussed in more details below) (Fig. S3C, F). With regard to ependymal cells, snL-SVZ dataset showed a significant decrease in ependymal cells, from 437 ependymal nuclei in Ankrd11^{Ctrl} samples (representing 1.35 % of total Ankrd11^{Ctrl} nuclei) to 186 ependymal nuclei in Ankrd11^{nscKO} samples (representing 0.43 % of total Ankrd11^{nscKO} nuclei) (Table S1), corroborating our whole mount results (Fig. 2). Because the dorsal wall is smaller relative to the lateral wall, periventricular white matter tissue collection inevitably yielded a low proportion of ependymal cells, explaining their low number (44 in total) in the snCC dataset, which was insufficient for downstream analysis. Thus, we focused on snL-SVZ dataset to transcriptomically characterize the ependymal cells.

Ependymal nuclei were identified by known marker genes including (*Foxj1, Vim, Cfap44, Pifo, Dynlrb2* (65)) (Fig. 2O), subsetted and reclustered to investigate differences in transcriptomes. When graphed by genotype, ependymal nuclei segregated clearly between Ankrd11^{nscKO} and Ankrd11^{Ctrl} samples (Fig. 2P). Differentially expressed genes (DEG; padj <0.05, log2FC |1.5|) (Fig. 2R, S, and Table S1), clustered into mononuclear cell migration (*Ecm1, Nbl1, Dusp1*), inner ear development (*Calb1, H2-K1, Ptprq*), and carboxylic acid transport (*Folr1, Gfap, Slc25a21*) gene ontology categories (GO; Metascape (66)) categories (Fig. 2T). The inner ear development category is noteworthy as the genes in this category, such as *Ptprq*, are linked to stereocilia, which share mechanisms with ependymal motile cilia development and function (67-69). Together, our results suggest that loss of Ankrd11 in E14.5 NPCs significantly impairs ependymal cell maturation and gene expression program.

Ankrd11^{nscKO} SVZ NPCs display reduced density and elongated primary cilia

Next, we looked at the postnatal SVZ NPCs that reside in close proximity to ependymal cells. Using the P5 and P7 lateral ventricle whole mounts described above, we identified NPCs by a smaller (~50 μm^2) apical surface area and a single γTub+ puncta (marking the primary cilium) in the centre of the βcat+ border (63, 64) (Fig. 3A-B, arrowheads). Ankrd11^{nscKO} lateral ventricle whole mounts showed decreased NPC density (~3-fold change, p<0.0001) and increased size (~2.7-fold change, p=0.0003) at P7, but not at P5 compared to Ankrd11^{Ctrl} (Fig. 3C-F). When P7 NPCs were stratified by size, we observed a significant reduction in the proportion of smaller (<25 μm^2) (~3.3-fold change, p<0.0001) and an increase in the proportion of larger (>76 μm^2) (~13-fold change, p<0.0001) Ankrd11^{nscKO} NPCs when compared to Ankrd11^{Ctrl} (Fig. 3G). Next, we analyzed the NPC primary cilium, a structure that extends into the CSF as a cellular sensory organelle (25). To identify the primary cilia, we immunostained for the γTub+ basal body and Arl13b+ axoneme (70) (Fig. 3H). Analysis of the combined measurement of γTub and Arl13b length showed significant increases at P5 and P7 (~1.3-fold change, p=0.0026 and ~1.4-fold change, p=0.0002 respectively) of primary cilia length in Ankrd11^{nscKO} NPCs compared to Ankrd11^{Ctrl} NPCs (Fig. 3I-J).

To validate decreased NPC density, we cultured NPCs isolated from P15 Ankrd11^{Ctrl} and Ankrd11^{nscKO} dorsolateral and lateral SVZ as primary neurospheres (Fig. 3K). Every primary neurosphere arises from a single NPC, while ependyma, microglia, and other cells do not

survive, allowing for enrichment of SVZ NPCs (47). Moreover, this is a well-established assay for testing SVZ NPC pool size (47, 71). After 7 DIV (days *in vitro*), Ankrd11^{nscKO} neurospheres were significantly reduced in number (~7.9-fold change, p=0.0015) and diameter (~1.6-fold change, p<0.0001), as well as had an irregular shape when compared to Ankrd11^{Ctrl} (Fig. 3L-O). This corroborates the lower SVZ NPC density in Ankrd11^{nscKO} brain lateral walls (Fig. 3C). Together, these data demonstrate that the loss of Ankrd11 in E14.5 NPCs results in altered primary cilium length and decreased density of postnatal SVZ NPCs.

Ankrd11^{nscKO} SVZ NPCs aberrantly upregulate immune genes

To characterize the Ankrd11^{nscKO} SVZ NPCs transcriptionally, we first analyzed transcriptomes of Ankrd11^{Ctrl} and Ankrd11^{nscKO} NPCs from the snCC and snL-SVZ datasets. While both datasets showed a decrease in the proportion of NPCs (identified by expression of *Mki67, Egfr, Tox3*, and *Tead1* [(72-74); Fig. S3, Table S1]) in the Ankrd11^{nscKO} samples when compared to Ankrd11^{Ctrl}, there was a larger decrease in the proportion of NPC nuclei in the snCC compared to the snL-SVZ dataset (~3-fold [~12% to ~4% total nuclei] vs. ~1.3-fold [~8% to ~6% total nuclei] reduction, respectively) (Table S1). This corroborates decreased NPC density in P7 whole mount analysis as well as reduced number of primary neurospheres from P15 SVZ cultures (Fig. 3E, M). Ankrd11^{Ctrl} and Ankrd11^{nscKO} NPC nuclei were subsetted and reclustered in each dataset independently to investigate the transcriptional differences (Fig. 4A, C). Due to the large difference in NPC nuclei in snCC Ankrd11^{Ctrl} and Ankrd11^{nscKO} samples, we performed pseudobulk analysis on the NPC clusters between genotypes, which reduces the false positives caused by severely imbalanced nuclei (75). Comparison between Ankrd11^{nscKO} NPCs and Ankrd11^{Ctrl} NPCs showed 23 upregulated and 1 downregulated gene in the snCC dataset, and 17 upregulated and 4 downregulated genes in the snL-SVZ dataset (Fig. 4B, D, Tables S2, S3). NPCs from snCC and snL-SVZ datasets exhibited broadly similar gene expression patterns in Ankrd11^{nscKO} samples relative to Ankrd11^{Ctrl}, with NPCs in the Ankrd11^{nscKO} samples with moderate hydrocephalus exhibiting more pronounced changes when compared to Ankrd11^{nscKO} with mild hydrocephalus (Fig. 4E). Moreover, these changes were more apparent in the snCC dataset (Fig. 4E). Thus, while the direction of Ankrd11^{nscKO}-associated transcriptional NPC profiles was broadly shared across regions, its apparent magnitude was greater in the dorsal periventricular region. GO analysis of all NPC DEGs clustered in two general categories;

proinflammatory/microglia activation categories, including microglia pathogen phagocytosis (*C1qb, C1qc, Trem2*), activation of immune response (*Fyb1, Vav3, Arpp21*), and innate immune response (*Inpp5d, Ly86, Mrc1*), and cell development/function categories, including synapse organization (*Epha3, Tnc, Frmpd4*), regulation of endocytosis (*Ptx3, Mctp1, Epha3*), and regulation of cell population proliferation (*Cdkn1a, Runx1, Nell1*) (Fig. 4F, Tables S2, S3). Notably, expression of several inflammatory and immune related genes (e.g. *Trem2, C1qc, Ly86* (96, 113, 114)) was increased to a higher level in NPCs in Ankrd11^{nscKO} samples with moderate hydrocephalus when compared to Ankrd11^{nscKO} with mild hydrocephalus in both snCC and snL-SVZ datasets (Fig. 4E).

To corroborate these results, we subjected the P15 SVZ Ankrd11^{nscKO} and Ankrd11^{Ctrl} primary neurospheres to bulk RNA-sequencing (Fig. 4G). Principal component analysis (PCA) and correlation heatmap clearly segregated Ankrd11^{nscKO} and Ankrd11^{Ctrl} samples (Fig. S4). DEG analysis (padj <0.05, log2FC |1.5|) identified 1009 upregulated and 296 downregulated genes in Ankrd11^{nscKO} compared to Ankrd11^{Ctrl} samples (Fig. 4H, Table S4). GO analysis on significantly upregulated DEGs clustered into categories such as cilium movement (*Kif27, Cfap70, Cfap44, Dnah2*), cell projection assembly (*Mak, Daw1, Rac2, Itgb4*), and regulation of morphogenesis of an epithelium (*Esr1, Cdh1, Lcn2, Wnt2b*), which support our results showing abnormal primary cilia in these cells (Fig. 4I). Importantly, many upregulated DEGs clustered into categories related to neuroinflammation; including complement cascade (*C1qa, C1qb, C3, C1s1* (76, 77)), integrin cell surface interactions (*Col3a1, Col4a2, Itgax, Icam1* (78)), and inflammatory response (*Bmx, Cd38, Cmklr1, Clec4d, Oas1c, Irf7* (79)) (Fig. 4I). Downregulated genes clustered into regulation of nervous system process (*Egr2, Sox10, Grin2c, Tnr*), cell-cell adhesion (*Cdh1, Dab1, Itga2, Plxnb3*), cell migration (*Ackr3, Pdgfra, Enp2, Ccn4*) and regulation of neurogenesis (*Cdh1, Dscam, Egr2, Hey2, Heyl*) (Fig. 4I), supporting our previous publication demonstrating that Ankrd11 loss in E14.5 NPCs reduces SVZ NPC migration and olfactory bulb neurogenesis (42).

Together, these data show that loss of Ankrd11 in E14.5 NPCs leads to reduced numbers of postnatal SVZ NPCs, which surprisingly display aberrant expression of immune genes *in vivo* and *in vitro*. While our data do not exclude contributions of altered niche environment on SVZ NPC transcriptome, the persistence of immune-gene signature in Ankrd11^{nscKO} SVZ NPCs *in*

vitro suggests that Ankrd11^{nscKO}-associated immune gene expression is retained outside of the *in vivo* SVZ microenvironment and includes a cell-intrinsic component. We were particularly intrigued by the upregulation of immune related genes in Ankrd11-deficient NPCs. While NPCs can acquire aberrant immune gene signatures in models of viral infections and neurodegenerative disorders (80-82), to our knowledge, aberrant immune gene activation in NPCs in the context of a neurodevelopmental disorder has not yet been reported. We thus hypothesized that Ankrd11^{nscKO} mice may display aberrant neuroinflammation.

Hydrocephalus severity in Ankrd11^{nscKO} mice correlates with periventricular microgliosis

Neuroinflammation in hydrocephalus can be mediated by aberrant activation of microglia (83-86), which are derived from the yolk sac, migrate into the embryonic brain at E8.5-E9.5 and extensively proliferate to populate postnatal brain parenchyma (53, 87-89). After P7-9, these developmental microglia adopt a homeostatic state, which is characterized by continuous surveillance of the brain tissue for pathogens and injury (90, 91). In response to injury, disease or inflammatory environment, microglia become activated. A subset of these activated cells transitions into a disease-associated microglia (DAM) state defined by a specific transcriptional program that downregulates homeostatic genes and upregulates genes involved in phagocytosis, lysosomal function, lipid metabolism, and inflammatory signalling (89, 92, 93).

To assess changes in microglia in a spatiotemporal manner, we immunostained a range of early postnatal tissues (P5, P10, P15) and regions surrounding the lateral ventricle for Iba1, a microglia marker (Fig. 5A-B). First, the density of microglia in Ankrd11^{Ctrl} brains was stable from P5-P15 in the dorsolateral SVZ (DL-SVZ) as well as the region encompassing dorsal SVZ and adjacent corpus callosum (herein referred to CC), while slightly decreased in the lateral SVZ (L-SVZ) and steadily increased in the rostral grey matter (GM) (Fig. 5C), in agreement with previous reports (87, 94). In P5 Ankrd11^{nscKO} mice, a timepoint with mild partially penetrant hydrocephalus (Fig. 1P), there was no significant change in the density of Iba1+ cells in any of the Ankrd11^{nscKO} regions compared to Ankrd11^{Ctrl} (Fig. 5C). In contrast, at P10, a timepoint with highly penetrant mild to severe hydrocephalus (Fig. 1P), there was an increase in the density of Iba1+ cells in all Ankrd11^{nscKO} periventricular regions (CC, L-SVZ, and DL-SVZ), however, it reached statistical significance only in the CC region (~2.7-fold change, p=0.040) (Fig. 5C). By

P15, when majority of Ankrd11^{nscKO} mice showed moderate or severe hydrocephalus (Fig. 1P), all Ankrd11^{nscKO} periventricular regions had a significant increase in Iba1+ density (~4.2-fold change, p=0.0001, ~3.0-fold change, p=0.042 and ~2.3-fold change, p=0.004 respectively) compared to Ankrd11^{Ctrl} (Fig. 5C). Notably, Ankrd11^{nscKO} cortical GM did not show any changes in Iba1 density at any of the time points (Fig. 5C). Thus, increased microglia density in Ankrd11^{nscKO} periventricular regions starts after the hydrocephalus onset.

Next, we immunostained the postnatal brain sections for Dectin1 (Clec7a), which is expressed in both early (developmental) proliferation-associated microglia and disease-associated microglia (90, 92) (Fig. 5B). The density of Dectin1+Iba1+ cells decreased in the CC, DL-SVZ, and L-SVZ of Ankrd11^{Ctrl} mice after P10 (Fig. 5D), similar to previous reports that showed a sharp decline in Dectin1 signal in corpus callosum after P7 (90, 95). In contrast, Ankrd11^{nscKO} mice showed increased periventricular density of Dectin1+Iba1+ cells in a spatiotemporal manner. Specifically, there was a significantly higher density of Dectin1+Iba1+ cells in DL-SVZ of P5 Ankrd11^{nscKO} mice when compared to Ankrd11^{Ctrl} (~2.5-fold change, p=0.014), while CC and L-SVZ regions displayed comparable densities in both genotypes (Fig. 5D). At P10 and P15, Ankrd11^{nscKO} mice showed a significantly increased density of Iba1+Dectin1+ cells in all periventricular regions when compared to Ankrd11^{Ctrl} (>7.4-fold change, p<0.036) (Fig. 5D). Notably, there was no or minimal Dectin1+ signal in P5-P15 Ankrd11^{Ctrl} and Ankrd11^{nscKO} rostral cortical GM, which did not significantly differ between the two genotypes (Fig. 5D).

Together, these data indicate that Ankrd11^{nscKO} mice displayed elevated microglia density and Dectin1 immunoreactivity in periventricular regions in a spatiotemporal manner, with dorsal periventricular regions correlating most strongly with the Ankrd11^{nscKO} age and hydrocephalus severity.

Microglia in the Ankrd11^{nscKO} brain are transcriptionally activated

To capture unbiased transcriptomic changes in periventricular microglial cell populations, we analyzed microglia in snL-SVZ and snCC datasets. Microglia in both datasets were identified by the abundant expression of classical microglia markers *Cx3cr1, Csf1r,* and *P2ry12* (96) (Fig. S5A, D). There was a ~1.4-fold (~4% Ankrd11^{Ctrl} nuclei vs ~6% Ankrd11^{nscKO} nuclei) and ~2.3-fold (~8% Ankrd11^{Ctrl} nuclei vs ~18% Ankrd11^{nscKO} nuclei) increase in the proportion of

454 microglia nuclei in the Ankrd11^{nscKO} snL-SVZ and snCC samples, respectively, compared to
455 Ankrd11^{Ctrl} (Fig. S3, Table S1), corroborating our immunohistochemistry findings (Fig. 5B-C).
456 Ankrd11^{Ctrl} and Ankrd11^{nscKO} microglia nuclei were subsetted and reclustered in each dataset
457 independently to investigate the transcriptional differences (Fig. 5E, H). Clusters were defined by
458 co-expression of known homeostatic (*Tmem119, P2ry12, Csmd3, Selplg, Sparc*), and activated
459 (*Apoe, Ctsb, Spp1, Igf1, Gpnmb)* microglia markers (92, 97) (Fig. S5B, E). The heatdot plots in
460 Fig. S5C and S5F show the visible shift in marker gene expression from the homeostatic
461 ("Homeo") to moderately activated ("Active") to the highly activated DAM clusters in snL-SVZ
462 and snCC microglia. The bulk of Ankrd11^{Ctrl} microglia identified as homeostatic (~79% in snL-
463 SVZ and ~88% in snCC), with only a few microglia identified as DAM (~0.2% in snL-SVZ and
464 ~0.8% in snL-CC) (Fig. 5F-G, I-J). In contrast, only ~44% and ~18% of Ankrd11^{nscKO} microglia
465 were identified as homeostatic in snL-SVZ and snCC datasets, respectively (Fig. 5F-G, I-J).
466 While a large proportion of Ankrd11^{nscKO} microglia were activated in both datasets, the snCC
467 showed a higher proportion of activated microglia (~46%) compared to snL-SVZ (~33%) dataset
468 (Fig. 5F-G, I-J). The remaining microglia represented DAM clusters, which were almost
469 exclusively populated by Ankrd11^{nscKO} nuclei in both snCC (~36%) and snL-SVZ (~23%)
470 datasets (Fig. 5F-G, I-J). Across both datasets, Ankrd11^{nscKO} mice with moderate hydrocephalus
471 showed a greater proportion of DAM than Ankrd11^{nscKO} mice with mild hydrocephalus (Fig. 5G,
472 J). This difference was most pronounced within the snCC dataset, where ~43% of microglia in
473 Ankrd11^{nscKO} moderate hydrocephalus localized to the DAM clusters, compared to ~29%
474 microglia from Ankrd11^{nscKO} mild hydrocephalus; while proportions in the Ankrd11^{nscKO} snL-
475 SVZ dataset showed ~40% and ~6% DAM, respectively (Fig. 5G, J).

476 A total of 113 DEGs (padj <0.05, log2FC |1.5|) were identified between Ankrd11^{nscKO} and
477 Ankrd11^{Ctrl} snCC microglia, with 101 genes upregulated and 12 genes downregulated in the
478 Ankrd11^{nscKO} samples (Fig. 5K; Table S5). Notably, ~20% of the upregulated DEGs (21 DEGs)
479 clustered into inflammation related categories (Fig. 5K-L). Some of these genes (*Apoe, Gpnmb,*
480 *Spp1, Csf1, Ctsb*) have previously been identified in pro-inflammatory DAMs in rodent models
481 of neurodegenerative disorders such as Alzheimer's (92) and stroke (98). Other key gene
482 ontology categories included import into cell (*Dab2, Itsn1,* and *Lilrb4a*), phagocytosis-related
483 genes (*C3ar1, Cd63, Gpnmb,* and *Spp1*), lipid processing genes (*Lpl, Apoe, Plin2*, and *Nampt*),
484 and migration-related genes (*Csf1, Gas6,* and *Ripor2*) (Fig. 5L) (92, 99). In contrast, DEG

analysis between microglia populations from the snL-SVZ dataset, which displayed persistent but milder microglia activation, identified only 27 DEGs (Fig. S5G). From this list, 23 genes overlapped with snCC DEGs leading to identification of similar GO categories including endocytosis (*Gas7, Itsn1, Mrc1, Reps2*), cell development-related genes (*Igf1, Il7r, Plxnc1*), cell migration-related genes (*Hpse, Myo5a, Sash1*) (Fig. S5H). In agreement with milder microglia activation based on immunohistochemistry results (Fig. 5B-D), only a few pro-inflammatory genes were aberrantly expressed in Ankrd11^{nscKO} snL-SVZ microglia including *Apoe, Igf1, Mrc1,* and *Plxnc1* (92, 100).

In summary, snRNAseq and immunohistochemistry concordantly demonstrate that both lateral and dorsal ventricular walls showed increased microglia density and activation in the Ankrd11^{nscKO} mice that correlated with the hydrocephalus severity, with the dorsal regions exhibiting the more severe microgliosis and activation. We thus hypothesized that microgliosis and/or increased microglia activation in the Ankrd11^{nscKO} mice was at least partially responsible for driving the hydrocephalus progression.

Bindarit administration reduces microglia activation and hydrocephalus severity in Ankrd11^{nscKO} mice

To test the role of microgliosis in hydrocephalus severity in Ankrd11^{nscKO} mice, we first treated Ankrd11^{nscKO} and Ankrd11^{Ctrl} mice with BLZ945, a potent Csf1r (Colony Stimulating Factor 1 Receptor) inhibitor, which was previously used in the Aicardi-Goutieres syndrome model of hydrocephalus to eliminate microglia (101). BLZ945 [200mg/kg, dose used by others (102, 103)] or DMSO (vehicle control [VC]) was injected subcutaneously every two days from P2 to P8 (Fig. S6A), and brains were analyzed at P10, a timepoint with highly penetrant but variable hydrocephalus in the Ankrd11^{nscKO} mice (Fig. 1P). Treatment of Ankrd11^{nscKO} mice with BLZ945 successfully eliminated the majority of Iba1+ microglia (237-fold decrease, p=0.0159) in the P10 rostral corpus callosum of the BLZ945-treated Ankrd11^{nscKO} mice relative to VC (Fig. S6B-C). Importantly, Ankrd11^{nscKO} mice treated with BLZ945 exhibited significantly higher hydrocephalus severity compared to Ankrd11^{nscKO} mice treated with VC (Fig. S6D-F). When the ventriculomegaly data were expressed through severity score (no hydrocephalus = score 0, mild hydrocephalus = score 1, moderate hydrocephalus = score 2 and severe hydrocephalus = score 3), Ankrd11^{nscKO} mice treated with BLZ945 had an average score ~2.8, whereas Ankrd11^{nscKO}

mice treated with VC had an average score of ~1.75 (Fig. S6E-F). Since hydrocephalus severity strongly negatively correlated with caudal cortical thickness (Fig. S2F), we assessed the correlation between cortical thickness and hydrocephalus severity score in P10 Ankrd11^{Ctrl} and Ankrd11^{nscKO} mice treated with BLZ945 and VC (Fig. S6G-H). Cortical column size was significantly (R^2=0.58, p=0.001) negatively correlated with hydrocephalus severity score, with only Ankrd11^{nscKO} mice treated with BLZ945 reaching the most severe hydrocephalus score and displaying the thinnest caudal cortex (Fig. S6H). Thus, microglia ablation worsens hydrocephalus severity in the Ankrd11^{nscKO} mice.

Next, we tested the role of microglia activation, since dampening of inflammation has been shown to improve hydrocephalus (104-106). Specifically, Bindarit, a small molecule inhibitor of myeloid cell activation through inhibition of chemoattractant proteins (*CCL2, CCL7, CCL8*) production (107), reduced ventricle volume in various rodent models of hydrocephalus (105, 106). Thus, we asked whether Bindarit can attenuate microglia activation and hydrocephalus severity in Ankrd11^{nscKO} mice. Bindarit, or DMSO (VC), was subcutaneously injected daily from P2-P9 at 100 mg/kg (dose used by others (106, 107)), to attenuate microglia activation (Fig. 6A). Mice were assessed at P10, similar to BLZ945 treatment. Treatment of Ankrd11^{nscKO} mice with Bindarit reduced the density of Dectin1+ cells (~1.2-fold change, p=0.018) without affecting the density of total Iba1+ cells in Ankrd11^{nscKO} mice compared to VC-treated and naive Ankrd11^{nscKO} mice (Fig. 6B-D). Importantly, the proportion of P10 Ankrd11^{nscKO} animals with severe hydrocephalus was reduced with the administration of Bindarit when compared to VC (Fig. 6E-F). Moreover, hydrocephalus score was slightly but significantly reduced in Ankrd11^{nscKO} mice treated with Bindarit compared to Ankrd11^{nscKO} mice treated with VC (~1.7-fold change, p=0.0128). Furthermore, Ankrd11^{nscKO} mice treated with Bindarit had mildly but significantly increased (~1.1-fold change, p=0.0441) caudal cortical column size, when compared to Ankrd11^{nscKO} treated with VC and similar to Ankrd11^{Ctrl} treated with VC (Fig. 6H-I). Finally, the caudal cortex size correlated negatively with hydrocephalus severity score (R^2=0.519, p<0.001), with only Ankrd11^{nscKO} mice treated with VC reaching the highest hydrocephalus score and displaying the thinnest cortex (Fig. 6J). Thus, consistent with a previous report (106), the administration of Bindarit mildly attenuated the proportion of Dectin1+ microglia and partially rescued hydrocephalus severity in Ankrd11^{nscKO} mice, indicating that microglia activation contributes to hydrocephalus severity. Having confirmed that microgliosis in

the Ankrd11^{nscKO} model modulates hydrocephalus severity, we set out to determine whether Ankrd11-deficient SVZ NPCs, which exhibit aberrant immune gene expression (Fig. 4), could contribute to non-cell autonomous microglial activation in this mouse model.

Ankrd11-deficient SVZ NPCs participate in aberrant cell-cell communication with microglia

Microglia arise from the E9 embryonic yolk sac (53, 87) and thus are not directly affected by the loss of Ankrd11 at E14.5 NPCs and their progeny. In support of this, our data demonstrate that none of the recombined YFP+ cells in Ankrd11^{WT} or Ankrd11^{nscKO} mice are Iba1+ (Fig. S1C). Therefore, the increased microgliosis in Ankrd11^{nscKO} brain arises due to a non-cell autonomous effect. We thus questioned if the microgliosis and neuroinflammation in Ankrd11^{nscKO} mice was solely due to the onset of hydrocephalus, which was previously postulated to drive microglia changes (84, 85, 108), or if aberrant communication between Ankrd11-deficient NPCs and/or their progeny with Ankrd11-expressing microglia contributed to the neuroinflammation. Extensive previous work has shown that NPC-derived ligands can regulate microglia function and activation during development and disease (reviewed in (109, 110)). In Ankrd11^{nscKO} mice, Iba1+ and Dectin1+Iba1+ cells were abnormally abundant in the periventricular regions directly adjacent to the SVZ NPCs that displayed aberrant immune gene expression (Figs. 4-5). While endogenous SVZ NPCs are known to regulate microglia function in a demyelinated corpus callosum of wild-type mice (111), the ability of SVZ NPCs to modulate microglia biology in the context of a hydrocephalus mouse model is unknown. We hypothesized that Ankrd11-deficient NPCs may contribute to neuroinflammation by communicating aberrantly with microglia at least in part due to abnormal expression of immune genes.

Since Ankrd11^{nscKO} dorsal periventricular regions showed the highest increase in total microglia and DAMs, which correlated with most pronounced changes in the NPC transcriptome, we subjected microglia and NPCs from the snCC dataset to LIANA (LIgand-receptor ANAlysis tool (112)), a consensus-based algorithm for detecting cell-cell communication networks. We first randomly down sampled snCC NPC nuclei in Ankrd11^{Ctrl} and snCC microglia nuclei in Ankrd11^{nscKO} to equal numbers between all samples. As we are interested in the unidirectional communication from NPCs to microglia, we set NPCs from each genotype as two separate source populations (ligand expressing) and the combined population of

microglia from both genotypes into a single target population (receptor expressing), identifying over 100 predicted interactions in both the Ankrd11^{Ctrl} and Ankrd11^{nscKO} conditions (Table S7). Using LIANA based aggregate rank as a measure of interaction strength, we then identified ligand-receptor (L-R) pairs that highly differed (aggregate rank shift ≥ 0.01) between Ankrd11^{Ctrl} NPCs and Ankrd11^{nscKO} NPCs communication with microglia (Fig. 7A, Table S7). This analysis predicted NPC ligands, such as *Ptn* and *Vegfa*, which drive microglia migration and activation towards an inflammatory state (113, 114), had higher predicted interaction strength in Ankrd11-deficient NPCs compared to Ankrd11^{Ctrl} NPCs (Fig. 7A). In contrast, NPC ligands, such as *Mfge8,* and *Cd47,* which typically promote inflammation resolution, or enable microglia-mediated phagocytosis of damaged cells (115, 116), had lower predicted interaction strength in Ankrd11-deficient NPCs compared to Ankrd11^{Ctrl} NPCs (Fig. 7A).

Next, we asked whether expression of these ligands in Ankrd11^{nscKO} NPCs in the snCC dataset correlates with hydrocephalus severity and DAM activation. Notably, the role of several predicted ligands in regulating microglia biology is not yet well known or depends on the CNS environment. Nevertheless, Fig. 7B demonstrates the highest expression of ligands that are known to promote microglia activation (e.g. *Vegfa, Ptn* and *Gnai2* (113, 114, 117, 118)) and lowest expression of ligand *Cd47*, which alleviates microglia activation (119), in the Ankrd11^{nscKO} NPCs with moderate hydrocephalus and high proportion of DAMs compared to Ankrd11^{nscKO} sample with mild hydrocephalus and low proportion of DAMs. Collectively, these results demonstrate that loss of Ankrd11 in E14.5 NPCs alters expression of immune ligands in postnatal SVZ NPCs, which are predicted to communicate aberrantly with microglia.

To test the functional significance of the predicted aberrant NPC-microglia communication in Ankrd11^{nscKO} samples, we co-cultured SVZ NPCs from Ankrd11^{Ctrl} and Ankrd11^{nscKO} brains with microglia isolated from the cortex of wild type (WT) pups (Fig. 7C). Briefly, P7 SVZ NPCs were expanded as primary neurospheres from Ankrd11^{Ctrl} and Ankrd11^{nscKO} brains and plated as monolayers for 24h according to our previously published protocol, which yields >90% NPCs (47). At this timepoint, WT microglia, which were cultured and isolated from P0 cortex according to our previous report, yielding >95% microglia (120), were added to Ankrd11^{Ctrl} or Ankrd11^{nscKO} NPCs for 1DIV and assessed for density, proliferation, activation, and cell death (Fig. 7E, G, I). In the presence of Ankrd11^{nscKO} NPCs,

there was a significant increase in the number of total Iba1+ microglia (~1.4-fold change, $p<0.001$), proportion of Ki67+Iba1+ microglia (% Ki67+Iba1+/Iba1+ cells, ~1.9-fold change, $p=0.0098$) and proportion of Dectin1+Iba1+ microglia (% Dectin1+Iba1+/Iba1+ cells, ~1.4-fold change, $p=0.0086$) when compared to microglia cultured with Ankrd11^{Ctrl} NPCs or without NPCs (Fig. 7D-H). Notably, we found no change in the proportion of microglia undergoing cell death in any of the conditions (Fig. 7I-J). Taken together, these data demonstrate that Ankrd11^{nscKO} NPCs induce microglia proliferation and activation, which likely contribute to increased microglial density and/or activation in the hydrocephalic Ankrd11^{nscKO} mice.

Discussion

In this study we show that loss of Ankrd11 in late embryonic NPCs results in altered ependymal cell function with unique transcriptomic profile contributing to postnatal hydrocephalus formation. We further show that severity of hydrocephalus is mediated, at least in part, by the activation of microglia, and that Ankrd11-deficient SVZ NPCs express immune ligands and contribute to anomalous activation of microglia, primarily within the dorsal region of the lateral ventricles. Therefore, Ankrd11 is a critical regulator of the postnatal brain lateral ventricle size by controlling ependymal cell function and microgliosis.

Overall, this study has identified five key findings. First, our report demonstrates a defined mechanistic contribution to the induction of hydrocephalus in Ankrd11^{nscKO} mice, attributable to altered ependymal cell polarity and cilia function, both of which are definitive causes of hydrocephalus onset (21-23). Importantly, while disruptions in several chromatin remodellers cause ventriculomegaly (29, 31, 121), little is known about their role and mechanism in ependymal cell formation and/or maturation. The best studied chromatin regulator in ependymal cell differentiation is BRG1, the deletion of which in NPCs causes an increase in ependymal cell formation (122). While the role of chromatin regulators in ependymal cell maturation remains unclear, it is known that transcription factors, like NFIX, regulate this process (123, 124). Our results show that ablation of Ankrd11, a chromatin regulator that controls global gene expression via histone acetylation (32-34), in late embryonic NPCs leads to increased ependymal cell apical size and basal body area at P7. While it is difficult to separate the effects on differentiation versus maturation, together with additional results showing normal

ependymal cell density and area at P5 as well as altered planar cell polarity and decreased motile cilia function at P6-7, our data argue that Ankrd11 regulates the maturation of ependymal cell function. This is supported by Ankrd11-dependent changes in the ependymal cell gene expression linked to ependymal dysfunction and/or ciliary/CSF homeostasis (*Ptprq* and *Ecm1*), ependymal cell activation and polarity (*Gfap*), and intracellular Ca^{2+} signalling required for appropriate cilia beating and frequency (*Calb1*) (125-130). This adds to the growing body of evidence that chromatin regulators, like Ankrd11, are crucial for regulating ependymal cell biology.

Second, our findings suggest a novel role for SVZ NPC dysfunction in the hydrocephalus phenotype. Consistent with our observation of a decreased SVZ NPCs pool *in vivo*, hydrocephalic *hyh* mice also exhibit fewer SVZ NPCs (131). However, SVZ NPCs isolated from *hyh* mice form neurospheres and differentiate comparably to control mice, suggesting that their *in vivo* deficits arise primarily from disruption of the SVZ neurogenic niche rather than an intrinsic SVZ NPC defect (131). In contrast, our current and previous findings (42) show that Ankrd11 ablation in late embryonic NPCs reduces postnatal SVZ NPC neurosphere size, proliferation and neurogenesis *in vitro*, supporting a cell-autonomous requirement for Ankrd11 in SVZ NPC biology. Although our *in vivo* experiments cannot fully distinguish intrinsic effects from secondary consequences of the perturbed ventricular environment, the *in vitro* phenotype demonstrates that Ankrd11 loss directly compromises SVZ NPC function.

Third, our report shows that Ankrd11-deficient NPCs have perturbed expression of genes that regulate cilium movement with concomitant increase in primary cilium length. While short primary cilium is linked to enhanced proliferation, long primary cilium is associated with decreased proliferation (132, 133). In this light, we have previously shown that loss of Ankrd11 in embryonic NPCs decreases postnatal SVZ NPC and neuroblast proliferation (42). The best studied extracellular signalling molecule that controls cell proliferation via primary cilium is Sonic Hedgehog (Shh) (25, 133). Interestingly, Shh-pathway related genes, like *Gli1-3, Ptch1/2* or *Smo*, were not deregulated in Ankrd1^{nscKO} P15 SVZ NPC bulk or snRNA-seq datasets. Since Ankrd11 controls histone acetylation levels (32, 34), which are important for NPC proliferation (134), it is likely that Ankrd11 knockout deregulates many genes implicated in NPC biology. For example, knockdown of Ankrd11 in early embryonic cortical NPCs reduces their proliferation,

which can be rescued by increasing histone deacetylation through expression of HDAC3 or inhibition of HAT activity (34). Moreover, mice that express mutated Ankrd11 have increased histone acetylation and deregulated global gene expression in embryonic cortical progenitor cells (34). Our results implicating primary cilium length and gene expression in Ankrd11-deficient NPCs extend and support these reports.

Fourth, our report demonstrates aberrant immune gene expression program in Ankrd11-deficient NPCs *in vivo* and *in vitro*. These immune related genes include the complement cascade, a classical immune activation pathway, as well as PTN and APP, which contribute to a chronic activation and neuroinflammatory response in resident immune cells (77, 114, 135, 136). Furthermore, our data predicts perturbed communication between Ankrd11-deficient SVZ NPCs and microglia, which we validated in co-cultures demonstrating that Ankrd11-deficient SVZ NPCs induce microglia activation. A previous report has shown that knockout of PTEN in embryonic ventral forebrain NPCs leads to ventriculomegaly associated with non-cell autonomous effect on choroid plexus macrophages, which exhibit elevated levels of gene expression related to innate immune cell activation and Toll-like receptor (TLR) signaling (137). While the mechanism of non-cell autonomous immune cell activation in NPC-specific PTEN knockout mice was not determined, it is tempting to speculate that PTEN-deficient NPCs could participate in immune cell activation similarly to Ankrd11-deficient NPCs. It is well established that the main role of NPCs is to ensure proper brain development and regeneration, however, they can also have immunomodulatory properties (reviewed in (109, 138)). For example, endogenous SVZ NPCs or NPCs derived from human induced pluripotent stem cells (iPSCs) modulate microglial phagocytosis and homeostasis via Mfge8 and Cd47, respectively (111, 116). Furthermore, transplantation of human NPCs overexpressing Sox2 into the brain of posthemorrhagic hydrocephalus restores ventricular volume and promotes alternate state of microglia associated with expression of anti-inflammatory cytokines (formerly known as M2) by attenuating the TLR4 pathway activation and reducing TNFα and IL1β expression (139). In the Ankrd11^{nscKO} mouse model, it is possible that the hydrocephalus itself may contribute to immune gene expression in NPCs and/or microglia activation *in vivo*. However, as hydrocephalus, a macrostructural brain condition, is absent in isolated cell cultures, the observed immune gene signature in Ankrd11-deficient NPCs *in vitro* and their ability to activate microglia in co-cultures represent intrinsic, cell-autonomous mechanisms rather than a response to altered intraventricular

pressure. These findings may suggest a potential new mechanism for neuroinflammation mediated by SVZ NPCs in other genetic models of hydrocephalus and/or neurodevelopmental disorders.

Finally, our report identifies microglia as an aggravating factor of hydrocephalus severity in the Ankrd11^{nscKO} mice. The precise role of microglia in hydrocephalus biology is debated. Constitutive absence of microglia via deletion of mouse *Csf1r* gene or a conserved enhancer FIRE in its locus causes perinatal hydrocephalus on C57BL/6N, but not on mixed CBA/J or BALBc/J genetic backgrounds (9, 140-142), suggesting that microglia contribution to hydrocephalus formation may be strain dependent. Pharmacological ablation of microglia using Csf1r inhibitors in genetic models of hydrocephalus has produced mixed results. Administration of PLX5622 in mice that carry a point mutation in the *Ccdc39* (Coiled-coil domain containing 39) gene, which causes loss of motile cilia mediated CSF flow and neonatal hydrocephalus formation, results in an increased ventriculomegaly (86). In contrast, administration of BLZ945 in a murine model of Aicardi-Goutières syndrome or PLX3397 in an ependymal cell specific knockout of Vps35 (Vacuolar protein sorting-35) alleviates hydrocephalus pathology (101, 143). In contrast, several anti-inflammatory drugs consistently show beneficial effects in various rodent models of hydrocephalus. Administration of Bindarit in the *Ccdc39* mutant mice reduces activation of microglia, overall ventricular volume and cortical thinning (105, 106). Administration of celecoxib (nonsteroidal anti-inflammatory drug and COX-2 inhibitor) into the CSF of kaolin induced rat model of hydrocephalus reduces neuroinflammation and improves corpus callosum thinning (144). Finally, administration of metformin in a posthemorrhagic hydrocephalus murine model reduces microglia and astrocyte activation and rescues lateral ventricle volume (145). Therefore, while dampening of microglia activation has a documented beneficial effect on hydrocephalus severity in various disease models, pharmacological ablation of microglia can be either beneficial or detrimental in different genetic models and/or due to specific Csf1r inhibitors. Our results, which show that ablation of microglia in postnatal Ankrd11^{nscKO} mice exacerbates hydrocephalus severity while attenuation of microglia activity reduces hydrocephalus severity, mirror the effects of microglia ablation and activity reduction in the Ccdc39 mutant mice (86, 105, 106).

In addition to scientific novelty and relevance, our results provide an explanation for the development of enlarged ventricles in at least some patients with *ANKRD11* mutations. While the prevalence of this brain phenotype is not fully known since MRI imaging is not offered to all affected patients, recent reports demonstrate that ventricle abnormalities are present in up to ~37% of cases (38-41). Together with these clinical data, our results strongly argue for the role of ANKRD11 in brain ventricle size regulation and may justify a periodic cerebral MRI monitoring in the patient population with *ANKRD11* mutations to fully understand the prevalence, progression and clinical significance of this neurological finding.

Materials and Methods

Animals

All animal use was approved by the Animal Care Committee of the University of Alberta in accordance with the Canadian Council of Animal Care policies. All mice were housed in the University of Alberta Animal Facility and served by North Campus Animal Services (NCAS). Mice were maintained on a 12h light or dark cycle, and food and water were provided ad libitum. Embryos at developmental ages embryonic day (E) 14.5, 14.75, 15.5, 18.5 and postnatal mice at ages postnatal day (P) 3, 5, 6, 7, 10, 15, and 30 of both sexes were used for all experiments. For animals used at postnatal ages, E19.5 embryos from tamoxifen-induced dams were delivered via caesarean-section and cross fostered with CD1 time pregnant females purchased from Charles River as per previously published protocols (42, 146, 147). Pregnant dams and early postnatal pups (under P10) were euthanized with CO2, and brains were dissected from E14.5-18.5 embryos and early postnatal pups. Pups older than P10 (up to P30) were euthanized via intraperitoneal injection of euthanyl (Bimeda-MTC) at 192 mg/kg body weight. Pups over P10 then underwent a transcardiac perfusion with HBSS and 4% PFA (when required).

Ankrd11$^{fl/fl}$;RosaYFP$^{STOP/STOP}$;NestinCre^{ERT2} mice are described in (42-44). Briefly, Ankrd11$^{fl/fl}$ females containing LoxP sites flanking exon 7 of the Ankrd11 gene were crossed with RosaYFP$^{stop/stop}$ (B6.129X1-Gt(ROSA)26Sortm1(EYFP) Cos/J, stock # 006148) mice from Jackson Laboratories (148) and NestinCre^{ERT2} mice from (45, 149). To generate experimental progeny, Ankrd11$^{fl/fl}$;RosaYFP$^{stop/stop}$ females were mated with

Ankrd11$^{fl/fl}$;RosaYFP$^{stop/stop}$;NestinCre^{ERT2} males, and Ankrd11$^{wt/wt}$;RosaYFP$^{stop/stop}$ females were mated with Ankrd11$^{wt/wt}$;RosaYFP$^{stop/stop}$;NestinCre^{ERT2} males. Pregnant dams were injected with tamoxifen at E14.5 (please see below). All pairings were timed mated and considered E0.5 upon positive plugs testing each morning.

All mice were bred and genotyped in accordance with protocols provided by Jackson Laboratories and the European Mouse Mutant Archive (EMMA), using the following primers: Ankrd11: forward, 5'-CTG TCT CAG AGA GGA GAG TGA GGA GGAC-3'; reverse, 3'-TAC CTT ACA CCC TGA GAC GGC GTC -5', 34 cycles of: 94 °C-30 s, 62 °C-45 s, 72 °C-60 s. YFPSTOP: wild-type, 5'-GGA GCG GGA GAA ATG GAT ATG-3'; common, 5'-AAA GTC GCT CTG AGT TGT TAT-3'; mutant, 5'-AAG ACC GCG AAG AGT TTG TC-3', 35 cycles of 94 °C-15 s, 65 °C-15 s, 72 °C-60 s. Pan-Cre: forward, 5'-TTC CCG CAG AAC CTG AAG ATG-3'; reverse, 3'-11 CCC CAG AAA TGC CAG ATT ACG-5'; control forward primer 5'-AAC AAC AAT GGC ACA ACC TAAT-3'; control reverse 3'-ACT TTC TCC CCA CCC GTC TA-5'; 35 cycles of: 94 °C-15 s, 60 °C-30 s, 72 °C-90 s.

Tamoxifen, Bindarit, and BLZ945 injections

Pregnant murine dams were injected intraperitoneally (IP) at E14.5 with a single dose (90 mg/kg) of tamoxifen (TMX, Sigma), which was dissolved in 9.5% ethanol and sunflower seed oil (Sigma) as previously described in (42, 149, 150). Bindarit (AF2838, MedChemExpress HY-B0498), which was initially dissolved in DMSO at a stock concentration of 100 mg/ml, was first diluted 2x in sunflower seed oil and then administered via subcutaneous injection (SQ) once per day from P2-P9 at 100 mg/kg (2 µl/g of 50 mg/ml) body weight through a 25 µl Hamilton syringe in accordance with previous reports (105, 106). BLZ945 (Sotuletinib, MedChemExpress HY-12768), which was dissolved in DMSO at 100 mg/ml, was administered via subcutaneous injection (SQ) once every two days from P2-P8 pups at 200 mg/kg body (2 µl/g of 100 mg/ml) weight through a 25 µl Hamilton syringe in accordance with previous reports (95, 103).

Evans blue dye injections

P10 postnatal pups were euthanized via IP injection of euthanyl. 10 ml of 0.5% Evans blue dye (Sigma, E2129) diluted in HBSS was transcardially injected followed by 10 ml of 4% PFA. Brains were dissected and further submerged and fixed in 4% PFA overnight. Coronal and

784 sagittal sections of 1 mm thickness were generated the following day using a mouse brain mold
785 (RWD). Tissue sections were imaged under a dissecting microscope with an iPhone 15 pro max
786 (Apple).

787 **Magnetic Resonance Imaging (MRI)**

788 P15 mice were euthanized via IP injection of euthanyl, followed by transcardiac
789 perfusion with 30 mL of phosphate-buffered saline (PBS) with 1 µl/mL heparin (1000 USP
790 units/mL) and 2 mM ProHance (Gadoteridol injection, Bracco Imaging) imaging contrast agent.
791 A second perfusion was performed with 30 mL of 4% paraformaldehyde (PFA; prepared using
792 16% aqueous PFA [Electron Microscopy Sciences #15710]) in PBS with 2 mM ProHance
793 (Bracco Imaging). Both solutions were made fresh on the day of perfusion, maintained at room
794 temperature, and perfused with a peristaltic pump (PeriStar Pro, World Precision Instruments) at
795 a rate of 1.0 ml/min (151). A 7-Tesla 306 mm horizontal bore magnet (BioSpec 70/30 USR,
796 Bruker, Ettlingen, Germany) with a ParaVision 6.0.1 console was used to image brains in skulls.
797 Eight samples at a time were imaged in parallel using a custom-built 8-coil solenoid array. To
798 acquire anatomical images, the following scan parameters were used: T2W 3D FSE cylindrical
799 k-space acquisition sequence, TR/TE/ETL = 350 ms/12 ms/6, TEeff = 30ms, four effective
800 averages, FOV/matrix-size = 20.2 × 20.2 × 25.2 mm/504 × 504 × 630, total-imaging-time = 13.2
801 h. The resulting anatomical images had an isotropic resolution of 40 µm voxels. Three-
802 dimensional modeling and volume quantification of structures from MRI scans were performed
803 using sagittal, axial, and coronal MRI images and ITK-SNAP software (152). Three-dimensional
804 volumetric segmentation was traced manually for relevant structures, including the lateral
805 ventricle, 3rd ventricle, hippocampus, and olfactory bulb, and measured using the inbuilt "volume
806 and statistics" function included in ITK-SNAP. Cortical thickness was measured from four
807 coronal slices spanning 0.8 mm (20 slices total) and matched to the Allen Mouse Brain
808 Reference Atlas (P56, Coronal), specifically images 46-54 for rostral cortex and images 70-82
809 for caudal cortex.

810 **Immunohistochemistry**

811 Brains isolated from PFA-perfused animals (over P10) or non-perfused animals (under
812 P10 including embryonic) were incubated in 4% PFA for 24 hours at 4°C, followed by
813 incubation in 30% sucrose for 3-7 days. Postnatal whole brains were then photographed using an

iPhone 15 pro max (Apple) to capture and qualitatively assess hydrocephalus severity (Fig. 1P and S1P). Hydrocephalus severity of postnatal brains was assessed when photographed and categorized based on overall brain size, and caudal cortex thickness and/or collapse. Samples were embedded in optimal cutting temperature compound (OCT, Epredia) and flash frozen, before sectioned coronally at 16 µm thickness on a cryotome (Leica biosystems, Germany). Sections were collected on a glass microscope slide and stored at -80°C. For whole mount tissue preparation, P5-P10 pups were euthanized via cervical dislocation and the lateral ventricle wall was microdissected by removing the dorsal cortex, medial thalamus, and septal structures as detailed in (64). Whole mount tissue was then processed for immunostaining (see below), live imaging (see below – "Live imaging") or SEM (see below - "Scanning electron microscopy").

Immunohistochemistry of cryosections is described in (42). Briefly, slides with sections were blocked for 1h with 5% BSA (bovine serum albumin, Jackson ImmunoResearch) and 0.3% Triton-X100 (Bio Basic, TB0198) in PBS with or without MOM (Mouse on Mouse) blocking reagent (Vector, VECTBMK2202) as required by the primary antibodies. Primary antibodies were diluted in 5% BSA, MOM protein diluent added if required, and incubated overnight at 4°C. Optionally, MOM biotinylated anti-Mouse IgG diluted in PBS with added MOM protein diluent, was incubated for 10 min at room temperature the following day. Sections were then incubated with the appropriate secondary antibodies for 1h at room temperature (listed in "Antibodies" section) diluted in 5% BSA. Sections were counter stained with Hoechst (33217; Riodel-De Haen Ag) for 2 min in PBS, washed thoroughly and mounted with Permafluor (Fisher).

Whole mount tissue was immunostained following the protocol in (64). Briefly, whole mount tissue was incubated, ventricle side up, in 4% PFA with 0.1% Triton-X100 overnight at 4°C in 24 well plates. Tissue was initially blocked with 10% BSA in 0.1M PBS with 0.5% Trixon-X100 (herein referred to as WM Block) with or without MOM blocking reagent as required by the primary antibodies for 24 hours at 4°C. Optionally, MOM biotinylated anti-Mouse IgG in WM block was added for 24 hours after primary antibody incubation. Appropriate secondary antibodies were also diluted in WM block and incubated for 24 hours at 4°C following primary and/or IgG incubation. Whole mount tissue was counter stained with Hoechst for 30 min

in PBS. The whole mount tissue was then further microdissected to isolate the lateral ventricle wall (200-300 μm thickness) and mounted with Permafluor.

Cultures

Primary Neurospheres

Cells from microdissected E15.5 neocortex or P7 or P15 SVZ from Ankrd11^{Ctrl} and Ankrd11^{nscKO} pups were mechanically triturated and cultured at clonal density (10 cells/μl) as described in (42, 47). Briefly, cells were cultured in serum free medium (SFM: equal parts Dulbecco's modified Eagle medium low glucose (DMEM, 10567–014, (Sigma), 5 mM HEPES (Gibco), 0.1125% sodium bicarbonate (NaHCO3, Gibco), 1% penicillin–streptomycin (Gibco), and 100 μg/mL L-glutamine (Gibco), supplemented with 10 ng/mL FGF (fibroblast growth factor; Peprotech), 2% B27 (Gibco), 20 ng/mL EGF (epidermal growth factor; Peprotech), and 2 μg/mL heparin sodium salt (H3149-50KU; Sigma) in 6-well polystyrene microplates for 6 or 7 days in vitro (DIV). E15.5 6DIV and P15 7DIV primary neurospheres were collected and subjected to RNA purification according to manufacturer instructions (Omega Bio-Tek E.Z.N.A Kit or MicroElute RNA kit). P7 6DIV primary neurospheres were pooled and utilized for NPC-microglia co-cultures as described below.

NPC-microglia co-cultures

P7 primary neurospheres from Ankrd11^{Ctrl} and Ankrd11^{nscKO} pups were dissociated as in (47). Resulting single cell suspension of primary neurosphere cells were plated at 40,000 cells/cm^2 density, on 40 μg/mL PDL- and 4 μg/mL laminin-coated glass coverslips. Cells were cultured in NPC media (SFM described above supplemented with FGF, EGF, and B27) for 1DIV before adding microglia. Microglia were cultured from microdissected P0-P2 CD1 cortex in T75 flasks. Resulting cell suspension was cultured as mixed glia cultures in microglia media (DMEM/F12 [Gibco] with 10% FBS [Sigma], 1% Pen/Strep, 1% sodium pyruvate, and 50 μM β-mercaptoethanol) as per (120, 153), with slight modifications. Notably 10 ng/mL GM-CSF was added from 8-11 DIV. Microglia were isolated on day 14 through lidocaine and shaking as described in (120, 153). Microglia were briefly washed with NPC media then added to 1DIV NPC monolayer cultures at 10,700 cells/cm^2. NPCs and microglia were co-cultured together for 24 hours. When required, propidium iodide (PI; Invitrogen, 25535-16-4) was added to the culture

at 5 μg/ml, for 15 min at 37°C and washed twice with PBS prior to immunocytochemistry (see below).

Immunocytochemistry

NPC-microglia co-cultures were immunostained as previously described in (42, 149). Briefly, cells were fixed with 4% PFA for 10 min, permeabilized in 0.2% IGEPAL CA-630 (Sigma) in PBS, and blocked with 6% donkey serum and 0.5% BSA in PBS for 1hr. Coverslips were then incubated in primary antibodies overnight at 4°C and secondary antibodies for 1hr (see "Antibodies" section). Coverslips were counter stained with Hoechst and mounted with Permafluor.

RT-qPCR

20 to 70 ng of total RNA isolated from E15.5 primary neurospheres was processed with QuantiTect Reverse Transcription Kit (Qiagen) to generate cDNA as per manufacturer's instructions. $1/100^{th}$ of the RT reaction was used for qPCR amplification, which was performed according to MIQE guidelines (154) using the Ssoadvanced SYBR Green kit (BioRad) on the Roche LightCycler 96 machine with the following primers: *Ankrd11* exon 6-7 junction: Forward 5'-CAC CGA GCA GCT ATC CGA G-3'; Reverse 5'-GCT AAC AGT TGC TTG GCG ATG-3', 40 cycles of; 95 °C 15 s, 60 °C 15 s, 72 °C 20 s. *Gapdh*; Forward 5'-AAA TAC GGA CTG CAG CCC TC-3'; Reverse 5'-AAA TCC GTT CAC ACC GAC CTT-3', 40 cycles of; 95 °C 15 s, 60 °C 15 s, 72 °C 20 s. Ankrd11 Ct values were measured in duplicate and averaged, then normalized to the housekeeping gene *Gapdh* Ct values and a relative control within each experiment. Data are presented as $2^{-(\Delta\Delta Ct)}$ (RQ [relative quantity] value) (155).

Antibodies

Primary antibodies: anti-Arl13b (ProteinTech, 17711-1-AP, RRID:AB_2060867, 1:500), anti-βcatenin (Sigma, C2206, RRID: 476831, 1:1000), anti-βcatenin (R&D systems, AF1329, RRID:AB_354736, 1:1000), anti-Ctip2 (Abcam, 18465, RRID:AB_2064130, 1:500), anti-Dectin1 (Invivogen, mabg-mdect, RRID:AB_2753143, 1:50), anti-GFP (Abcam, ab13970, RRID: AB_300798, 1:1000), anti-GFP (Abcam, ab290, RRID: AB_303395, 1:2000), anti-IB4-Biotin (Vector Laboratories, B-1205, RRID:AB_2314661, 1:500), anti-Iba1 (Sigma, SAB2500041, RRID:AB_10600296, 1:500), anti-Ki67 (BD Pharmingen, 556003,

RRID:AB_396287, 1:500), anti-NeuN-Alexa555 (Millipore, MAB377A5, RRID: AB_2814948, 1:250), anti-Olig2 (Thermofisher, MA5-32039, RRID:AB_2809333, 1:500), anti-Pax6 (Convance, PRB-278P, RRID:AB_291612, 1:1000), anti-Satb2 (Abcam, ab51502, RRID:AB_882455, 1:500), anti-Sox2 (Novus Bio, AF2018, RRID:AB_355110, 1:1000), anti-Tbr1 (Abcam, ab31940, RRID:AB_2200219, 1:1000), anti-Tbr2 (Millipore, ab15894, RRID:AB_10615604, 1:500), anti-γTubulin (Abcam, ab11316, RRID:AB_297920, 1:500).

Secondary antibodies: anti-chicken-488 (Jackson, 703-545-155, RRID:AB_2340375, 1:1000), anti-chicken-647 (Jackson, 703-605-155, RRID:AB_2340379, 1:1000), anti-goat-488 (Jackson, 705-545-147, RRID:AB_2336933, 1:1000), anti-goat-555 (Jackson, 705–165-147, RRID:AB_2307351, 1:1000), anti-goat-647 (Jackson, 705-605-147, RRID:AB_2340437, 1:1000), anti-mouse-555 (Jackson, 715-165-151, RRID:AB_2315777, 1:1000), anti-rabbit-488 (Jackson, 711-545-152, RRID:AB_2313584, 1:1000), anti-rabbit-555 (Jackson, 711-165-152, RRID:AB_2307443, 1:1000), anti-rabbit-647 (Jackson, 711-605-152, RRID:AB_2492288, 1:1000), anti-rat-488 (Jackson, 712-545-150, RRID:AB_2340683, 1:1000), anti-rat-555 (Jackson, 712-165-153, RRID:AB_2340667, 1:1000), anti-rat-647 (Jackson, 712-175-150, RRID:AB_2340671, 1:1000), streptavidin-555 (Jackson, 016-160-084, RRID:AB_2337244, 1:1000), streptavidin-647 (Jackson, 016-170-084, RRID:AB_ 2337245, 1:1000).

Microscopy

Fluorescent and confocal microscopy

Immunostained brain sections and cultures were imaged using a Zeiss Axio Imager M2 fluorescence microscope, ORCA-Flash LT sCMOS Camera, and Zen software (Zeiss). *In vitro* cultures were imaged in a single plane at 200x magnification with a minimum of five random fields of view (FOV) per cover slip. Four to six brain sections per brain were also imaged at 200x magnification and tiled to encompass the region of interest. Immunostained whole mount tissue samples were imaged with a Zeiss LSM700 confocal microscope with a photomultiplier tube (PMT) using the 40x NA 1.3 oil immersion objective (EC Plan-Neofluar). Eight to ten images encompassing the entire lateral ventricle tissue were captured at 400x magnification with oil immersion in a single plane. Three wells of primary neurospheres from each animal were swirled to the center of well and imaged using Zeiss Primovert inverted cell culture microscope, Zeiss Axiocam ERc5s camera, and Zen software (Zeiss) prior to collection and dissociation.

931 ***Live imaging microscopy (whole mount)***

932 Cilia bead movement *ex vivo* recordings were performed on P6 whole mount lateral
933 ventricle tissue was dissected as described above. The lateral ventricles were immediately
934 submerged in cold HBSS and immobilized with 23G needles onto the petri dish. FluoSpheres™
935 Polystyrene Microspheres (1.0 μm, red fluorescent; F13083, ThermoFisher, Waltham, MA) were
936 used to track cilia generated flow across the lateral ventricle tissue. FluoSpheres were diluted to
937 25% in 5% glycerol in MilliQ and manually deposited (0.2 μL) onto the tissue. Live video was
938 recorded at 4.40 frames per second for 10-30 seconds using an Olympus SZX12 Fluorescence
939 Stereoscope equipped with a Zeiss Axiocam 105 camera under a 38.4x zoom. Video acquisition
940 was achieved by using the Labscope Software v6. ImageJ software was used to manually track
941 flourescent particles and calculate the average speed of bead velocity.

942 **Scanning electron microscopy (SEM)**

943 P10 mice were euthanized via cervical dislocation, and the brain was quickly dissected.
944 Lateral ventricles were excised following the protocol in (64) and mounted on Whatman 1 filter
945 paper to preserve wall facing orientation. Mounted samples were immediately fixed in 2.5%
946 glutaraldehyde and 1.6% PFA in 0.1M sodium cacodylate (pH 7.2) overnight at 4°C (156). Fixed
947 samples were washed twice with the same fixation buffer and three times with a 0.1M sodium
948 cacodylate buffer. After the washes, samples were dehydrated through a graded series of ethanol
949 washes 30% to 100%. Samples were kept in 100% ethanol until they were loaded into the critical
950 point dryer and further dehydrated with liquid CO2 (Bal-tec CPD 030). Once completed,
951 samples were mounted onto a carbon sticker on top of an aluminum SEM stub and sputter coated
952 with Au/Pd (Hummer 6.2 Sputtering system). Samples were then visualized and imaged on
953 a scanning electron microscope (Evo 10, Zeiss) with Smart SEM software version 6.06 at 10.0
954 kV accelerating voltage.

955 **Data analysis**

956 Sample numbers are indicated in figure legends (*n*). All data were graphed using
957 GraphPad Prism (version 8.0.2) and depicted as mean ± sem. Representative images were
958 acquired with Zen software and analyzed in Fiji ImageJ v1.54p software (157). Figures were

generated in Adobe Illustrator CC 2015. Schematics were generated using Biorender and Adobe Illustrator.

Image analysis

Whenever possible, image analysis was blinded to genotype. However, due to structural differences in postnatal Ankrd11^{nscKO} animals, blinding was not possible for tissues collected from >P3 animals. Data from at least three animals from two independent litters was analyzed for all ages.

For whole mount analysis, a minimum of five images per animal were analyzed, with apical cell number and area traced and measured in ImageJ. Ependymal cells were identified by a larger βcatenin border with multiple γTubulin puncta within the cell boundary. NPCs were identified with a smaller βcatenin border with a single bright γTubulin punctum within the apical cell (20). For planar cell polarity analysis, the apical cell border marked with βcatenin and the basal body (grouped γTubulin puncta) of 15 ependymal cell per image were manually traced and converted to binary images. PCP autocount (158) was then applied to all binary images with the same settings and vector length and angle were recorded. Average angle of each photo was calculated and relative angle of each basal body vector to the average angle of the photo was determined and graphed. Proportion basal body patch area was calculated from 20 ependymal cells per image per animal using the same manual tracing and binary conversion as above.

Marker+ cells were quantified from immunohistochemistry images as described in (34, 42, 159). Briefly, anatomically matched coronal sections over the dorsal and ventral lateral walls (encompassing rostral cortex) were imaged. A defined size column was overlayed on the images directly over the lateral ventricle to create corpus callosum and cortical grey matter regions of interest. A separate defined region of interest was overlayed for the D-LSVZ and L-SVZ regions, and the relevant tissue region was manually outlined and area recorded. Marker+ cells within each region of interest were quantified. Results are presented as marker+ cells over area (density), average marker+ cells per region or double marker+ cells per region or over area. A minimum of 4 images per animal were analyzed.

For all immunostained culture experiments, five to seven random fields of view (FOV) were captured at 200x magnification for each biological replicate. For each co-culture condition

approximately 100 Iba1+ microglia were analysed from a minimum of four images per animal. Data are presented from at least eleven pups from two independent litters.

For primary neurosphere analysis, spheres containing over 50 cells were counted (150, 160). Each data point is the average amount of spheres from two technical replicates per each biological replicate. Sphere diameter analysis was performed using ImageJ, where the longest diameter of each sphere was recorded. A minimum of 75 spheres per biological replicate were analyzed.

SEM images at 1,000x magnification were utilized to determine cilia bundle density. A minimum of five images per animal from two independent biological litters were quantified. The region containing cilia bundles was identified and outlined in ImageJ, each cilia bundle was manually counted, and cilia bundle density was calculated. Each dot represents the average cilia bundle density for each individual animal.

Statistical analysis

Majority of data passed normality tests including the D'Agostino & Pearson test, Kolmogorov-Smirnov, or Shapiro-Wilk tests, except for Figs. S6F, 6G, and 7J. For normal data, parametric tests were performed as described below. For comparison between two groups unpaired students t-test or multiple t-tests were used to assess statistical significance between groups. For comparison between three-groups one- or two-way ANOVA performed followed by Tukey's multiple comparisons. For non-normal data comparison between two groups utilized the Mann-Whitney test, for comparison between 3 groups the Kruskal-Wallis test was performed. In all cases GraphPad Prism (version 8.0.2) was used for statistical tests. In figures, significance is indicated by increasing number of asterisks with * $p<0.05$, ** $p<0.01$, *** $p<0.001$.

RNA Data analysis

Bulk RNA sequencing Sample Preparation

Total RNA isolated from P15 Ankrd11^{Ctrl} and Ankrd11^{nscKO} primary neurospheres was generated as described above. Genomic DNA digestion was performed following the manufacturers instruction using DNAse1 (OMEGA Biotek). RNA was stored at -80°C until library generation. RNA quality was assessed by Agilent Fragment Analyzer, and the high-

quality RNA (RIN > 9) samples (n=4 per genotype) were subjected to library preparation using the Illumina Stranded mRNA Library Preparation Kit (Cat#20040532) according to the manufacturer's instructions. Libraries fragment size was checked using an Agilent Fragment Analyzer, then quantified with Qubit and qPCR using Collibri™ Library Quantification Kit (ThermoFisher, Cat#A38524500) on a BioRad CFX96 Touch Real-Time PCR Detection System. Quality checked libraries were loaded onto an Illumina NovaSeqX Plus running PE 150 cycles and sequenced at a depth of 50 million reads. Real-time basecall (.bcl) files were converted to FASTQ files using Illumina bcl2fastq2 v2.20 conversion software.

Bulk RNA sequencing Analysis

Bulk RNA sequencing files were processed and analyzed as per (47). Briefly BAM files were generated from paired end fasta.gz files aligned using STAR with the mouse reference genome M25 release, GRCm38 (161). A counts matrix was generated using *featureCounts* (version 2.16.1) from Rsubread software from all BAM files (162). The counts matrix was run through DESeq2 (version 1.42.0) to normalize and identify differentially expressed genes (163). Normalized counts were used to generate a principal component analysis (PCA) and correlation heatmaps. Differentiation gene analysis between Ankrd11^{Ctrl} and Ankrd11^{nscKO} samples were filtered to only include genes with an adjusted p-value of <0.05 and log fold change (LogFC) of >|1.5|. Up- and down-regulated genes were loaded into Metascape for gene ontology analysis under *Mus musculus* species (66).

Single Nucleus RNA sequencing (snRNA-seq) Sample Preparation

The P15 snL-SVZ dataset was generated from two male P15 Ankrd11^{Ctrl} and two male Ankrd11^{nscKO} pups. The P15 snCC dataset was generated from two P15 Ankrd11^{Ctrl} (one female and one male) and two Ankrd11^{nscKO} (two male) pups. Each dataset was generated from unique pups from at least two independent litters. All P15 pups were euthanized via euthanyl and perfused intracardially with 15 mL HBSS. The brain was quickly dissected and divided into 2 mm sagittal sections. The lateral SVZ wall (snL-SVZ) or the corpus callosum including the dorsal and dorsolateral SVZ (snCC) was microdissected from two medial sagittal sections and added to a cryotube prior to immersion in liquid N2 for snap freezing. Samples were stored in -80°C until nuclei isolation.

Nuclei were isolated using 10x Genomics' Chromium Nuclei Isolation Kits (V1 and V2 for snCC and snL-SVZ datasets, respectively) according to manufacturer's instructions with a few modifications. Namely, the debris removal was substituted by the Miltenyi Anti-nucleus beads according to manufacturer's instructions. Briefly, frozen tissue pieces were weighed on dry ice before transferring into a petri dish. 500 µl of 1x Lysis buffer for snCC samples or 0.5x Lysis buffer for snL-SVZ samples comprised of Lysis Reagent (10x Genomics, cat. no. 2000558), Reducing Agent B (10x Genomics, cat. no. 2000087), Surfactant A (10x Genomics, cat. no. 2000559), and PBS with RNase Inhibitor (10x Genomics, cat no. 2000565/2001488) for snL-SVZ samples, was added to the frozen tissue on ice. The tissue was chopped into smaller pieces with tissue scissors and then transferred to a 2 mL glass douncer. Three strokes with the loose pestle A and one stroke with tight pestle B were required to fully dissociate the tissue. The total lysis time was 5 minutes. After dissociation, 500 µl of lysate was transferred to the Nuclei Isolation Column (10x Genomics, cat. no. 2000562) and spun at 16,000 rcf for 20 sec at 4°C to remove leftover tissue. Following the centrifugation, the sample was vortexed for 10 sec at 3000 rpm. An aliquot from the lysate was used to calculate the nuclei numbers using a 1:1 dilution with AOPI. This count was used after the spin to calculate the volume of buffer to resuspend the nuclei. The sample was spun at 500 rcf for 3 min at 4°C. The supernatant was removed and the nuclei pellet was resuspended in Nuclei Separation buffer composed of Nuclei Extraction buffer (Miltenyi Biotec, cat. No. 130-128-024), PBS, BSA and RNAse Inhibitor (Millipore Sigma, cat. No. 3335402001 [snCC] or 10x Genomics, cat no. 2000565/2001488 [snL-SVZ]). Miltenyi Anti-nucleus beads (Cat. No.130-132-997) were then added to the sample; 50 µl for each million nuclei. The nuclei were incubated with the beads for 15 min on ice after which an additional 2 mL of the Nuclei Separation buffer was added to the sample. Then the sample was passed through a LS column (Cat. No.130-042-401) attached to the MAC Multistand (Cat. No. 130-042-303) with QuadroMACS separator (Cat. No. 130-042-302) for magnetic separation, prepared by rinsing with 3 mL of Nuclei Separation Buffer. The column was then washed twice with 1 mL of the same buffer. Then the column was placed on a 15 mL collection tube and 1 mL of the Nuclei Separation buffer was added into the column per million nuclei and plunged into the tube. The clean nuclei in the buffer were then spun at 500 rcf for 5 min. The supernatant was removed and the nuclei pellet was washed with Wash Buffer comprised of 1x PBS, 10% BSA and RNase Inhibitor (Millipore Sigma, cat. No. 3335402001 [snCC] or 10x Genomics, cat no.

2000565/2001488 [snL-SVZ]). The purified nuclei suspension was centrifuged at 4°C for 5 min at 500 rcf and the nuclei pellet was resuspended in Resuspension Buffer comprising 20X Nuclei Buffer (10x Genomics, cat. no. 2000207), Reducing Agent B, Nuclease-free water, and RNase Inhibitor. Nuclei counting was done using AOPI on a haemocytometer (Thermo Fisher, cat. no. 22-600-100). Following counting, the appropriate volume for each sample was calculated for a target capture of 20,000 (snL-SVZ dataset) or 10,000 nuclei (snCC dataset).

All samples were loaded into the 10x transposition reaction and incubated for 1hour on a Bio-Rad C1000 Touch™ thermal cycler. Following transposition, snL-SVZ sample nuclei were washed with the Transposition Wash Buffer comprising 20X Nuclei Buffer (10x Genomics, cat. no. 2000207), Reducing Agent B, Nuclease-free water, and RNase Inhibitor. Nuclei count was made using a 1:1 dilution with AOPI to determine the volume of nuclei to be loaded into GEM generation. Then, the nuclei were loaded onto a 10x Multiome GEM-X MO chip for droplet generation. Following transposition, snCC sample nuclei were loaded onto a 10x Multiome J chip for droplet generation. After that, all samples were transferred to pre-chilled PCR strip tubes (MJS BioLynx, cat. no. US14024700) and incubated on a C1000 Touch™ thermal cycler. Quenching Agent was then added to terminate the reaction. Samples were stored at −80°C for <4 weeks prior to library preparation. For library preparation, pre-amplification product was recovered using Recovery Agent (10x Genomics) and purified using a Silane Dynabead mix, following the Multiome ATAC + GEX User Guide (snCC) or GEM-X Epi Multiome ATAC + GEX User Guide (snL-SVZ). Purified product was amplified for 6 (snL-SVZ) or 7 (snCC) cycles, then cleaned using SPRIselect beads (Beckman Coulter, cat. no. B23318). Pre-Amplification product was used for cDNA amplification. cDNA was amplified for 6 cycles, cleaned with SPRIselect beads, and analyzed on a Bioanalyzer (Agilent Technologies) to determine concentration. GEX libraries were prepared per the user guide, with PCR cycle numbers adjusted according to measured cDNA concentration. Library molarity was calculated using Bioanalyzer size output (Agilent Technologies) and qPCR quantification (Roche, cat. no. 07960140001). Gene Expression libraries were sequenced separately on the Illumina NovaSeq X using the following gene expression sequencing parameters; for snL-SVZ samples Read 1:51 cycles, Read 2: 51 cycles, Index 1:8 cycles, Index 2:24 cycles, for snCC samples Read 1:28 cycles, Read 2: 90 cycles, Index 1:10 cycles, Index 2:10 cycles.

snRNA-seq Analysis

Both snRNA sequencing datasets (snL-SVZ and snCC) were analyzed individually and pooled together by dataset for analysis via Seurat (version 5.3.0, Ubuntu 24.04) (164) in R (version 4.5.0, Ubuntu 24.04). Events were subsetted for nuclei with greater than 1000 but less than 25000 RNA counts. Objects initially underwent SCTransform and were then merged and layer integration was performed using RPCAIntegration and SCT normalisation. Following normalisation cells were clustered and dimensional reduction was completed by generating a Uniform Manifold Approximation and Projection (UMAP) using 50 dimensions and a resolution of 0.8 with otherwise default parameters. Cell type annotation was conducted by expression of marker genes, clusters were confirmed using the online database ACT (165), and the datasets were later subsetted for analysis of ependymal cells and microglia (snL-SVZ) or microglia and neural precursor cells (NPC) (snCC).

Identification of differentially expressed genes (DEGs) for microglia and ependymal cells were conducted using the *FindMarkers* function within the Seurat R package. Statistical significance was determined using a non-parametric Wilcoxon rank-sum test. To eliminate low-abundance backgrounds and maximize statistical power, genes were subjected to a pre-filtering minimum detection threshold min.pct = 0.1 as default, min.pct=0.05 was used for ependymal cell DEG analysis due to a lower overall nuclei number. Raw p-values were adjusted for multiple testing using a Bonferroni correction based on all features in the dataset. To evaluate gene expression changes in NPCs we choose to use pseudobulk to account for the large difference in nuclei number between genotypes. NPCs were subsetted from the snRNA-seq dataset using Seurat R package. Raw RNA counts were aggregated for each biological sample (orig.ident) using the *AggregateExpression* function to generate a sample level pseudobulk count matrix. Differential expression testing was performed using DESeq2 Bioconductor package after removal of genes with fewer than 10 total reads. Expression changes were modeled as a function of genotype with Ctrl samples defined at the reference baseline. Hypothesis testing was conducted using the Wald test, and the resulting *p*-values were adjusted for multiple testing using the Benjamini-Hochberg False Discovery Rate (FDR) method. DEGs were defined with a p adjusted value of < 0.05 and LogFC $>|1.5|$. Gene ontology metrics for DEGs were determined by inputting identified DEGs into the Metascape database (66). Visualization of differential gene

expression profiles was modeled using Enhanced Volcano Bioconductor package. Genes were defined as significantly differentially expressed if they demonstrated a strict Bonferroni-adjusted p-value < 0.05 paired with an absolute average log2 Fold-change >|1.5|.

Prior to cell-cell communication analysis, neural progenitor cells (NPCs) and microglia were independently isolated by subsetting the parent single-nuclei dataset (snCC) and subjected to standard downstream unsupervised UMAP clustering. NPC and microglia populations were identified by known marker genes and labeled accordingly. To mitigate cell-count bias and ensure balanced representation across biological replicates, the cell populations were randomly down sampled within each genotype to match the lowest common cell number baseline. Intercellular communication networks were robustly modeled using the LIANA R package, an ensemble framework for single-cell ligand-receptor analysis (112). Molecular interactions were mapped against the curated MouseConsensus database to guarantee species-specific relevance. To minimize technical noise and remove low-abundance backgrounds, a strict expression threshold was applied (expr_prop = 0.1), which required both the ligand and its cognate receptor to be actively detected in at least 10% of the cells within their respective cluster groups to be evaluated. Individual scoring methods computed by LIANA were subsequently synthesized and consolidated into an ensemble rank framework using the *liana_aggregate* function. To dissect specific paracrine and autocrine signaling alterations driven by the Ankrd11^{nscKO} NPCs, directional cell-cell crosstalk was profiled between defined source and target communities. The analysis focused on interactions where NPCs served as the signal senders (Sources: NPC_nscKO or NPC_Ctrl) and microglia served as the signal receivers (Targets: combined Microglia_nscKO and Microglia_Ctrl). Significant shifts in ligand-receptor aggregate rank were identified by an absolute rank shift ≥ 0.01 between NPC_ctrl and NPC_nscKO sources. When a single ligand paired with multiple receptors, only the partner yielding the strongest (lowest) aggregate rank was selected. The top 15 interactions, by overall baseline consensus rank, were visualized on a coordinate dumbbell plot.

Data availability

RNA sequencing datasets will be uploaded to the GEO omnibus prior to publication.

Acknowledgements

We thank the Mouse Imaging Centre (Toronto, Canada) for acquiring the magnetic resonance images for this study. We thank Dr. Kin Chan of the Network Biology Collaborative Centre Next-Generation Sequencing Facility (RRID: SCR_025385) at the Lunenfeld-Tanenbaum Research Institute for the Bulk RNASeq service. The facility is supported by the Canada Foundation for Innovation and the Ontario Government. We thank Dr. Troy Ketela from Princes Margaret Genomics Center (Toronto, Canada), https://www.pmgenomics.ca/pmgenomics/, for the snRNAseq service. We thank Dr. Kacie Norton at the Advanced Microscopy Facility (University of Alberta) for the use of the scanning electron microscope. We thank Drs. Andrew Simmonds and Sarah Hughes for the use of the flourescent stereoscope for live imaging and the confocal microscope for whole mount imaging, respectively. We also would like to thank Drs. Jo Anne Stratton, Sarah Hughes, and Ordan Lehmann for advice and critical reading of the manuscript.

Authors' contributions

Conceptualization, KG and AV. Methodology, KG, DH, SAY and AV. Formal analysis, KG, DH. Investigation, KG, DH, and AV. Resources, AV. Writing—original draft, KG. Writing—review and editing, AV. Supervision, AV. Funding acquisition, AV.

Funding

KG was supported by the Women and Children's Health Research Institute (WCHRI) Graduate studentship, the Andrew Stewart Memorial Graduate Prize, the Violet Kilburn Award, and the Natural Sciences and Engineering Research Council (NSERC) Canada Graduate Scholarship—Master's level. This work was supported by awards from The Scottish Rite Charitable Foundation of Canada and Killam Trusts awarded to AV. AV was also supported by the Canada Research Chair in Neural Stem Cell Biology and Sloan Research Fellowship in Neuroscience. DH was supported by a Research Excellence Postdoctoral Fellowship. Work in SAY's lab is supported by grants from NSERC and the Canadian Institutes for Health Research.

References

1. Kahle KT, Klinge PM, Koschnitzky JE, Kulkarni AV, MacAulay N, Robinson S, et al. Paediatric hydrocephalus. Nature Reviews Disease Primers. 2024;10(1):35.
2. Anwar F, Zhang K, Sun C, Pang M, Zhou W, Li H, et al. Hydrocephalus: An update on latest progress in pathophysiological and therapeutic research. Biomed Pharmacother. 2024;181:117702.
3. Hale AT, Zhou B, Rajan A, Duy PQ, Goolam M, Alper SL, et al. Molecular hallmarks of hydrocephalus. Science translational medicine. 2025;17(801):eadq1810.
4. Koleva M, De Jesus O. Hydrocephalus. 2023.
5. Cinalli G, Spennato P, Nastro A, Aliberti F, Trischitta V, Ruggiero C, et al. Hydrocephalus in aqueductal stenosis. Childs Nerv Syst. 2011;27(10):1621-42.
6. Lin X, Liu B, Yang X, Yue X, Diao L, Wang J, et al. Genetic deletion of Rnd3 results in aqueductal stenosis leading to hydrocephalus through up-regulation of Notch signaling. Proceedings of the National Academy of Sciences of the United States of America. 2013;110(20):8236-41.
7. Munch TN, Hedley PL, Hagen CM, Baekvad-Hansen M, Geller F, Bybjerg-Grauholm J, et al. The genetic background of hydrocephalus in a population-based cohort: implication of ciliary involvement. Brain Commun. 2023;5(1):fcad004.
8. Duy PQ, Weise SC, Marini C, Li X-J, Liang D, Dahl PJ, et al. Impaired neurogenesis alters brain biomechanics in a neuroprogenitor-based genetic subtype of congenital hydrocephalus. Nature neuroscience. 2022;25(4):458-73.
9. Erblich B, Zhu L, Etgen AM, Dobrenis K, Pollard JW. Absence of colony stimulation factor-1 receptor results in loss of microglia, disrupted brain development and olfactory deficits. PloS one. 2011;6(10):e26317.
10. Garcia-Bonilla M, Castaneyra-Ruiz L, Zwick S, Talcott M, Otun A, Isaacs AM, et al. Acquired hydrocephalus is associated with neuroinflammation, progenitor loss, and cellular changes in the subventricular zone and periventricular white matter. Fluids Barriers CNS. 2022;19(1):17.
11. Spassky N, Merkle FT, Flames N, Tramontin AD, Garcia-Verdugo JM, Alvarez-Buylla A. Adult ependymal cells are postmitotic and are derived from radial glial cells during embryogenesis. The Journal of neuroscience : the official journal of the Society for Neuroscience. 2005;25(1):10-8.
12. Yuzwa SA, Borrett MJ, Innes BT, Voronova A, Ketela T, Kaplan DR, et al. Developmental Emergence of Adult Neural Stem Cells as Revealed by Single-Cell Transcriptional Profiling. Cell reports. 2017;21(13):3970-86.
13. Furutachi S, Miya H, Watanabe T, Kawai H, Yamasaki N, Harada Y, et al. Slowly dividing neural progenitors are an embryonic origin of adult neural stem cells. Nature neuroscience. 2015;18(5):657-65.
14. Kriegstein A, Alvarez-Buylla A. The glial nature of embryonic and adult neural stem cells. Annu Rev Neurosci. 2009;32:149-84.
15. Spector R, Robert Snodgrass S, Johanson CE. A balanced view of the cerebrospinal fluid composition and functions: Focus on adult humans. Experimental neurology. 2015;273(1090-2430 (Electronic)):57-68.
16. Hirota Y, Meunier A, Huang S, Shimozawa T, Yamada O, Kida YS, et al. Planar polarity of multiciliated ependymal cells involves the anterior migration of basal bodies regulated by non-muscle myosin II. Development (Cambridge, England). 2010;137(18):3037-46.
17. McClenahan FK, Sharma H, Shan X, Eyermann C, Colognato H. Dystroglycan Suppresses Notch to Regulate Stem Cell Niche Structure and Function in the Developing Postnatal Subventricular Zone. Developmental cell. 2016;38(5):548-66.

18. Gonzalez-Cano L, Fuertes-Alvarez S, Robledinos-Anton N, Bizy A, Villena-Cortes A, Farinas I, et al. p73 is required for ependymal cell maturation and neurogenic SVZ cytoarchitecture. Dev Neurobiol. 2016;76(7):730-47.
19. Boutin C, Labedan P, Dimidschstein J, Richard F, Cremer H, Andre P, et al. A dual role for planar cell polarity genes in ciliated cells. Proceedings of the National Academy of Sciences of the United States of America. 2014;111(30):E3129-38.
20. Mirzadeh Z, Han YG, Soriano-Navarro M, Garcia-Verdugo JM, Alvarez-Buylla A. Cilia organize ependymal planar polarity. The Journal of neuroscience : the official journal of the Society for Neuroscience. 2010;30(7):2600-10.
21. Ohata S, Nakatani J, Herranz-Perez V, Cheng J, Belinson H, Inubushi T, et al. Loss of Dishevelleds disrupts planar polarity in ependymal motile cilia and results in hydrocephalus. Neuron. 2014;83(3):558-71.
22. Fuertes-Alvarez S, Maeso-Alonso L, Villoch-Fernandez J, Wildung M, Martin-Lopez M, Marshall C, et al. p73 regulates ependymal planar cell polarity by modulating actin and microtubule cytoskeleton. Cell Death Dis. 2018;9(12):1183.
23. Groh AMR, Song YL, Tea F, Lu B, Huynh S, Afanasiev E, et al. Multiciliated ependymal cells: an update on biology and pathology in the adult brain. Acta neuropathologica. 2024;148(1):39.
24. Lim DA, Alvarez-Buylla A. The Adult Ventricular-Subventricular Zone (V-SVZ) and Olfactory Bulb (OB) Neurogenesis. Cold Spring Harb Perspect Biol. 2016;8(5).
25. Tong CK, Han YG, Shah JK, Obernier K, Guinto CD, Alvarez-Buylla A. Primary cilia are required in a unique subpopulation of neural progenitors. Proceedings of the National Academy of Sciences of the United States of America. 2014;111(34):12438-43.
26. Bressan C, Gengatharan A, Rodriguez-Aller R, Richter ML, Snapyan M, Fischer-Sternjak J, et al. Cilia beating of ependymal cells regulates adult neural stem cell quiescence via mechanical forces mediated by PKD1/2-TRPM3. Neuron. 2026.
27. Quaresima S, Istiaq A, Jono H, Cacci E, Ohta K, Lupo G. Assessing the Role of Ependymal and Vascular Cells as Sources of Extracellular Cues Regulating the Mouse Ventricular-Subventricular Zone Neurogenic Niche. Frontiers in cell and developmental biology. 2022;10:845567.
28. Luo J, Shook BA, Daniels SB, Conover JC. Subventricular zone-mediated ependyma repair in the adult mammalian brain. The Journal of neuroscience : the official journal of the Society for Neuroscience. 2008;28(14):3804-13.
29. Singh AK, Allington G, Viviano S, McGee S, Kiziltug E, Ma S, et al. A novel SMARCC1 BAFopathy implicates neural progenitor epigenetic dysregulation in human hydrocephalus. Brain : a journal of neurology. 2024;147(4):1553-70.
30. Weiss K, Lazar HP, Kurolap A, Martinez AF, Paperna T, Cohen L, et al. The CHD4-related syndrome: a comprehensive investigation of the clinical spectrum, genotype–phenotype correlations, and molecular basis. Genetics in Medicine. 2020;22(2):389-97.
31. Holdhof D, Schoof M, Hellwig M, Holdhof NH, Niesen J, Schuller U. hGFAP-Positive Stem Cells Depend on Brg1 for Proper Formation of Cerebral and Cerebellar Structures. Cereb Cortex. 2020;30(3):1382-92.
32. Zhang A, Yeung PL, Li CW, Tsai SC, Dinh GK, Wu X, et al. Identification of a novel family of ankyrin repeats containing cofactors for p160 nuclear receptor coactivators. The Journal of biological chemistry. 2004;279(32):33799-805.
33. Li CW, Dinh GK, Zhang A, Chen JD. Ankyrin repeats-containing cofactors interact with ADA3 and modulate its co-activator function. The Biochemical journal. 2008;413(2):349-57.

34. Gallagher D, Voronova A, Zander Mark A, Cancino Gonzalo I, Bramall A, Krause Matthew P, et al. Ankrd11 Is a Chromatin Regulator Involved in Autism that Is Essential for Neural Development. Developmental cell. 2015;32(1):31-42.
35. Satterstrom FK, Kosmicki JA, Wang J, Breen MS, De Rubeis S, An JY, et al. Large-Scale Exome Sequencing Study Implicates Both Developmental and Functional Changes in the Neurobiology of Autism. Cell. 2020;180(3):568-84.e23.
36. Low K, Ashraf T, Canham N, Clayton-Smith J, Deshpande C, Donaldson A, et al. Clinical and genetic aspects of KBG syndrome. American Journal of Medical Genetics Part A. 2016;170(11):2835-46.
37. Willemsen MH, Fernandez BA, Bacino CA, Gerkes E, Brouwer APMd, Pfundt R, et al. Identification of ANKRD11 and ZNF778 as candidate genes for autism and variable cognitive impairment in the novel 16q24.3 microdeletion syndrome. European Journal of Human Genetics. 2010;18(4):429-35.
38. Peluso F, Caraffi SG, Contro G, Valeri L, Napoli M, Carboni G, et al. Deep phenotyping of the neuroimaging and skeletal features in KBG syndrome: a study of 53 patients and review of the literature. J Med Genet. 2023.
39. Su S, Ma J, Zhang Q, Hu W, Ren Y, Zhang W, et al. Insights into ANKRD11-related epilepsy from 163 people. Epilepsia. 2026.
40. Jing XY, Yu QX, Zhen L, Xiao ZQ, Li DZ. Prenatal Diagnosis of KBG Syndrome: Phenotypic and Genotypic Features of 12 Fetal Cases With the Disorder. Prenat Diagn. 2025.
41. Yang X, Ding H, Hu R, Liu L, Huang W, Lu J. Prenatal Genetic and Sonographic Features of KBG Syndrome: A Cohort Study of 19 Fetal Cases. Prenat Diagn. 2026;n/a(n/a).
42. Goodkey K, Wischmeijer A, Perrin L, Watson AES, Qureshi L, Cordelli DM, et al. Olfactory bulb anomalies in KBG syndrome mouse model and patients. BMC medicine. 2024;22(1):158.
43. Roth DM, Baddam P, Lin H, Vidal-García M, Aponte JD, De Souza ST, et al. The Chromatin Regulator Ankrd11 Controls Palate and Cranial Bone Development. Frontiers in cell and developmental biology. 2021;9:645386.
44. Kibalnyk Y, Noble R, Alexiou M, Poverennaya I, Dittmann N, Greenwell A, et al. Ankrd11, a chromatin regulator and a KBG syndrome risk gene, is a critical regulator of cardiac neural crest cell biology and heart development. Research Square; 2023.
45. Imayoshi I, Ohtsuka T, Metzger D, Chambon P, Kageyama R. Temporal regulation of Cre recombinase activity in neural stem cells. Genesis. 2006;44(5):233-8.
46. Reynolds BA, Weiss S. Generation of neurons and astrocytes from isolated cells of the adult mammalian central nervous system. Science (New York, NY). 1992;255(5052):1707-10.
47. Dittmann NL, Torabi P, Watson AES, Yuzwa SA, Voronova A. Culture Protocol and Transcriptomic Analysis of Murine SVZ NPCs and OPCs. Stem Cell Rev Rep. 2023;19(4):983-1000.
48. Ellis P, Fagan BM, Magness ST, Hutton S, Taranova O, Hayashi S, et al. SOX2, a Persistent Marker for Multipotential Neural Stem Cells Derived from Embryonic Stem Cells, the Embryo or the Adult. Developmental neuroscience. 2005;26(2-4):148-65.
49. Lee DR, Rhodes C, Mitra A, Zhang Y, Maric D, Dale RK, et al. Transcriptional heterogeneity of ventricular zone cells in the ganglionic eminences of the mouse forebrain. eLife. 2022;11.
50. Imai Y, Ibata I, Ito D, Ohsawa K, Kohsaka S. A novel gene iba1 in the major histocompatibility complex class III region encoding an EF hand protein expressed in a monocytic lineage. Biochemical and biophysical research communications. 1996;224(3):855-62.
51. Ito D, Imai Y, Ohsawa K, Nakajima K, Fukuuchi Y, Kohsaka S. Microglia-specific localisation of a novel calcium binding protein, Iba1. Brain Res Mol Brain Res. 1998;57(1):1-9.
52. Ernst C, Christie BR. Isolectin-IB 4 as a vascular stain for the study of adult neurogenesis. J Neurosci Methods. 2006;150(1):138-42.

53. Alliot F, Godin I, Pessac B. Microglia derive from progenitors, originating from the yolk sac, and which proliferate in the brain. Brain Res Dev Brain Res. 1999;117(2):145-52.
54. Aquino JB, Sierra R, Montaldo LA. Diverse cellular origins of adult blood vascular endothelial cells. Developmental biology. 2021;477(1095-564X (Electronic)):117-32.
55. Di Bella DJ, Habibi E, Stickels RR, Scalia G, Brown J, Yadollahpour P, et al. Molecular logic of cellular diversification in the mouse cerebral cortex. Nature. 2021;595(7868):554-9.
56. Finn R, Evans CC, Lee L. Strain-dependent brain defects in mouse models of primary ciliary dyskinesia with mutations in Pcdp1 and Spef2. Neuroscience. 2014;277:552-67.
57. Jimenez AJ, Tome M, Paez P, Wagner C, Rodriguez S, Fernandez-Llebrez P, et al. A programmed ependymal denudation precedes congenital hydrocephalus in the hyh mutant mouse. Journal of neuropathology and experimental neurology. 2001;60(11):1105-19.
58. Harkins D, Harvey TJ, Atterton C, Miller I, Currey L, Oishi S, et al. Hydrocephalus in Nfix(-/-) Mice Is Underpinned by Changes in Ependymal Cell Physiology. Cells. 2022;11(15).
59. Banizs B, Pike MM, Millican CL, Ferguson WB, Komlosi P, Sheetz J, et al. Dysfunctional cilia lead to altered ependyma and choroid plexus function, and result in the formation of hydrocephalus. Development (Cambridge, England). 2005;132(23):5329-39.
60. Muniz-Talavera H, Schmidt JV. The mouse Jhy gene regulates ependymal cell differentiation and ciliogenesis. PloS one. 2017;12(12):e0184957.
61. Crowley LC, Waterhouse NJ. Detecting Cleaved Caspase-3 in Apoptotic Cells by Flow Cytometry. Cold Spring Harb Protoc. 2016;2016(11).
62. Redmond SA, Figueres-Onate M, Obernier K, Nascimento MA, Parraguez JI, Lopez-Mascaraque L, et al. Development of Ependymal and Postnatal Neural Stem Cells and Their Origin from a Common Embryonic Progenitor. Cell reports. 2019;27(2):429-41 e3.
63. Mirzadeh Z, Merkle FT, Soriano-Navarro M, Garcia-Verdugo JM, Alvarez-Buylla A. Neural stem cells confer unique pinwheel architecture to the ventricular surface in neurogenic regions of the adult brain. Cell stem cell. 2008;3(3):265-78.
64. Mirzadeh Z, Doetsch F, Sawamoto K, Wichterle H, Alvarez-Buylla A. The subventricular zone en-face: wholemount staining and ependymal flow. Journal of visualized experiments : JoVE. 2010(39).
65. MacDonald A, Lu B, Caron M, Caporicci-Dinucci N, Hatrock D, Petrecca K, et al. Single Cell Transcriptomics of Ependymal Cells Across Age, Region and Species Reveals Cilia-Related and Metal Ion Regulatory Roles as Major Conserved Ependymal Cell Functions. Frontiers in cellular neuroscience. 2021;15:703951.
66. Zhou Y, Zhou B, Pache L, Chang M, Khodabakhshi AH, Tanaseichuk O, et al. Metascape provides a biologist-oriented resource for the analysis of systems-level datasets. Nature communications. 2019;10(1):1523.
67. Nagata Y, Bundo M, Sugiura S, Kamita M, Ono M, Hattori K, et al. PTPRQ as a potential biomarker for idiopathic normal pressure hydrocephalus. Molecular medicine reports. 2017;16(3):3034-40.
68. Zhang K, Xin X, Liu J, Hou B, Qu P, Xu X, et al. Whole Exome Sequencing Identifies Novel Splicing Variants in the PTPRQ Gene and Their Mechanisms in Autosomal Recessive Non-Syndromic Hearing Loss. J Otol. 2025;20(3):204-9.
69. Xu Z, Tavakoli A, Kulasooriya S, Liu H, Tu S, Bloom C, et al. The dual molecular identity of vestibular kinocilia bridges structural and functional traits of primary and motile cilia. eLife. 2026;14(2050-084X (Electronic)).
70. Higginbotham H, Guo J, Yokota Y, Umberger NL, Su CY, Li J, et al. Arl13b-regulated cilia activities are essential for polarized radial glial scaffold formation. Nature neuroscience. 2013;16(8):1000-7.

71. Soares R, Ribeiro FF, Lourenco DM, Rodrigues RS, Moreira JB, Sebastiao AM, et al. The neurosphere assay: an effective in vitro technique to study neural stem cells. Neural regeneration research. 2021;16(11):2229-31.
72. Zhang Q, Wu X, Fan Y, Zhang H, Yin M, Xue X, et al. Characterizing progenitor cells in developing and injured spinal cord: Insights from single-nucleus transcriptomics and lineage tracing. Proceedings of the National Academy of Sciences of the United States of America. 2025;122(2):e2413140122.
73. Sahu SK, Fritz A, Tiwari N, Kovacs Z, Pouya A, Wullner V, et al. TOX3 regulates neural progenitor identity. Biochim Biophys Acta. 2016;1859(7):833-40.
74. Cao X, Pfaff SL, Gage FH. YAP regulates neural progenitor cell number via the TEA domain transcription factor. Genes & development. 2008;22(23):3320-34.
75. Murphy AE, Skene NG. A balanced measure shows superior performance of pseudobulk methods in single-cell RNA-sequencing analysis. Nature communications. 2022;13(1):7851.
76. Ramaglia V, Hughes TR, Donev RM, Ruseva MM, Wu X, Huitinga I, et al. C3-dependent mechanism of microglial priming relevant to multiple sclerosis. Proceedings of the National Academy of Sciences of the United States of America. 2012;109(3):965-70.
77. Vukojicic A, Delestree N, Fletcher EV, Pagiazitis JG, Sankaranarayanan S, Yednock TA, et al. The Classical Complement Pathway Mediates Microglia-Dependent Remodeling of Spinal Motor Circuits during Development and in SMA. Cell reports. 2019;29(10):3087-100 e7.
78. Zhang W, Wang J, Ji J, Wang P, Yuan G, Fang S, et al. Glioblastoma cells secrete ICAM1 via FASN signaling to promote glioma-associated macrophage infiltration. Cell Signal. 2025;132:111823.
79. Mayo L, Jacob-Hirsch J, Amariglio N, Rechavi G, Moutin MJ, Lund FE, et al. Dual role of CD38 in microglial activation and activation-induced cell death. Journal of immunology (Baltimore, Md : 1950). 2008;181(1):92-103.
80. Vazquez C, Negatu SG, Bannerman CD, Sriram S, Ming GL, Jurado KA. Antiviral immunity within neural stem cells distinguishes Enterovirus-D68 strain differences in forebrain organoids. Journal of neuroinflammation. 2024;21(1):288.
81. Park B, Nicaise AM, Tsitsipatis D, Pirvan L, Zucha D, Munteanu A, et al. Integrated omics reveals disease-associated radial glia-like cells with epigenetically dysregulated interferon response in multiple sclerosis. Neuron. 2025;113(24):4158-77 e10.
82. Pillat MM, Ayupe AC, Juvenal G, Meinerz C, Glaser T, da Silva Pellegrina DV, et al. Differentiated Embryonic Neurospheres from Familial Alzheimer's Disease Model Show Innate Immune and Glial Cell Responses. Stem Cell Rev Rep. 2023;19(6):1800-11.
83. Deren KE, Packer M, Forsyth J, Milash B, Abdullah OM, Hsu EW, et al. Reactive astrocytosis, microgliosis and inflammation in rats with neonatal hydrocephalus. Experimental neurology. 2010;226(1):110-9.
84. Lattke M, Magnutzki A, Walther P, Wirth T, Baumann B. Nuclear factor kappaB activation impairs ependymal ciliogenesis and links neuroinflammation to hydrocephalus formation. The Journal of neuroscience : the official journal of the Society for Neuroscience. 2012;32(34):11511-23.
85. Goulding DS, Vogel RC, Pandya CD, Shula C, Gensel JC, Mangano FT, et al. Neonatal hydrocephalus leads to white matter neuroinflammation and injury in the corpus callosum of Ccdc39 hydrocephalic mice. J Neurosurg Pediatr. 2020:1-8.
86. Brown FN, Iwasawa E, Shula C, Fugate EM, Lindquist DM, Mangano FT, et al. Early postnatal microglial ablation in the Ccdc39 mouse model reveals adverse effects on brain development and in neonatal hydrocephalus. Fluids Barriers CNS. 2023;20(1):42.

87. Barry-Carroll L, Greulich P, Marshall AR, Riecken K, Fehse B, Askew KE, et al. Microglia colonize the developing brain by clonal expansion of highly proliferative progenitors, following allometric scaling. Cell reports. 2023;42(5):112425.
88. Hattori Y, Kato D, Murayama F, Koike S, Asai H, Yamasaki A, et al. CD206(+) macrophages transventricularly infiltrate the early embryonic cerebral wall to differentiate into microglia. Cell reports. 2023;42(2):112092.
89. Hammond BP, Manek R, Kerr BJ, Macauley MS, Plemel JR. Regulation of microglia population dynamics throughout development, health, and disease. Glia. 2021;69(12):2771-97.
90. Li Q, Cheng Z, Zhou L, Darmanis S, Neff NF, Okamoto J, et al. Developmental Heterogeneity of Microglia and Brain Myeloid Cells Revealed by Deep Single-Cell RNA Sequencing. Neuron. 2019;101(2):207-23 e10.
91. Matcovitch-Natan O, Winter DR, Giladi A, Vargas Aguilar S, Spinrad A, Sarrazin S, et al. Microglia development follows a stepwise program to regulate brain homeostasis. Science (New York, NY). 2016;353(6301):aad8670.
92. Keren-Shaul H, Spinrad A, Weiner A, Matcovitch-Natan O, Dvir-Szternfeld R, Ulland TK, et al. A Unique Microglia Type Associated with Restricting Development of Alzheimer's Disease. Cell. 2017;169(7):1276-90 e17.
93. Cheng YH, Ho MS. Disease-associated microglia in neurodegenerative diseases: Friend or foe? PLoS Biol. 2025;23(10):e3003426.
94. Liwang JK, Kronman FN, Pi HJ, Wu YT, Vanselow DJ, Manjila SB, et al. epDevAtlas: mapping GABAergic cells and microglia in the early postnatal mouse brain. Nature communications. 2025;16(1):9538.
95. Hagemeyer N, Hanft KM, Akriditou MA, Unger N, Park ES, Stanley ER, et al. Microglia contribute to normal myelinogenesis and to oligodendrocyte progenitor maintenance during adulthood. Acta neuropathologica. 2017;134(3):441-58.
96. Butovsky O, Weiner HL. Microglial signatures and their role in health and disease. Nature reviews Neuroscience. 2018;19(10):622-35.
97. Satoh J, Kino Y, Asahina N, Takitani M, Miyoshi J, Ishida T, et al. TMEM119 marks a subset of microglia in the human brain. Neuropathology. 2016;36(1):39-49.
98. Nath S, Martinez Santamaria JC, Chu YH, Choi JS, Conforti P, Lin JD, et al. Interaction between subventricular zone microglia and neural stem cells impacts the neurogenic response in a mouse model of cortical ischemic stroke. Nature communications. 2024;15(1):9095.
99. Krasemann S, Madore C, Cialic R, Baufeld C, Calcagno N, El Fatimy R, et al. The TREM2-APOE Pathway Drives the Transcriptional Phenotype of Dysfunctional Microglia in Neurodegenerative Diseases. Immunity. 2017;47(3):566-81 e9.
100. Bernard A, Eggstein C, Tang L, Keller M, Korner A, Mirakaj V, et al. Plexin C1 influences immune response to intracellular LPS and survival in murine sepsis. J Biomed Sci. 2024;31(1):82.
101. Yoo H, Nakahama T, Sugihara R, Gao Y, Ishizawa Y, Yang J, et al. Aberrant multicellular interferon signaling underlies Adar1 mutation-driven Aicardi-Goutieres syndrome-like encephalopathy. Cell reports. 2026;45(4):117113.
102. Milinkeviciute G, Henningfield CM, Muniak MA, Chokr SM, Green KN, Cramer KS. Microglia Regulate Pruning of Specialized Synapses in the Auditory Brainstem. Front Neural Circuits. 2019;13:55.
103. Chokr SM, Milinkeviciute G, Jimenez GA, Abubakr H, Cramer KS. Long-term microglia depletion impairs synapse elimination and auditory brainstem function. Scientific reports. 2022;12(1):18521.

104. Tang J, Jila S, Luo T, Zhang B, Miao H, Feng H, et al. C3/C3aR inhibition alleviates GMH-IVH-induced hydrocephalus by preventing microglia-astrocyte interactions in neonatal rats. Neuropharmacology. 2022;205:108927.
105. Iwasawa E, Brown FN, Shula C, Emmert AS, Fugate EM, Lindquist D, et al. Suppression of microglial activation with anti-inflammatory drug bindarit enhances neural development in the shunt-treated neonatal hydrocephalus model rat. Experimental neurology. 2025;398:115608.
106. Iwasawa E, Brown FN, Shula C, Kahn F, Lee SH, Berta T, et al. The Anti-Inflammatory Agent Bindarit Attenuates the Impairment of Neural Development through Suppression of Microglial Activation in a Neonatal Hydrocephalus Mouse Model. The Journal of neuroscience : the official journal of the Society for Neuroscience. 2022;42(9):1820-44.
107. Zhang K, Wang H, Xu M, Frank JA, Luo J. Role of MCP-1 and CCR2 in ethanol-induced neuroinflammation and neurodegeneration in the developing brain. Journal of neuroinflammation. 2018;15(1):197.
108. Olopade FE, Shokunbi MT, Azeez IA, Andrioli A, Scambi I, Bentivoglio M. Neuroinflammatory Response in Chronic Hydrocephalus in Juvenile Rats. Neuroscience. 2019;419:14-22.
109. de Almeida MMA, Goodkey K, Voronova A. Regulation of microglia function by neural stem cells. Frontiers in cellular neuroscience. 2023;17:1130205.
110. Willis CM, Nicaise AM, Krzak G, Ionescu RB, Pappa V, D'Angelo A, et al. Soluble factors influencing the neural stem cell niche in brain physiology, inflammation, and aging. Experimental neurology. 2022;355(1090-2430 (Electronic)):114124.
111. Brousse B, Mercier O, Magalon K, Daian F, Durbec P, Cayre M. Endogenous neural stem cells modulate microglia and protect against demyelination. Stem cell reports. 2021;16(7):1792-804.
112. Dimitrov D, Schafer PSL, Farr E, Rodriguez-Mier P, Lobentanzer S, Badia IMP, et al. LIANA+ provides an all-in-one framework for cell-cell communication inference. Nature cell biology. 2024;26(9):1613-22.
113. Ryu JK, Cho T, Choi HB, Wang YT, McLarnon JG. Microglial VEGF receptor response is an integral chemotactic component in Alzheimer's disease pathology. The Journal of neuroscience : the official journal of the Society for Neuroscience. 2009;29(1):3-13.
114. Fernandez-Calle R, Vicente-Rodriguez M, Gramage E, Pita J, Perez-Garcia C, Ferrer-Alcon M, et al. Pleiotrophin regulates microglia-mediated neuroinflammation. Journal of neuroinflammation. 2017;14(1):46.
115. Fuller AD, Van Eldik LJ. MFG-E8 regulates microglial phagocytosis of apoptotic neurons. Journal of neuroimmune pharmacology : the official journal of the Society on NeuroImmune Pharmacology. 2008;3(4):246-56.
116. Li J, Brickler T, Banuelos A, Marjon K, Shcherbina A, Banerjee S, et al. Overexpression of CD47 is associated with brain overgrowth and 16p11.2 deletion syndrome. Proceedings of the National Academy of Sciences of the United States of America. 2021;118(15).
117. Couturier A, Bousquet E, Zhao M, Naud MC, Klein C, Jonet L, et al. Anti-vascular endothelial growth factor acts on retinal microglia/macrophage activation in a rat model of ocular inflammation. Mol Vis. 2014;20(1090-0535 (Electronic)):908-20.
118. Vural A, Nabar NR, Hwang I-Y, Sohn S, Park C, Karlsson MCI, et al. Gαi2 Signaling Regulates Inflammasome Priming and Cytokine Production by Biasing Macrophage Phenotype Determination. The Journal of Immunology. 2019;202(5):1510-20.
119. Lee IS, Jung K, Kim IS, Lee H, Kim M, Yun S, et al. Human neural stem cells alleviate Alzheimer-like pathology in a mouse model. Mol Neurodegener. 2015;10(1):38.

120. de Almeida MMA, Watson AES, Bibi S, Dittmann NL, Goodkey K, Sharafodinzadeh P, et al. Fractalkine enhances oligodendrocyte regeneration and remyelination in a demyelination mouse model. Stem cell reports. 2023;18(2):519-33.
121. Brugmans AK, Walter C, Moreno N, Gobel C, Holdhof D, de Faria FW, et al. A Carboxy-terminal Smarcb1 Point Mutation Induces Hydrocephalus Formation and Affects AP-1 and Neuronal Signalling Pathways in Mice. Cell Mol Neurobiol. 2023;43(7):3511-26.
122. Ninkovic J, Steiner-Mezzadri A, Jawerka M, Akinci U, Masserdotti G, Petricca S, et al. The BAF complex interacts with Pax6 in adult neural progenitors to establish a neurogenic cross-regulatory transcriptional network. Cell stem cell. 2013;13(4):403-18.
123. Vidovic D, Davila RA, Gronostajski RM, Harvey TJ, Piper M. Transcriptional regulation of ependymal cell maturation within the postnatal brain. Neural Dev. 2018;13(1):2.
124. Patir A, Fraser AM, Barnett MW, McTeir L, Rainger J, Davey MG, et al. The transcriptional signature associated with human motile cilia. Scientific reports. 2020;10(1):10814.
125. Sakaguchi H, Tokita J, Naoz M, Bowen-Pope D, Gov NS, Kachar B. Dynamic compartmentalization of protein tyrosine phosphatase receptor Q at the proximal end of stereocilia: implication of myosin VI-based transport. Cell Motil Cytoskeleton. 2008;65(7):528-38.
126. Nakajima M, Rauramaa T, Makinen PM, Hiltunen M, Herukka SK, Kokki M, et al. Protein tyrosine phosphatase receptor type Q in cerebrospinal fluid reflects ependymal cell dysfunction and is a potential biomarker for adult chronic hydrocephalus. European journal of neurology. 2021;28(2):389-400.
127. Yang J, Simonneau C, Kilker R, Oakley L, Byrne MD, Nichtova Z, et al. Murine MPDZ-linked hydrocephalus is caused by hyperpermeability of the choroid plexus. EMBO Mol Med. 2019;11(1):EMMM201809540.
128. Pourabdolhossein F, Gil-Perotin S, Garcia-Belda P, Dauphin A, Mozafari S, Tepavcevic V, et al. Inflammatory demyelination induces ependymal modifications concomitant to activation of adult (SVZ) stem cell proliferation. Glia. 2017;65(5):756-72.
129. Chard PS, Bleakman D, Christakos S, Fullmer CS, Miller RJ. Calcium buffering properties of calbindin D28k and parvalbumin in rat sensory neurones. The Journal of physiology. 1993;472(0022-3751 (Print)):341-57.
130. Liu T, Jin X, Prasad RM, Sari Y, Nauli SM. Three types of ependymal cells with intracellular calcium oscillation are characterized by distinct cilia beating properties. J Neurosci Res. 2014;92(9):1199-204.
131. Jimenez AJ, Garcia-Verdugo JM, Gonzalez CA, Batiz LF, Rodriguez-Perez LM, Paez P, et al. Disruption of the neurogenic niche in the subventricular zone of postnatal hydrocephalic hyh mice. Journal of neuropathology and experimental neurology. 2009;68(9):1006-20.
132. Takahashi H, Fujimoto T, Yaoi T, Fushiki S, Itoh K. Leukemia inhibitory factor shortens primary cilia by upregulating C-C motif chemokine 2 in human neural stem/progenitor cells. Genes to cells : devoted to molecular & cellular mechanisms. 2023;28(12):868-80.
133. Suciu SK, Caspary T. Cilia, neural development and disease. Seminars in Cell & Developmental Biology. 2021;110:34-42.
134. Lilja T, Heldring N, Hermanson O. Like a rolling histone: epigenetic regulation of neural stem cells and brain development by factors controlling histone acetylation and methylation. Biochim Biophys Acta. 2013;1830(2):2354-60.
135. Wilton DK, Mastro K, Heller MD, Gergits FW, Willing CR, Fahey JB, et al. Microglia and complement mediate early corticostriatal synapse loss and cognitive dysfunction in Huntington's disease. Nature medicine. 2023;29(11):2866-84.

136. Manocha GD, Floden AM, Rausch K, Kulas JA, McGregor BA, Rojanathammanee L, et al. APP Regulates Microglial Phenotype in a Mouse Model of Alzheimer's Disease. The Journal of neuroscience : the official journal of the Society for Neuroscience. 2016;36(32):8471-86.
137. DeSpenza T, Jr., Kiziltug E, Allington G, Barson DG, McGee S, O'Connor D, et al. PTEN mutations impair CSF dynamics and cortical networks by dysregulating periventricular neural progenitors. Nature neuroscience. 2025;28(3):536-57.
138. Lukowicz K, Grygier B, Basta-Kaim A. Emerging role of neural stem/progenitor cell secretome in brain inflammatory response modulation. Pharmacol Rep. 2025;77(4):907-20.
139. Gao B, Wang H, Hu S, Zhong K, Liu X, Deng Z, et al. Sox2-overexpressing neural stem cells alleviate ventricular enlargement and neurological dysfunction in posthemorrhagic hydrocephalus. Neural regeneration research. 2026;21(2):769-79.
140. Rojo R, Raper A, Ozdemir DD, Lefevre L, Grabert K, Wollscheid-Lengeling E, et al. Deletion of a Csf1r enhancer selectively impacts CSF1R expression and development of tissue macrophage populations. Nature communications. 2019;10(1):3215.
141. Jacquelin S, Maxwell E, Taylor I, Green E, O'Brien CJO, Jessen EE, et al. Homozygous kinase-dead Csf1r mutation in outbred mice reveals essential and redundant functions of tissue resident macrophages. J Leukoc Biol. 2026;118(6):qiag074.
142. Taylor I, Patkar OL, Liu Y, Jacquelin S, Ranpura G, Carter-Cusack D, et al. Repopulation of the brain with microglia-like cells following intraperitoneal bone marrow cell transfer in microglia-deficient mice. bioRxiv. 2025:2025.01.16.633478.
143. Wu KY, Tang FL, Lee D, Zhao Y, Song H, Zhu XJ, et al. Ependymal Vps35 Promotes Ependymal Cell Differentiation and Survival, Suppresses Microglial Activation, and Prevents Neonatal Hydrocephalus. The Journal of neuroscience : the official journal of the Society for Neuroscience. 2020;40(19):3862-79.
144. Dutra M, Covas da Silva S, da Silva Beggiora Marques P, Oliveira Amaral I, Funo de Souza SN, Dutra LA, et al. Celecoxib attenuates neuroinflammation, reactive astrogliosis and promotes neuroprotection in young rats with experimental hydrocephalus. J Chem Neuroanat. 2023;133:102344.
145. Cao Y, Liu C, Li G, Gao W, Tang H, Fan S, et al. Metformin Alleviates Delayed Hydrocephalus after Intraventricular Hemorrhage by Inhibiting Inflammation and Fibrosis. Transl Stroke Res. 2023;14(3):364-82.
146. Murphy D. Caesarean section and fostering. Methods Mol Biol. 1993;18(1940-6029 (Electronic)):177-8.
147. Cai Z, Wang G, Chen Y, He M. Caesarean Sectioning and Cross-Fostering of the Mouse. Bio-protocol. 2018;8(22):e3085.
148. Srinivas S, Watanabe T, Lin CS, William CM, Tanabe Y, Jessell TM, et al. Cre reporter strains produced by targeted insertion of EYFP and ECFP into the ROSA26 locus. BMC Dev Biol. 2001;1:4.
149. Watson AES, de Almeida MMA, Dittmann NL, Li Y, Torabi P, Footz T, et al. Fractalkine signaling regulates oligodendroglial cell genesis from SVZ precursor cells. Stem cell reports. 2021;16(8):1968-84.
150. Li Y, Dittmann NL, Eve A, Watson S, de Almeida MMA, Footz T, et al. Hepatoma Derived Growth Factor Enhances Oligodendrocyte Genesis from Subventricular Zone Precursor Cells. ASN Neuro. 2022;14(1759-0914 (Electronic)):17590914221086340.
151. Cahill LS, Laliberte CL, Ellegood J, Spring S, Gleave JA, Eede MC, et al. Preparation of fixed mouse brains for MRI. Neuroimage. 2012;60(2):933-9.
152. Yushkevich PA, Piven J, Hazlett HC, Smith RG, Ho S, Gee JC, et al. User-guided 3D active contour segmentation of anatomical structures: significantly improved efficiency and reliability. Neuroimage. 2006;31(3):1116-28.

153. Galleguillos D, Wang Q, Steinberg N, Zaidi A, Shrivastava G, Dhami K, et al. Anti-inflammatory role of GM1 and other gangliosides on microglia. Journal of neuroinflammation. 2022;19(1):9.
154. Bustin SA, Benes V, Garson JA, Hellemans J, Huggett J, Kubista M, et al. The MIQE guidelines: minimum information for publication of quantitative real-time PCR experiments. Clin Chem. 2009;55(4):611-22.
155. Livak KJ, Schmittgen TD. Analysis of relative gene expression data using real-time quantitative PCR and the 2(-Delta Delta C(T)) Method. Methods. 2001;25(4):402-8.
156. Hou CC, Li D, Berry BC, Zheng S, Carroll RS, Johnson MD, et al. Heterozygous FOXJ1 Mutations Cause Incomplete Ependymal Cell Differentiation and Communicating Hydrocephalus. Cell Mol Neurobiol. 2023;43(8):4103-16.
157. Schindelin J, Arganda-Carreras I, Frise E, Kaynig V, Longair M, Pietzsch T, et al. Fiji: an open-source platform for biological-image analysis. Nat Methods. 2012;9(7):676-82.
158. Stansak KL, Baum LD, Ghosh S, Thapa P, Vanga V, Walters BJ. PCP auto count: a novel Fiji/ImageJ plug-in for automated quantification of planar cell polarity and cell counting. Frontiers in cell and developmental biology. 2024;12:1394031.
159. Voronova A, Yuzwa SA, Wang BS, Zahr S, Syal C, Wang J, et al. Migrating Interneurons Secrete Fractalkine to Promote Oligodendrocyte Formation in the Developing Mammalian Brain. Neuron. 2017;94(3):500-16.e9.
160. Coles-Takabe BL, Brain I, Purpura KA, Karpowicz P, Zandstra PW, Morshead CM, et al. Don't look: growing clonal versus nonclonal neural stem cell colonies. Stem cells (Dayton, Ohio). 2008;26(11):2938-44.
161. Frankish A, Diekhans M, Jungreis I, Lagarde J, Loveland JE, Mudge JM, et al. Gencode 2021. Nucleic Acids Res. 2021;49(D1):D916-D23.
162. Liao Y, Smyth GK, Shi W. featureCounts: an efficient general purpose program for assigning sequence reads to genomic features. Bioinformatics. 2014;30(7):923-30.
163. Love MI, Huber W, Anders S. Moderated estimation of fold change and dispersion for RNA-seq data with DESeq2. Genome Biol. 2014;15(12):550.
164. Hao Y, Stuart T, Kowalski MH, Choudhary S, Hoffman P, Hartman A, et al. Dictionary learning for integrative, multimodal and scalable single-cell analysis. Nat Biotechnol. 2024;42(2):293-304.
165. Quan F, Liang X, Cheng M, Yang H, Liu K, He S, et al. Annotation of cell types (ACT): a convenient web server for cell type annotation. Genome Med. 2023;15(1):91.

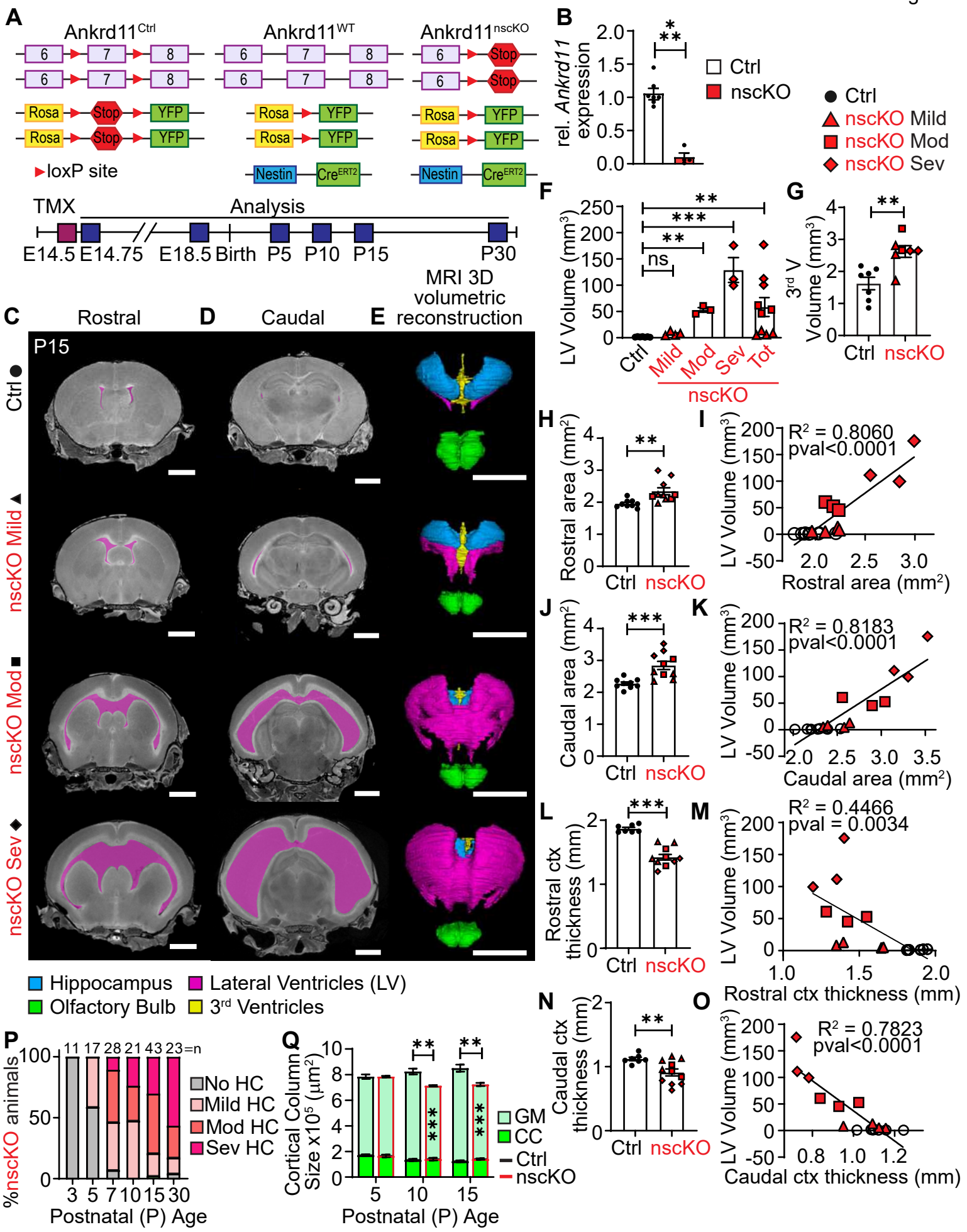
A
Ankrd11Ctrl
Ankrd11WT
Ankrd11nscKO
6
7
8
Stop
Rosa
YFP
loxP site
Nestin
CreERT2
TMX
Analysis
E14.5
E14.75
E18.5
Birth
P5
P10
P15
P30
B
rel. Ankrd11 expression
Ctrl
nscKO
nscKO Mild
nscKO Mod
nscKO Sev
C
Rostral
D
Caudal
E
MRI 3D volumetric reconstruction
P15
Ctrl
nscKO Mild
nscKO Mod
nscKO Sev
Hippocampus
Lateral Ventricles (LV)
Olfactory Bulb
3rd Ventricles
F
LV Volume (mm3)
ns
Mild
Mod
Sev
Tot
G
3rd V Volume (mm3)
H
Rostral area (mm2)
I
R2 = 0.8060
pval<0.0001
LV Volume (mm3)
Rostral area (mm2)
J
Caudal area (mm2)
K
R2 = 0.8183
pval<0.0001
Caudal area (mm2)
L
Rostral ctx thickness (mm)
M
R2 = 0.4466
pval = 0.0034
Rostral ctx thickness (mm)
N
Caudal ctx thickness (mm)
O
R2 = 0.7823
pval<0.0001
Caudal ctx thickness (mm)
P
11 17 28 21 43 23=n
%nscKO animals
No HC
Mild HC
Mod HC
Sev HC
Postnatal (P) Age
Q
Cortical Column Size x10^5 (µm2)
GM
CC
Ctrl
nscKO
Postnatal (P) Age

Figure 1. Loss of Ankrd11 in E14.5 NPCs results in postnatal progressive hydrocephalus. ***Please see associated Fig. S1.*** **A)** Schematic of Ankrd11$^{fl/fl}$;RosaYFP$^{stop/stop}$ (Ankrd11^{Ctrl}), Ankrd11$^{wt/wt}$;RosaYFP$^{stop/stop}$;NestinCre^{ERT2} (Ankrd11^{WT}) and Ankrd11$^{fl/fl}$;RosaYFP$^{stop/stop}$;NestinCre^{ERT2} (Ankrd11^{nscKO}) genotypes. Dams were injected at E14.5 with Tamoxifen (TMX) and embryos or pups collected from E14.75 to P30. **B)** Quantitative RT-PCR analysis of relative expression of *Ankrd11* mRNA in E15.5 cortical primary neurosphere cultures from Ankrd11^{Ctrl} and Ankrd11^{nscKO} embryos. Data normalized to *Gapdh* and calibrated against Ankrd11^{Ctrl} samples. **C-D)** Representative anatomically matched images of rostral (**C**) and caudal (**D**) coronal cross sections from MRI images of P15 Ankrd11^{Ctrl} and Ankrd11^{nscKO} brains. Lateral ventricles are pseudo colored in pink. **E)** Three-dimensional volumetric reconstruction of brain lateral ventricles (pink), 3rd ventricles (yellow), olfactory bulbs (green) and hippocampus (blue) from P15 Ankrd11^{Ctrl} and Ankrd11^{nscKO} MRI images. **F)** Quantification of lateral ventricles volume from E. Data are shown based on hydrocephalus severity (mild = triangle symbols, moderate [Mod] = square symbols, severe [Sev] = diamond symbols) and last column shows all Ankrd11^{nscKO} samples (Tot). **G)** Quantification of 3rd ventricle volume from (E). **H-K)** Quantification of rostral (**H**) and caudal (**J**) cortical area from (C-D) and its correlation to lateral ventricles volume (**I, K** respectively). **L-O)** Quantification of rostral (**L**) and caudal (**N**) cortical cortex thickness from (C-D) and its correlation to lateral ventricles volume (**M, O** respectively). **P)** Proportion of Ankrd11^{nscKO} mice with no hydrocephalus (HC) in grey, mild HC in pink, moderate HC in orange and severe HC in fuchsia at P3, P5, P7, P10, P15 and P30. Number of Ankrd11^{nscKO} mice at each timepoint is indicated at the top of the graph. **Q)** Quantification of cortical column size from postnatal rostral IHC sections, with corpus callosum (CC) size in bright green and grey matter (GM) size in pale green. n≥6 mice per genotype from at least two independent litters. Error bars represent SEM. Data were analyzed using linear regression (I, K, M, O), unpaired t-test (B, G, H, J, L, N), or one-way ANOVA with Tukey's post hoc test (F, Q). *p<0.05, **p<0.01, ***p<0.001. ns = not significant. Scale bars represent 2mm (C, D) and 5mm (E). Ctx=cortex, E=embryonic day, HC=hydrocephalus, LV=lateral ventricle, Mod=moderate, MRI=magnetic resonance imaging, P=postnatal day, Sev=severe, TMX=tamoxifen, Tot=total, V=ventricle

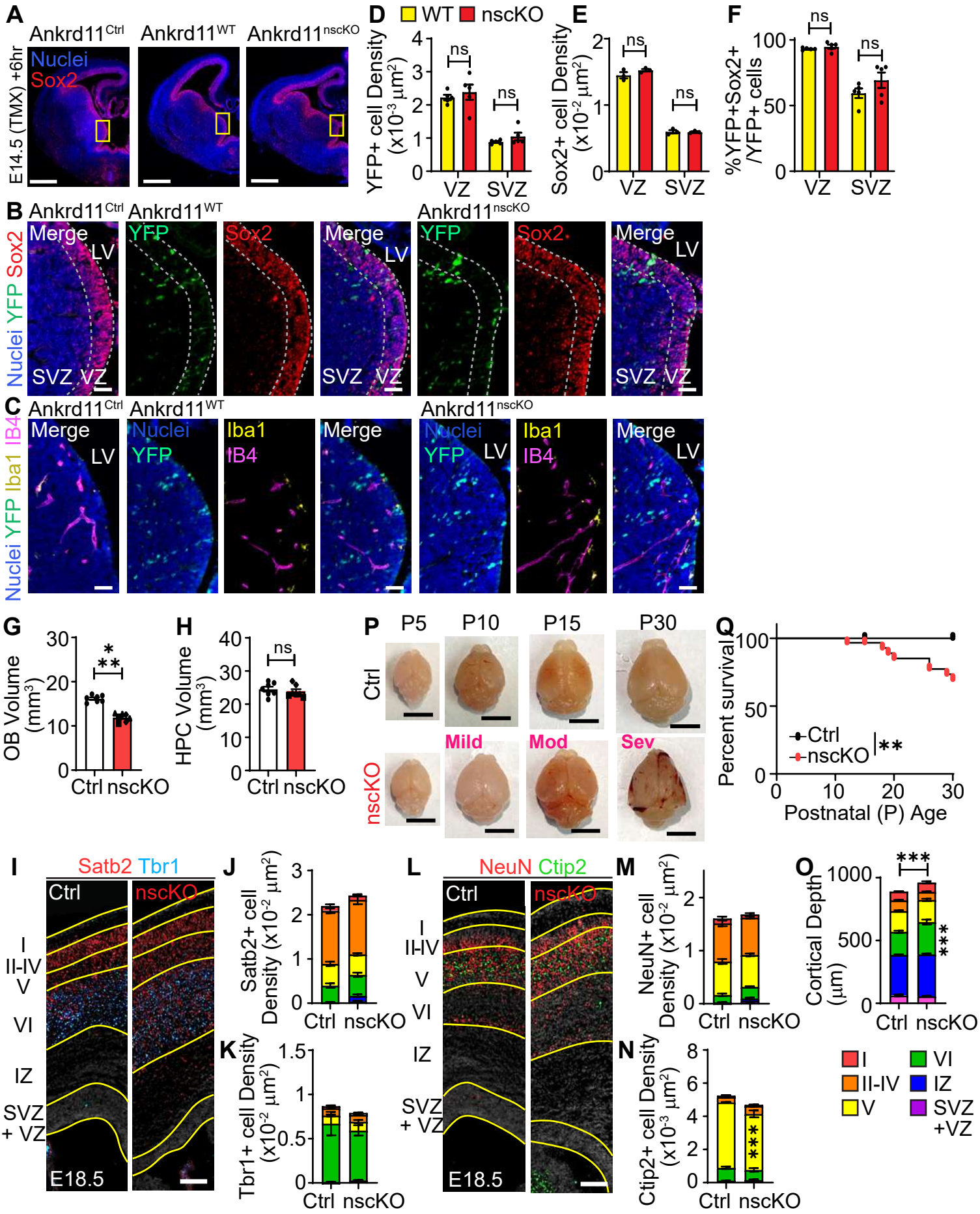
A
Ankrd11Ctrl
Ankrd11WT
Ankrd11nscKO
E14.5 (TMX) +6hr
Nuclei
Sox2
D
WT
nscKO
YFP+ cell Density (x10-3 µm2)
ns
VZ
SVZ
E
Sox2+ cell Density (x10-2 µm2)
F
%YFP+Sox2+ /YFP+ cells
B
Merge
YFP
Sox2
LV
SVZ
VZ
Nuclei YFP Sox2
C
Iba1
IB4
Nuclei YFP Iba1 IB4
G
OB Volume (mm3)
Ctrl
nscKO
H
HPC Volume (mm3)
P
P5
P10
P15
P30
Mild
Mod
Sev
Q
Percent survival
Postnatal (P) Age
I
Satb2 Tbr1
I
II-IV
V
VI
IZ
SVZ + VZ
E18.5
J
Satb2+ cell Density (x10-2 µm2)
K
Tbr1+ cell Density (x10-2 µm2)
L
NeuN Ctip2
M
NeuN+ cell Density (x10-2 µm2)
N
Ctip2+ cell Density (x10-3 µm2)
O
Cortical Depth (µm)
I
II-IV
V
VI
IZ
SVZ +VZ

Supplementary Figure S1. Validation of Ankrd11^{nscKO} model. ***Please see associated Fig. 1.*** **A)** Representative images of the E14.75 Ankrd11^{Ctrl}, Ankrd11^{WT}, and Ankrd11^{nscKO} forebrain, 6 hours post TMX injection at E14.5, immunostained for Sox2 (red) and counterstained with Hoechst (blue). Yellow box indicates crop region shown in B and C. **B)** High magnification representative images from insets in (A) immunostained for YFP (green) and Sox2 (red) and counterstained with Hoechst (blue). White dashed lines demarcate the VZ region. **C)** Representative images of Ankrd11^{Ctrl}, Ankrd11^{WT}, and Ankrd11^{nscKO} ventral forebrain immunostained for Hoechst (blue), YFP (green), Iba1 (yellow), and IB4 (pink). Approximate location of images is shown in (A). **D-F)** Quantification of (B) for YFP+ cell density **(D)**, Sox2+ cell density **(E)** and proportion of YFP+Sox2+ cells (% YFP+Sox2+/YFP+ cells) **(F)** in the VZ and SVZ regions. **G-H)** Quantification of olfactory bulb (OB) **(G)** and hippocampus (HPC) **(H)** volume from P15 MRI images shown in Fig. 1. **I)** Representative images of E18.5 rostral cortical columns from Ankrd11^{Ctrl} (Ctrl) and Ankrd11^{nscKO} (nscKO) brains immunostained for Satb2 (red) and Tbr1 (blue), counterstained for Hoechst (grey). Yellow lines demarcate cortical layers. **J-K)** Quantification of Satb2+ (**J**) and Tbr1+ (**K**) cell density in each cortical layer. **L)** Representative images of E18.5 rostral cortical columns immunostained for NeuN (red) and Ctip2 (green), counterstained for Hoechst (grey). Yellow lines demarcate cortical layers. **M-N)** Quantification of NeuN+ (**M**) and Ctip2+ (**N**) cell density in each cortical layer. **O)** Quantification of E18.5 cortical layer thickness. **P)** Representative images of Ankrd11^{nscKO} and Ankrd11^{Ctrl} brains at P5, P10, P15, and P30. **Q)** Survival curve of Ankrd11^{nscKO} and Ankrd11^{Ctrl} mice up to P30. n≥4 mice per genotype from at least two independent litters. Error bars represent SEM. Data were analyzed using two-way ANOVA Tukey's multiple comparisons post hoc test (D, E, F, J, K, M, N, O), unpaired t-test (G, H), and Log-rank (Mantel-Cox) test (Q). *$p<0.05$, **$p<0.01$, ***$p<0.001$. ns=not significant. Scale bars represent 500 μm (A), 200 μm (I and L), 50 μm (B and C) and 5 mm (P). E=embryonic day, HPC=hippocampus, LV=lateral ventricle, Mod=moderate, MRI=magnetic resonance imaging, OB=olfactory bulb, P=postnatal day, Sev=severe, SVZ=subventricular zone, TMX=tamoxifen, VZ=ventricular zone.

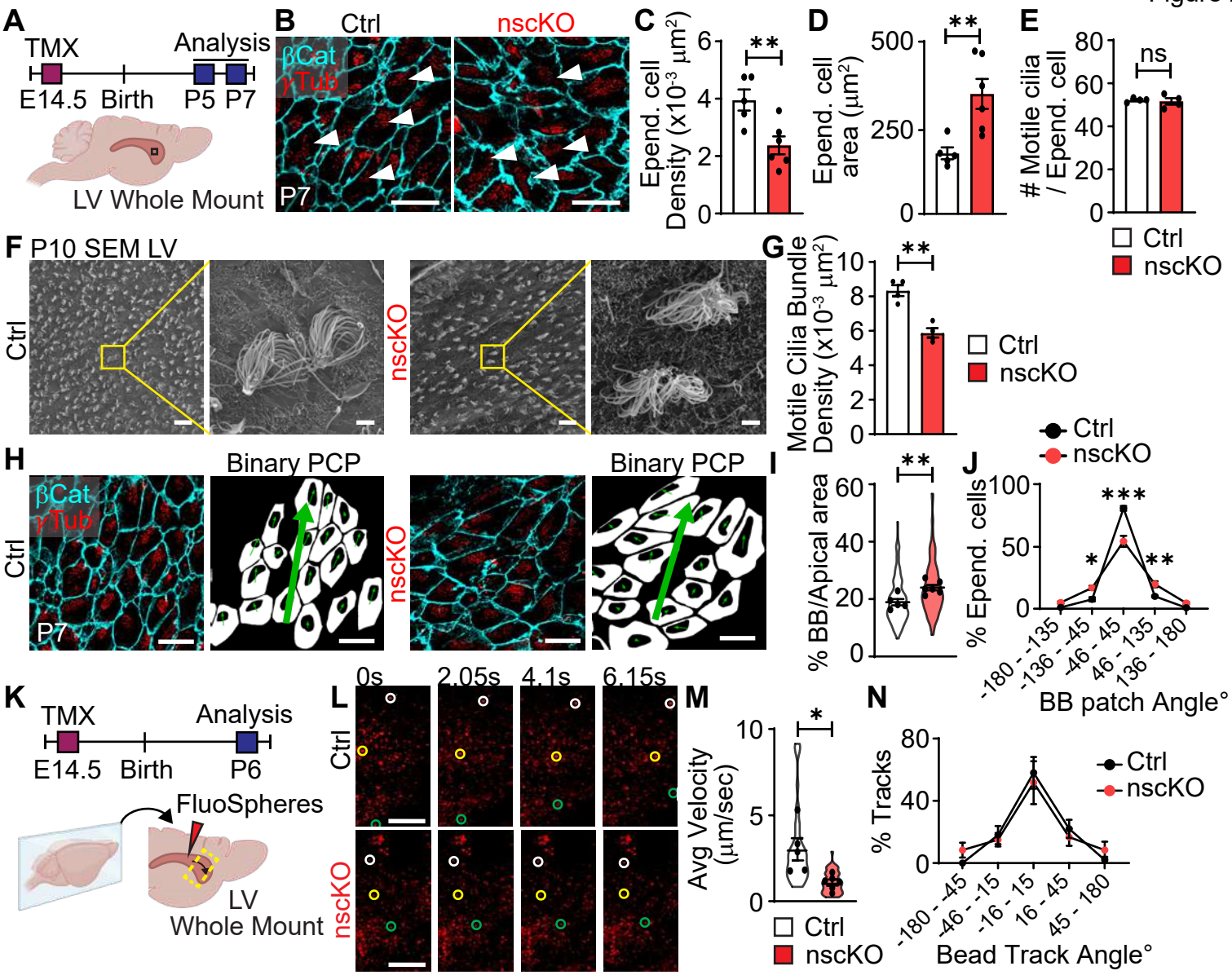
A
TMX
Analysis
E14.5 Birth P5 P7
LV Whole Mount
B
Ctrl
nscKO
βCat
γTub
P7
C
Epend. cell Density (x10-3 µm2)
D
Epend. cell area (µm2)
E
Motile cilia / Epend. cell
ns
Ctrl
nscKO
F P10 SEM LV
Ctrl
nscKO
G
Motile Cilia Bundle Density (x10-3 µm2)
H
Binary PCP
I
% BB/Apical area
J
% Epend. cells
BB patch Angle°
K
TMX
Analysis
E14.5 Birth P6
FluoSpheres
LV
Whole Mount
L
0s
2.05s
4.1s
6.15s
M
Avg Velocity (µm/sec)
N
% Tracks
Bead Track Angle°
O
snL-SVZ Ependymal
(Foxj1, Vim, Cfap44, Pifo, Dynlrb2)
76139 nuclei
umap_1
umap_2
P
Ependymal subset
632 nuclei
R
nscKO vs Ctrl
NS p-value Log2FC p-value+Log2FC
10 genes
15 genes
-Log10P
Log2FC
12642 variables
Neat1
Ptprq
Rmst
Calb1
Folr1
Dusp1
Gfap
Ecm1
Ttr
S
Ctrl1
Ctrl2
nscKOmild
nscKOmod
Slc25a21 Fam81b Plscr2 Hmcn1 Zfp536 Ccdc3 Calb1 Tcerg1l Folr1 Rmst Ecm1 Erlin2 C4b Gfap Dusp1 Neat1 Nbl1 Ptprq Ttr Adarb2 Usp13 Scd1
T
reg of mononuclear cell migration
inner ear development
carboxylic acid transport
-Log10P

Figure 2. Loss of Ankrd11 in E14.5 NPCs results in reduced ependymal cell density with altered planar cell polarity, function, and transcriptomic profile. ***Please see associated Figs. S2, S3, Videos S1-2, and Table S1.*** **A)** Schematic of experimental design. TMX was injected at E14.5, and lateral ventricle (LV) wall whole mount (dark pink) were microdissected from Ankrd11^{Ctrl} and Ankrd11^{nscKO} mice at P5 and P7 (box indicates representative image location). **B)** Representative images of P7 LV whole mount immunostained for βcat (cyan) and γTub (red). Arrowheads point to ependymal cells with multiple γTub puncta. **C-E)** Quantification of ependymal cell density **(C)**, cell area **(D)**, and motile cilia (γTub) puncta per cell (**E)**. **F-G)** Representative images of scanning electron microscopy (SEM) micrographs from the P10 LV wall (**F**) and quantification of motile cilia bundle density (**G**). **H)** Representative images of P7 LV whole mount from Ankrd11^{Ctrl} and Ankrd11^{nscKO} mice, immunostained for βcat (cyan) and γTub (red), with binary planar cell polarity (PCP; white outline = apical cell, black = basal body [BB], small green arrow = apical-to-BB centroid vector, large green arrow = image average vector angle). Please also see Fig. S2L. **I-J)** Quantification of BB area relative to apical cell area (**I**) and proportion of ependymal cells with binned BB patch angles relative to the average vector angle (**J**). **K)** Schematic of P6 live FluoSphere (1 μm) bead tracking design following E14.5 TMX injection (dark pink = LV whole mount, red arrow = deposit area, black arrows = bead path, yellow box = ROI). **L-N)** Representative live video tracking screenshots over 6.15s (colored circles track individual beads; Videos S1, S2) (**L**), quantification of average bead velocity (**M**), and proportion of bead tracks binned by track angle relative to average 0° (**N**). **O)** FeaturePlot of combined expression for known ependymal marker genes (*Foxj1, Vim, Cfap44, Pifo, Dynlrb2*) from the P15 L-SVZ snRNA-seq dataset (snL-SVZ) UMAP. Please see associated Fig. S3. **P)** UMAP of ependymal nuclei subcluster split by genotype, with Ankrd11^{Ctrl} nuclei in blue and Ankrd11^{nscKO} nuclei in red. **R-T)** Volcano plot of DEGs between Ankrd11^{nscKO} vs Ankrd11^{Ctrl} snL-SVZ ependymal cells (**R;** red dots: padj≤0.05 Log2FC |1.5|; yellow box = genes submitted to GO analysis in (**T**)) and heatmap of DEGs split by animal (**S**). snL-SVZ dataset (panel O-T) is from four mice (two per genotype). Neither of the Ankrd11^{Ctrl} mice exhibited hydrocephalus, while one Ankrd11^{nscKO} mouse exhibited mild (n=1) and one mouse Ankrd11^{nscKO} exhibited moderate (n=1) hydrocephalus in each dataset. n≥4 mice per genotype from at least two independent litters for panels A-N. Error bars represent SEM. Data were analyzed using unpaired t-test (C, D, E, G, I, M) or multiple T-test (J and N). *p<0.05, **p<0.01, ***p<0.001. ns = not significant. Scale bars represent 200 μm (L), 20 μm (B, F [1000x], K), and 2 μm (F [10000x]). Avg=average, BB=basal body, DEG=differentially expressed genes, E=embryonic day, GO=gene ontology, L-SVZ=lateral subventricular zone, LV=lateral ventricle, P=postnatal day, SEM=scanning electron microscopy, snRNA-seq=single nucleus RNA sequencing, TMX=tamoxifen.

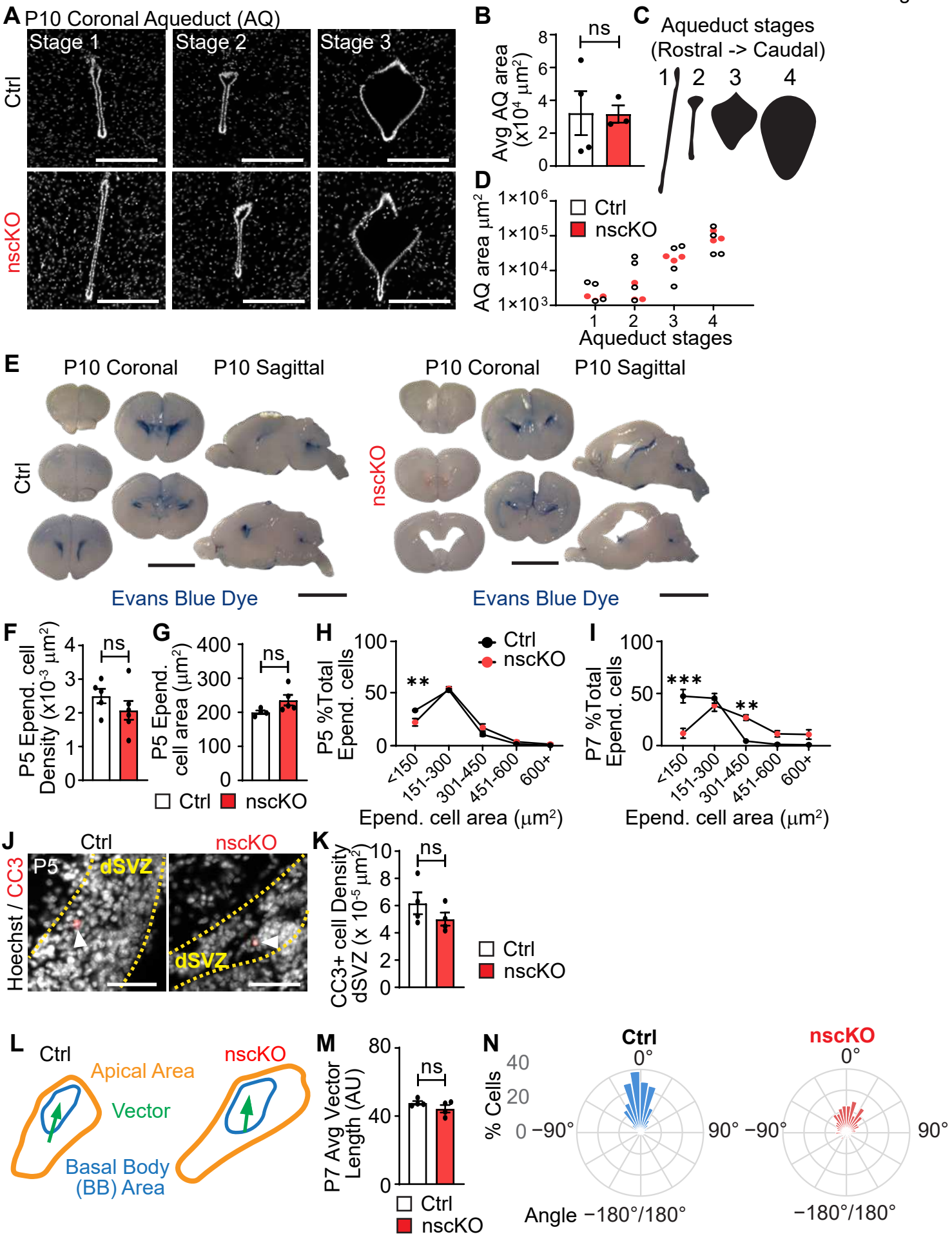
A P10 Coronal Aqueduct (AQ)
Stage 1
Stage 2
Stage 3
Ctrl
nscKO
B
ns
Avg AQ area (x10⁴ µm²)
C
Aqueduct stages (Rostral -> Caudal)
1 2 3 4
D
AQ area µm²
Ctrl
nscKO
Aqueduct stages
E
P10 Coronal
P10 Sagittal
Ctrl
nscKO
Evans Blue Dye
F
P5 Epend. cell Density (x10⁻³ µm²)
G
P5 Epend. cell area (µm²)
H
P5 %Total Epend. cells
Epend. cell area (µm²)
I
P7 %Total Epend. cells
J
Hoechst / CC3
P5
dSVZ
K
CC3+ cell Density dSVZ (x 10⁻⁵ µm²)
L
Apical Area
Vector
Basal Body (BB) Area
M
P7 Avg Vector Length (AU)
N
% Cells
Angle −180°/180°

Supplementary Figure S2. Ankrd11^{nscKO} brains do not exhibit aqueduct stenosis, gross BBB changes or increased cell death. ***Please see associated Fig. 2.*** **A)** Representative images of the P10 cerebral aqueduct (AQ) from Ankrd11^{Ctrl} and Ankrd11^{nscKO} mice stained for Hoechst (grey). **B)** Quantification of AQ area shown in (A). **C)** Schematic of AQ shape from rostral to caudal AQ, labeled by stage at the top. **D)** Quantification of AQ area separated by stage shown in (C). **E)** Representative images of P10 Ankrd11^{Ctrl} and Ankrd11^{nscKO} coronal and sagittal brain sections after transcardiac perfusion with Evans blue dye. **F-G)** Quantification of ependymal cell density **(F)** and ependymal cell area **(G)** from P5 LV whole mount. **H-I)** Proportion of P5 (**H**) and P7 (**I**) ependymal cells binned by area. **J)** Representative images of the P5 rostral dorsal SVZ (dSVZ) from Ankrd11^{Ctrl} and Ankrd11^{nscKO} mice immunostained for CC3 (cleaved caspase 3; red) and counterstained with Hoechst (grey). Yellow dashed line indicates borders of dorsal SVZ. Arrowheads indicate CC3-positive cells. **K)** Quantification of (J). **L)** Schematic of binary outline showing apical area (orange), BB area (blue), and PCP vector (green arrow) for one Ankrd11^{Ctrl} and one Ankrd11^{nscKO} ependymal cell. **M)** Quantification P7 average vector length from center of BB patch to center of apical ependymal cell. Each dot represents the average for an individual animal. **N)** Polar histogram of the proportion of ependymal cells with binned BB patch angle relative of the average vector angle (=0°). BB patch angles measured from immunostained lateral ventricle wall whole mounts of P7 Ankrd11^{Ctrl} and Ankrd11^{nscKO} mice (see Fig. 2). n=4 mice per genotype from at least two independent litters. Error bars represent SEM. Data were analyzed using unpaired t-tests (B, F, G, K, M) and two-way ANOVA with Sidak's multiple comparison test (D, H, I). **p<0.01, ***p<0.001. ns=not significant. Scale bars represent 50 μm (J), 200 μm (A), and 200 mm (E). Avg=average, AQ=aqueduct, BB=basal body, BBB = blood brain barrier, E=embryonic day, D-SVZ=dorsal subventricular zone, P=postnatal day, TMX=tamoxifen.

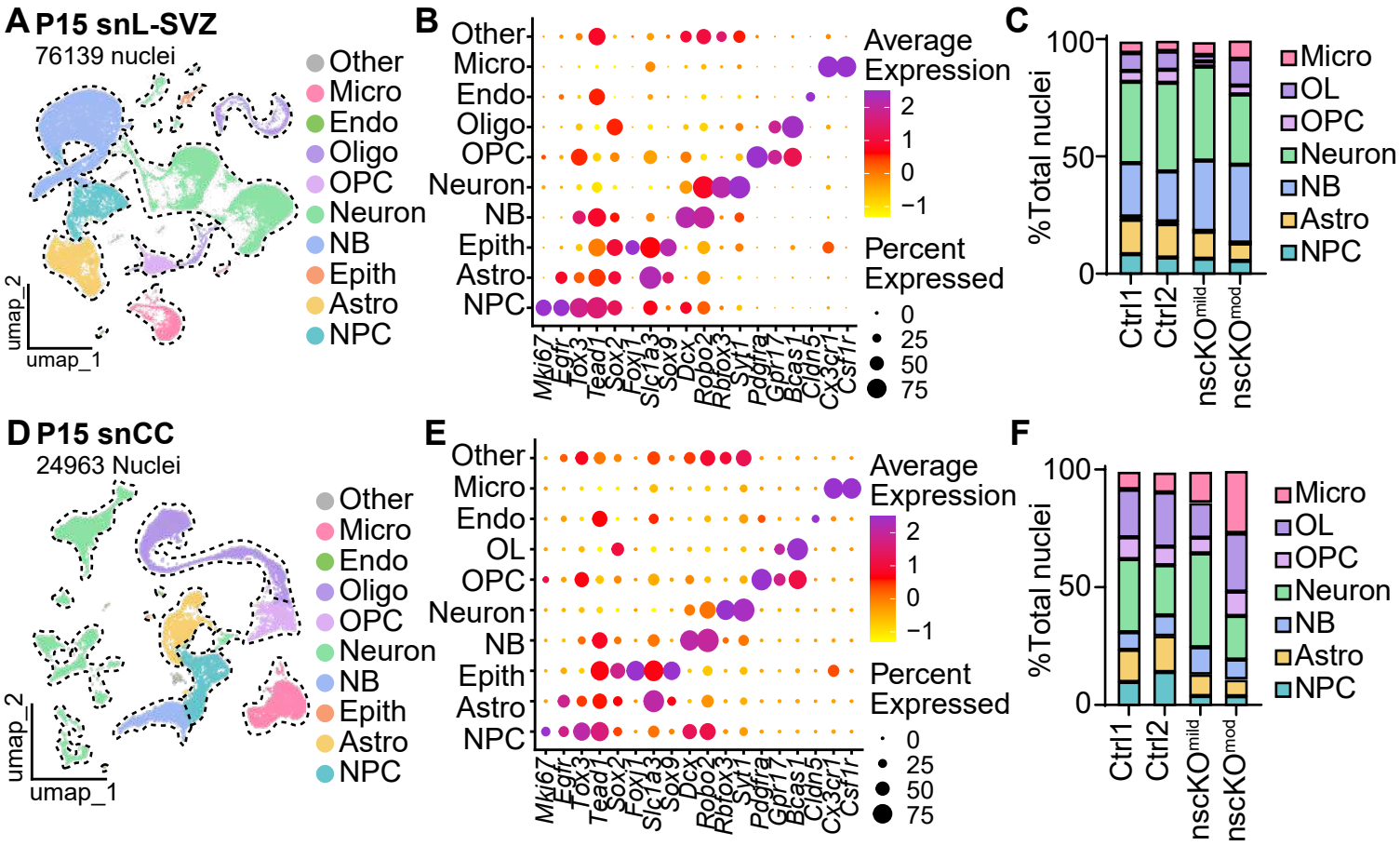
A P15 snL-SVZ
76139 nuclei
Other
Micro
Endo
Oligo
OPC
Neuron
NB
Epith
Astro
NPC
umap_2
umap_1
B
Other
Micro
Endo
Oligo
OPC
Neuron
NB
Epith
Astro
NPC
Mki67
Egfr
Fox3
Tead1
Sox2
Foxj1
Slc1a3
Sox9
Dcx
Robo2
Rbfox3
Syt1
Pdgfra
Gpr17
Bcas1
Cldn5
Cx3cr1
Csf1r
Average Expression
2
1
0
−1
Percent Expressed
0
25
50
75
C
%Total nuclei
100
50
0
Micro
OL
OPC
Neuron
NB
Astro
NPC
Ctrl1
Ctrl2
nscKOmild
nscKOmod
D P15 snCC
24963 Nuclei
Other
Micro
Endo
Oligo
OPC
Neuron
NB
Epith
Astro
NPC
umap_2
umap_1
E
Other
Micro
Endo
OL
OPC
Neuron
NB
Epith
Astro
NPC
Mki67
Egfr
Fox3
Tead1
Sox2
Foxj1
Slc1a3
Sox9
Dcx
Robo2
Rbfox3
Syt1
Pdgfra
Gpr17
Bcas1
Cldn5
Cx3cr1
Csf1r
Average Expression
2
1
0
−1
Percent Expressed
0
25
50
75
F
%Total nuclei
100
50
0
Micro
OL
OPC
Neuron
NB
Astro
NPC
Ctrl1
Ctrl2
nscKOmild
nscKOmod

Supplemental Figure S3. snRNA sequencing of periventricular regions reveals differences in NPC and microglia proportions in Ankrd11^{nscKO} mice. ***Please see associated Fig. 2 and Table S1.*** **A)** UMAP of P15 L-SVZ snRNA-seq Seurat clusters, annotated by major cell type categories. **B)** Heatmap dot plot of cell marker gene expression across snL-SVZ clusters. **C)** Relative proportion of snL-SVZ grouped cell type clusters across individual animals. **D)** UMAP of P15 CC snRNA-seq Seurat clusters, annotated by major cell type categories. **E)** Heatmap dot plot of cell marker gene expression across snCC clusters. **F)** Relative proportion of snCC grouped cell type clusters across individual animals. Both datasets are from four mice (two per genotype). None of the Ankrd11^{Ctrl} mice exhibited hydrocephalus, while one Ankrd11^{nscKO} mouse exhibited mild (n=1) and one mouse Ankrd11^{nscKO} exhibited moderate (n=1) hydrocephalus in each dataset. Astro=astrocyte, CC=corpus callosum, Endo=endothelial cells, Epith=epithelial cell, L-SVZ=lateral subventricular zone, Micro=microglia, NB=neuroblast, NPC=neural precursor cell, NS=neurospheres, Oligo=oligodendrocyte, OPC=oligodendrocyte progenitor cells, P=postnatal day, snRNA-seq=single nucleus RNA sequencing.

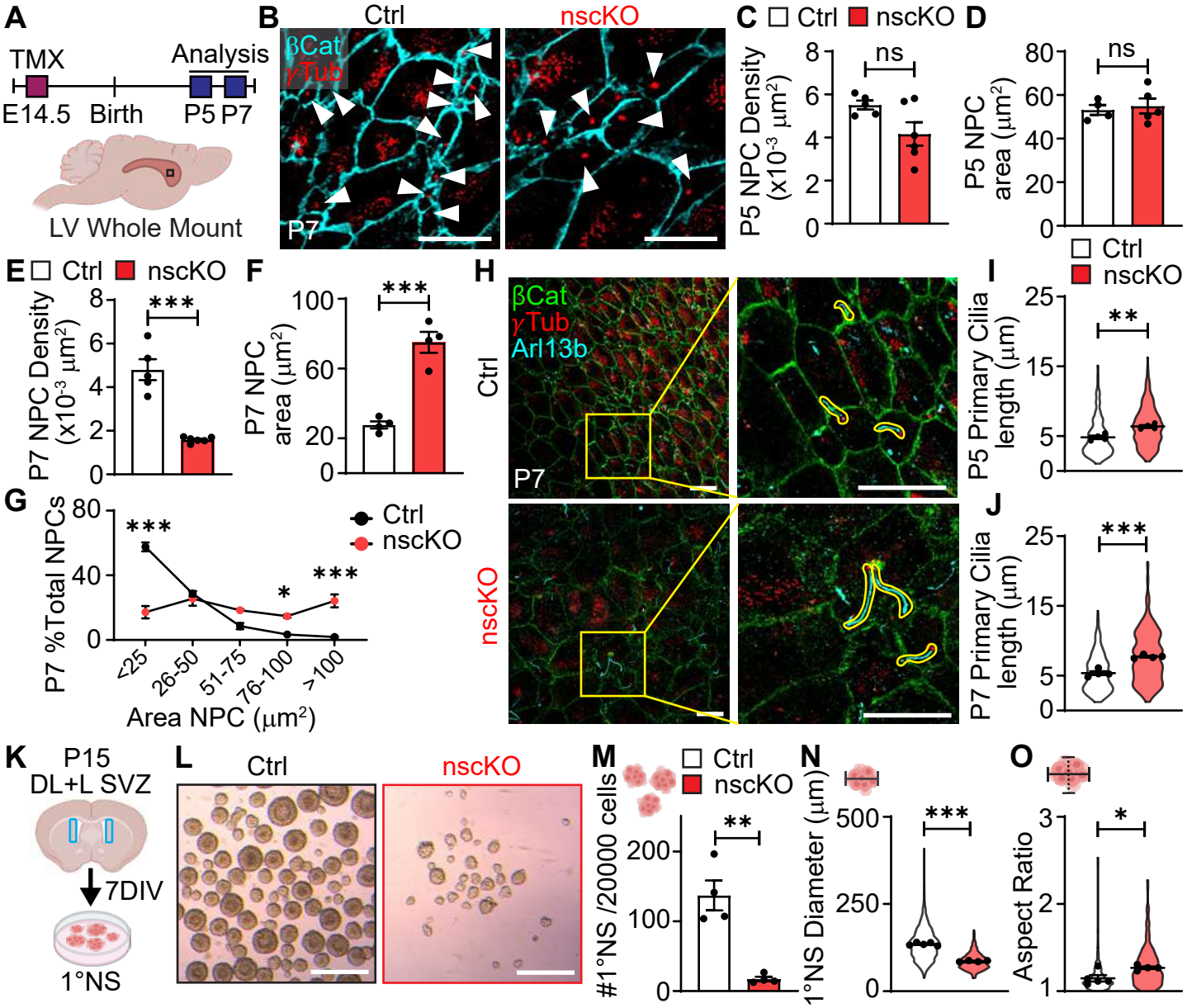
A
TMX
Analysis
E14.5
Birth
P5 P7
LV Whole Mount
B
Ctrl
nscKO
βCat
γTub
P7
C
Ctrl
nscKO
P5 NPC Density (x10-3 µm2)
ns
D
P5 NPC area (µm2)
ns
E
Ctrl
nscKO
P7 NPC Density (x10-3 µm2)
***
F
P7 NPC area (µm2)
***
G
P7 %Total NPCs
Ctrl
nscKO
***
*
***
<25
26-50
51-75
76-100
>100
Area NPC (µm2)
H
Ctrl
nscKO
βCat
γTub
Arl13b
P7
I
Ctrl
nscKO
P5 Primary Cilia length (µm)
**
J
P7 Primary Cilia length (µm)
***
K
P15
DL+L SVZ
7DIV
1°NS
L
Ctrl
nscKO
M
Ctrl
nscKO
#1°NS /20000 cells
**
N
1°NS Diameter (µm)
***
O
Aspect Ratio
*

Figure 3. Loss of Ankrd11 in E14.5 NPCs results in abnormal postnatal SVZ NPC density and ciliogenesis. A) Schematic of experimental design. TMX was injected at E14.5. Lateral ventricle (LV) wall whole mount (dark pink area) was microdissected from Ankrd11^{Ctrl} and Ankrd11^{nscKO} pups at P5 and P7. Box indicates approximate location of representative images. **B)** Representative images of P7 LV whole mount immunostained for βcat (cyan) and γTub (red). Arrowheads point to NPCs, identified by single γTub puncta. **C-F)** Quantification of NPC density **(C, E)** and NPC area **(D, F)** in P5 (**C-D**) and P7 (**E-F**) LV whole mount. **G)** Proportion of P7 NPCs binned by area. **H)** Representative image of P7 LV whole mount immunostained for βcat (green), γTub (red), and Arl13b (cyan). Yellow box indicates cropped panel shown on the right. Yellow outline indicates individual primary cilia identified by γTub (cilium base) and Arl13b (ciliary axoneme) signal. **I-J)** Quantification of primary cilium length from P5 **(I)** and P7 **(J)** LV whole mount, shown in (H). Violin plots represent data from all primary cilia analyzed, and circles indicate averages from each animal. **K)** Schematic of experimental design. NPCs from P15 Ankrd11^{Ctrl} and Ankrd11^{nscKO} dorsolateral (DL) and lateral (L) SVZ were cultured as primary neurospheres (1°NS) for 7 days *in vitro* (DIV). **L)** Representative images of 7DIV 1°NS cultured from Ankrd11^{Ctrl} and Ankrd11^{nscKO} DL+L SVZ. **M-O)** Quantification of 1°NS number (**M**), diameter (**N**), and aspect ratio (**O**) from (L). n ≥4 mice per genotype from at least two independent litters for panels A-O and n=2 mice per genotype from at least two independent litters for panels P-Q. Data were analyzed using unpaired t-test (C-F, I, J, M-O) or one-way ANOVA with Tukey's multiple comparisons post hoc test (G). *p<0.05, **p<0.01, ***p<0.001. ns=not significant. Scale bars represent 15 μm (B, H, and L), 20 μm (H crop box). DIV=days *in vitro*, E=embryonic day, LV=lateral ventricle, NPC=neural progenitor cell, NS=neurosphere, P=postnatal day, SVZ=subventricular zone, TMX=tamoxifen, VZ=ventricular zone.

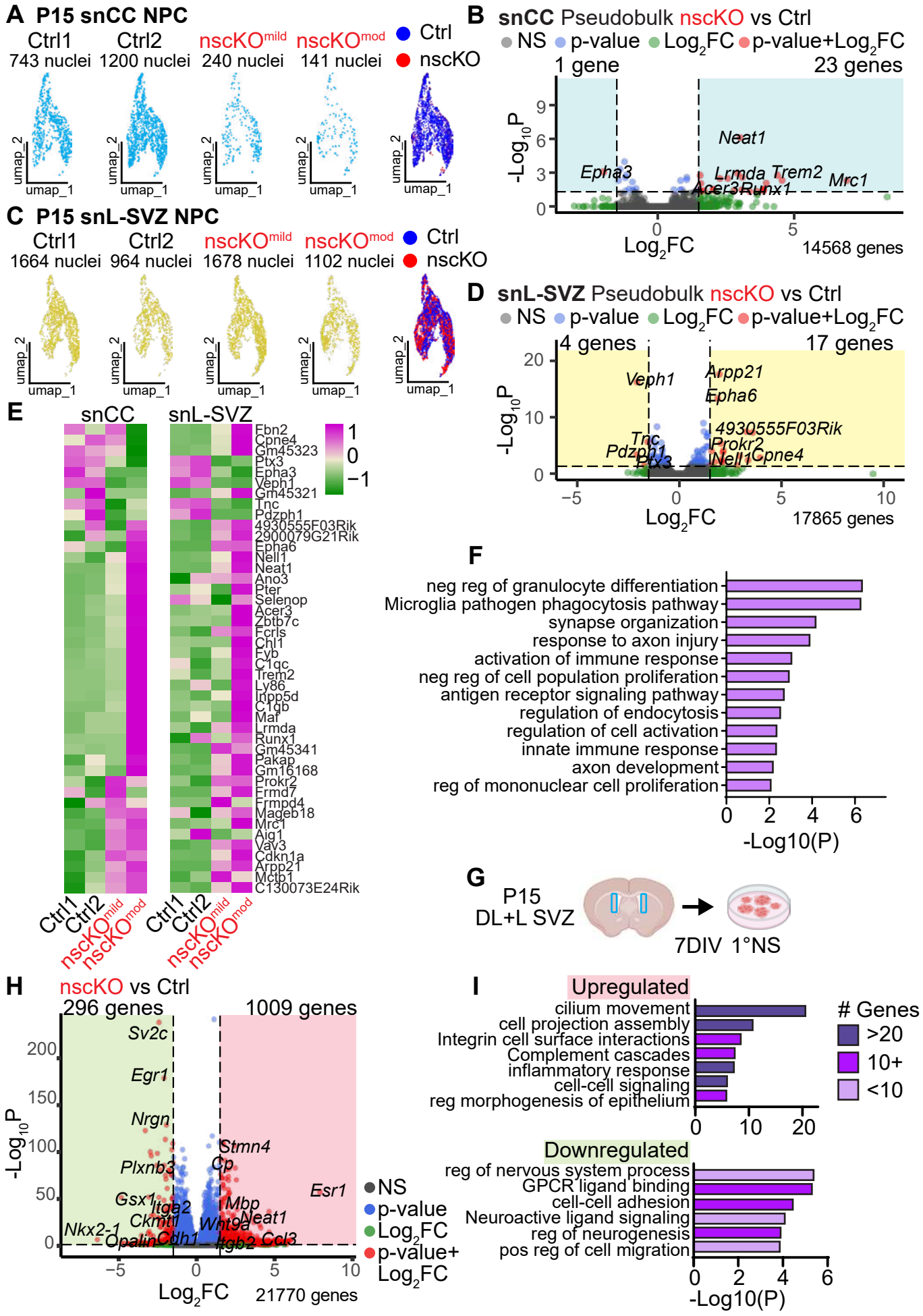
A P15 snCC NPC
Ctrl1
743 nuclei
Ctrl2
1200 nuclei
nscKO^mild
240 nuclei
nscKO^mod
141 nuclei
Ctrl
nscKO
umap_1
umap_2
B snCC Pseudobulk nscKO vs Ctrl
NS p-value Log2FC p-value+Log2FC
1 gene
23 genes
-Log10P
Log2FC
14568 genes
Epha3
Neat1
Lrmda
Trem2
Acer3
Runx1
Mrc1
C P15 snL-SVZ NPC
Ctrl1
1664 nuclei
Ctrl2
964 nuclei
nscKO^mild
1678 nuclei
nscKO^mod
1102 nuclei
Ctrl
nscKO
D snL-SVZ Pseudobulk nscKO vs Ctrl
NS p-value Log2FC p-value+Log2FC
4 genes
17 genes
-Log10P
Log2FC
17865 genes
Veph1
Arpp21
Epha6
4930555F03Rik
Prokr2
Tnc
Pdzph1
Ptx3
Nell1
Cpne4
E
snCC
snL-SVZ
Fbn2
Cpne4
Gm45323
Ptx3
Epha3
Veph1
Gm45321
Tnc
Pdzph1
4930555F03Rik
2900079G21Rik
Epha6
Nell1
Neat1
Ano3
Pter
Selenop
Acer3
Zbtb7c
Fcrls
Chl1
Fyb
C1qc
Trem2
Ly86
Inpp5d
C1qb
Maf
Lrmda
Runx1
Gm45341
Pakap
Gm16168
Prokr2
Frmd7
Frmpd4
Mageb18
Mrc1
Aig1
Vav3
Cdkn1a
Arpp21
Mctp1
C130073E24Rik
1
0
−1
Ctrl1
Ctrl2
nscKO^mild
nscKO^mod
F
neg reg of granulocyte differentiation
Microglia pathogen phagocytosis pathway
synapse organization
response to axon injury
activation of immune response
neg reg of cell population proliferation
antigen receptor signaling pathway
regulation of endocytosis
regulation of cell activation
innate immune response
axon development
reg of mononuclear cell proliferation
-Log10(P)
G
P15
DL+L SVZ
7DIV 1°NS
H
nscKO vs Ctrl
296 genes
1009 genes
-Log10P
Log2FC
21770 genes
Sv2c
Egr1
Nrgn
Stmn4
Cp
Plxnb3
Esr1
Gsx1
Itga2
Mbp
Ckmt1
Wnt9a
Neat1
Nkx2-1
Opalin
Cdh1
Itgb2
Ccl3
NS
p-value
Log2FC
p-value+
Log2FC
I
Upregulated
cilium movement
cell projection assembly
Integrin cell surface interactions
Complement cascades
inflammatory response
cell-cell signaling
reg morphogenesis of epithelium
Genes
>20
10+
<10
Downregulated
reg of nervous system process
GPCR ligand binding
cell-cell adhesion
Neuroactive ligand signaling
reg of neurogenesis
pos reg of cell migration
-Log10(P)

Figure 4. Ankrd11-deficient SVZ NPCs aberrantly express immune related genes. ***Please see associated Figs. S3, S4, and Tables S2-S3*****. A)** UMAPs of NPC subcluster from P15 snCC, split by animal and false coloured by genotype (far right plot), with Ankrd11^{Ctrl} nuclei in blue and Ankrd11^{nscKO} nuclei in red. **B)** Volcano plot of pseudobulk DEGs in Ankrd11^{nscKO} vs Ankrd11^{Ctrl} snCC NPC nuclei (red dots: padj≤0.05 Log2FC |1.5|; blue box = genes for GO analysis). **C)** UMAPs of NPC subcluster from P15 snL-SVZ, split by animal and false coloured by genotype (far right plot) with Ankrd11^{Ctrl} nuclei in blue and Ankrd11^{nscKO} nuclei in red. **D)** Volcano plot of pseudobulk DEGs in Ankrd11^{nscKO} vs Ankrd11^{Ctrl} snL-SVZ NPC nuclei (red dots: padj≤0.05 Log2FC |1.5|; yellow box = genes for GO analysis). **E-F)** Heatmap of DEGs identified in B and D split by animal for NPCs expression from snCC and snL-SVZ datasets (**E**) and corresponding GO analysis of DEGs (**F**)**.** Both datasets are from four mice (two per genotype). None of the Ankrd11^{Ctrl} mice exhibited hydrocephalus, while one Ankrd11^{nscKO} mouse exhibited mild (n=1) and one mouse Ankrd11^{nscKO} exhibited moderate (n=1) hydrocephalus in each dataset. **G)** Schematic of experimental design. P15 SVZ NPCs from Ankrd11^{Ctrl} and Ankrd11^{nscKO} mice were cultured as primary neurospheres (1°NS) for 7 days in vitro (DIV) and subjected to bulk RNA-sequencing. **H-I)** Volcano plot of DEGs in Ankrd11^{nscKO} vs Ankrd11^{Ctrl} 1°NS bulk RNAseq (**H;** red dots: padj≤0.05 Log2FC |1.5|; red box = upregulated genes and green box = downregulated genes used for GO analysis in (**I**). n=2 mice per genotype from two independent litters for panels A-F and n=4 mice per genotype from two independent litters for panels G-I. CC=corpus callosum, GO=gene ontology, L-SVZ=lateral subventricular zone, P=postnatal day, snRNA-seq=single nucleus RNA sequencing.

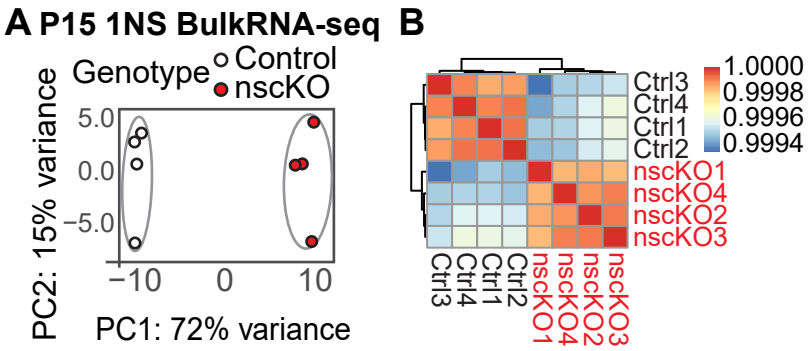
A P15 1NS BulkRNA-seq
Genotype
Control
nscKO
5.0
0.0
−5.0
−10
0
10
PC2: 15% variance
PC1: 72% variance
B
Ctrl3
Ctrl4
Ctrl1
Ctrl2
nscKO1
nscKO4
nscKO2
nscKO3
1.0000
0.9998
0.9996
0.9994

Supplementary Figure S4. Ankrd11^{nscKO} SVZ NPCs are transcriptionally distinct. ***Please see associated Fig. 6.*** **A)** PCA plot of Ankrd11^{Ctrl} and Ankrd11^{nscKO} P15 SVZ NPC primary neurosphere (1°NS) bulk RNA-seq samples. **B)** Correlation heatmap (spearman correlation) between Ankrd11^{Ctrl} and Ankrd11^{nscKO} 1°NS bulk RNA-seq samples. n≥4 mice per genotype from at least two independent litters. Data were analyzed using spearman correlation (B).

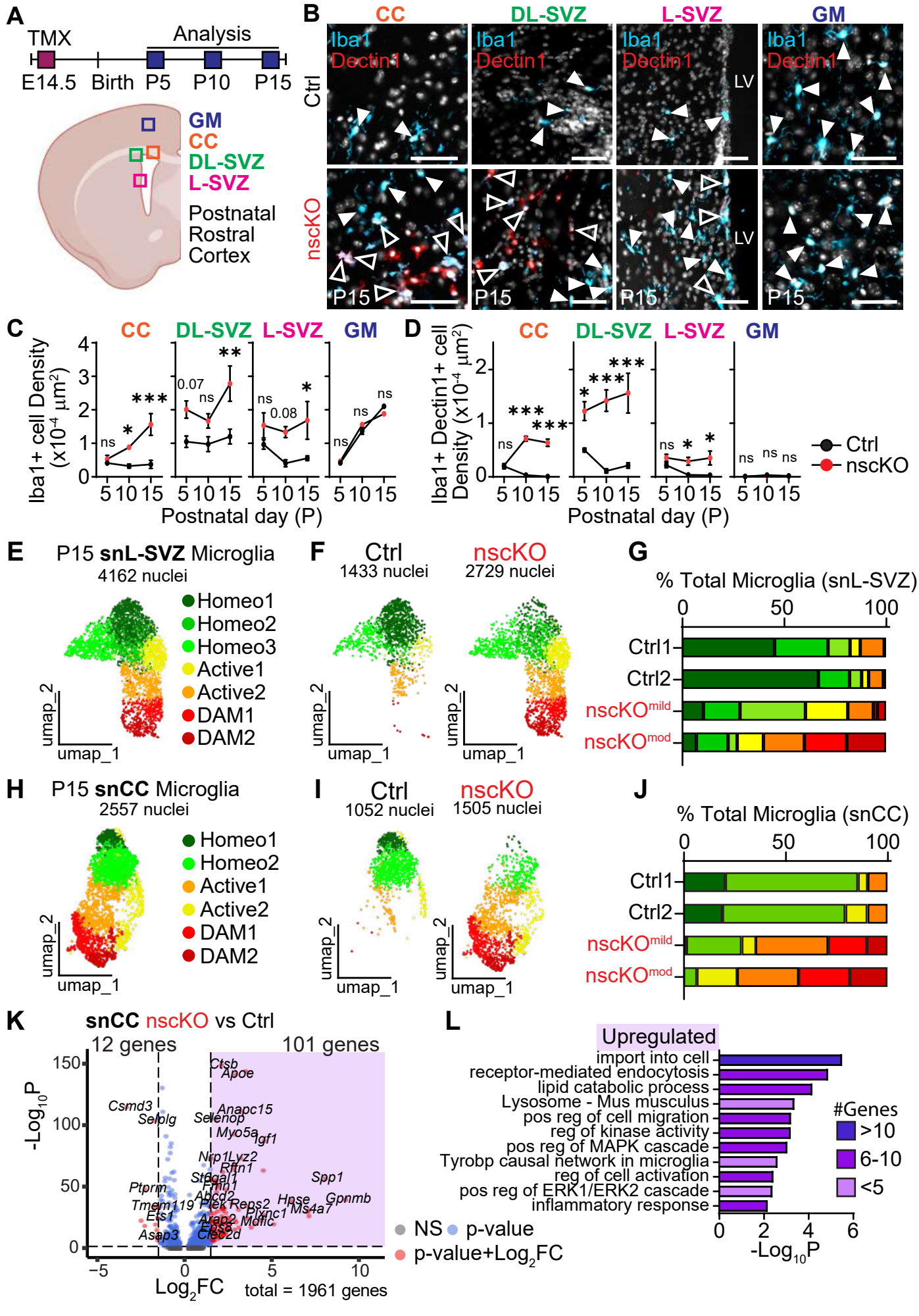
A
TMX
Analysis
E14.5
Birth
P5
P10
P15
GM
CC
DL-SVZ
L-SVZ
Postnatal
Rostral
Cortex
B
CC
DL-SVZ
L-SVZ
GM
Ctrl
nscKO
Iba1
Dectin1
LV
P15
C
Iba1+ cell Density (x10-4 µm2)
Postnatal day (P)
D
Iba1+ Dectin1+ cell Density (x10-4 µm2)
Postnatal day (P)
Ctrl
nscKO
E
P15 snL-SVZ Microglia
4162 nuclei
Homeo1
Homeo2
Homeo3
Active1
Active2
DAM1
DAM2
umap_1
umap_2
F
Ctrl
1433 nuclei
nscKO
2729 nuclei
G
% Total Microglia (snL-SVZ)
Ctrl1
Ctrl2
nscKOmild
nscKOmod
H
P15 snCC Microglia
2557 nuclei
I
Ctrl
1052 nuclei
nscKO
1505 nuclei
J
% Total Microglia (snCC)
K
snCC nscKO vs Ctrl
12 genes
101 genes
-Log10P
Log2FC
total = 1961 genes
NS
p-value
p-value+Log2FC
L
Upregulated
import into cell
receptor-mediated endocytosis
lipid catabolic process
Lysosome - Mus musculus
pos reg of cell migration
reg of kinase activity
pos reg of MAPK cascade
Tyrobp causal network in microglia
reg of cell activation
pos reg of ERK1/ERK2 cascade
inflammatory response
#Genes
>10
6-10
<5
-Log10P

Figure 5. Loss of Ankrd11 in E14.5 NPCs results in periventricular microgliosis, which correlates with age and HC severity. ***Please see associated Fig. S5, Tables S5-S6.*** **A)** Schematic of experimental design. TMX was injected at E14.5. Ankrd11^{Ctrl} and Ankrd11^{nscKO} pups were collected at P5, P10, and P15. Boxes indicate approximate location of representative images in B, with GM in blue, CC in orange, DL-SVZ in green, and L-SVZ in pink. **B)** High magnification representative images of all regions at P15, immunostained for Iba1 (cyan), Dectin1 (red) and Hoechst (grey). Solid arrowheads indicate Iba1+ cells, open arrowheads indicate Iba1+Dectin1+ cells, "LV" indicates lateral ventricle. **C-D)** Quantification of B for Iba1+ (**C**), and Iba1+Dectin1+ (**D**) cell density from all regions at P5, P10, and P15. **E–J)** UMAP of P15 snL-SVZ (**E-G**) and sn-CC (**H-J**) microglia nuclei subcluster (Figs. S3A, S3D, S5A, S5D) shown aggregated with cluster labels (**E, H**) and split by genotype (Ankrd11^{Ctrl} vs. Ankrd11^{nscKO}) (**F, I**), with cluster proportions per animal relative to total microglia (**G, J**). Both datasets are from four mice (two per genotype). None of the Ankrd11^{Ctrl} mice exhibited hydrocephalus, while one Ankrd11^{nscKO} mouse exhibited mild (n=1) and one mouse Ankrd11^{nscKO} exhibited moderate (n=1) hydrocephalus in each dataset. **K-L)** Volcano plot of DEGs in Ankrd11^{nscKO} vs Ankrd11^{Ctrl} snCC microglia (**K**; red dots: padj≤0.05 Log2FC |1.5|). Purple box = genes used for GO analysis in (**L)**. n≥4 mice per genotype from at least two independent litters for panels A-D and n=2 mice per genotype from two independent litters for panels E-L. Error bars represent SEM. Data were analyzed using Multiple t-tests (C, D). *p<0.05, **p<0.01, ***p<0.001. ns=not significant. Scale bars represent 50 μm (B). Actie=activated microglia, CC=corpus callosum, DAM=disease associated microglia, E=embryonic day, GO=gene ontology, Homeo=homeostatic microglia, LV=lateral ventricle, Mod=moderate, P=postnatal day, snRNA-seq=single nucleus RNA sequencing, TMX=tamoxifen.

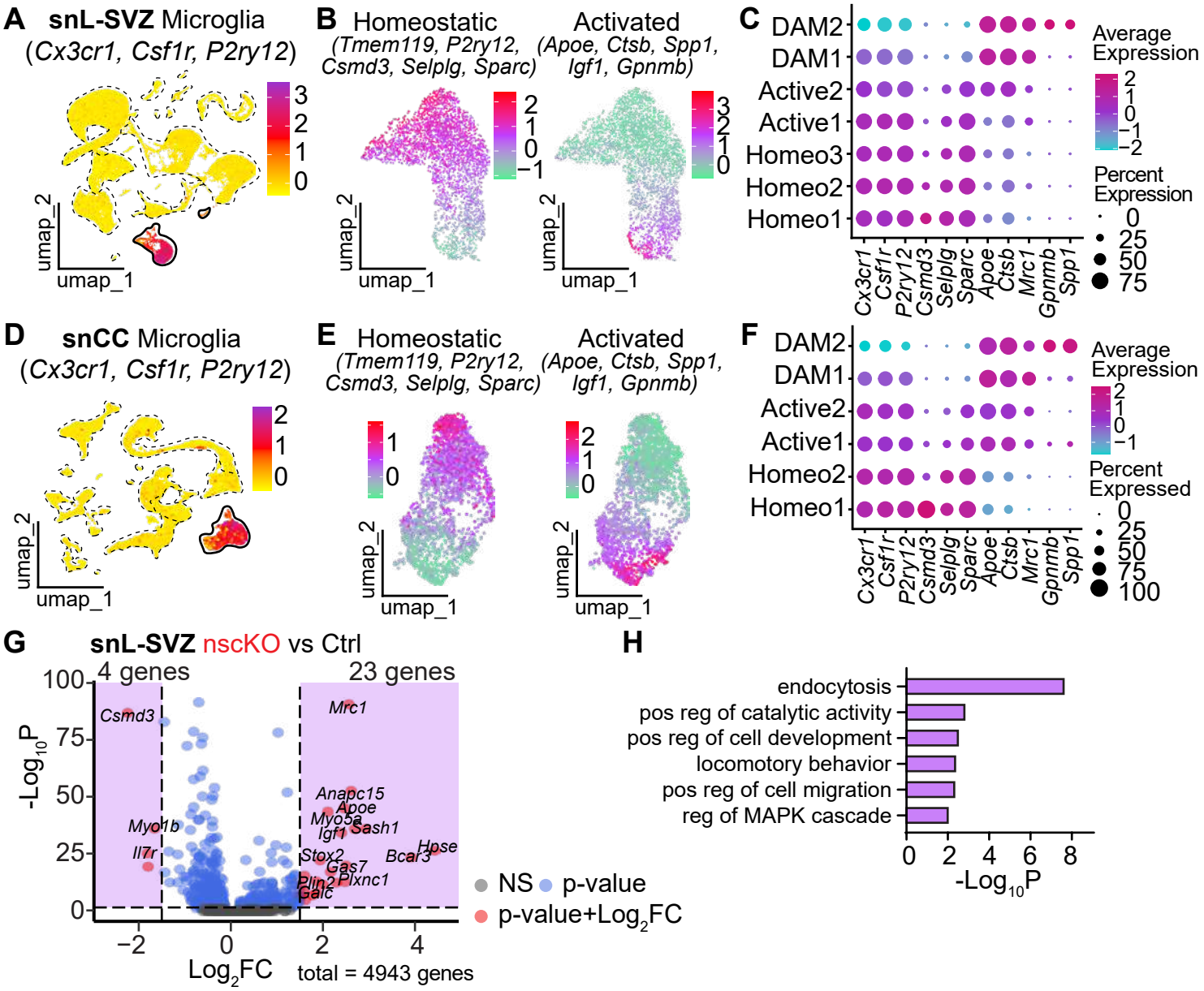
A snL-SVZ Microglia
(Cx3cr1, Csf1r, P2ry12)
B Homeostatic
(Tmem119, P2ry12, Csmd3, Selplg, Sparc)
Activated
(Apoe, Ctsb, Spp1, Igf1, Gpnmb)
C
DAM2
DAM1
Active2
Active1
Homeo3
Homeo2
Homeo1
Cx3cr1 Csf1r P2ry12 Csmd3 Selplg Sparc Apoe Ctsb Mrc1 Gpnmb Spp1
Average Expression
Percent Expression
D snCC Microglia
(Cx3cr1, Csf1r, P2ry12)
E Homeostatic
(Tmem119, P2ry12, Csmd3, Selplg, Sparc)
Activated
(Apoe, Ctsb, Spp1, Igf1, Gpnmb)
F
Average Expression
Percent Expressed
umap_1
umap_2

G snL-SVZ nscKO vs Ctrl
4 genes
23 genes
Csmd3
Mrc1
Anapc15
Apoe
Myo5a
Igf1
Sash1
Myo1b
Il7r
Stox2
Gas7
Bcar3
Hpse
Plin2
Plxnc1
Galc
-Log10P
Log2FC
NS
p-value
p-value+Log2FC
total = 4943 genes

H
endocytosis
pos reg of catalytic activity
pos reg of cell development
locomotory behavior
pos reg of cell migration
reg of MAPK cascade
-Log10P

Supplementary Figure S5. Microglia characterization in snRNA-seq datasets. ***Please see associated Fig. 5, Tables S5-S6*****. A-C)** P15 snL-SVZ UMAP showing FeaturePlot of combined microglia markers (*Cx3cr1, Csf1r, P2ry12*) (**A**), homeostatic and activated microglia genes expressions scores for the subset from (A) (**B**), and a heatmap dot plot of marker expression per cluster (**C**). **D-F)** P15 snCC UMAP showing FeaturePlot of combined microglia markers (*Cx3cr1, Csf1r, P2ry12*) (**D**), homeostatic and activated microglia genes expressions scores for the subset from (D) (**E**), and a heatmap dot plot of marker expression per cluster (**F**). **G-H)** Volcano plot of DEGs in Ankrd11^{nscKO} vs Ankrd11^{Ctrl} snL-SVZ microglia (**G;** red dots: padj≤0.05 Log2FC |1.5|). Purple box = genes used for GO analysis in (**H**). n=2 mice per genotype from two independent litters. Active=activated microglia, CC=corpus callosum, DAM=disease associate microglia, GO=gene ontology, Homeo=homeostatic microglia, L-SVZ=lateral subventricular zone, snRNA-seq=single nucleus RNA sequencing.

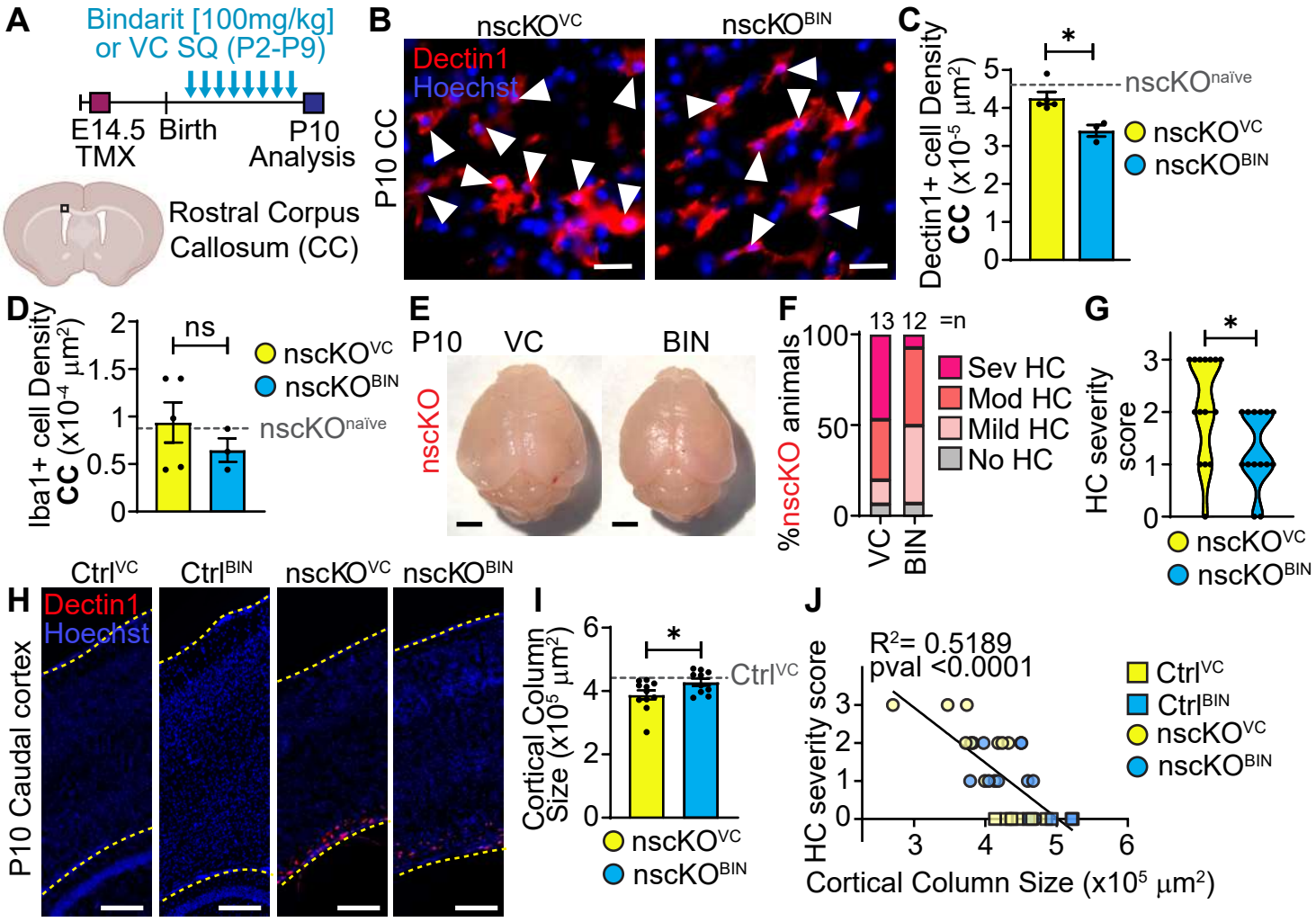
A
Bindarit [100mg/kg] or VC SQ (P2-P9)
E14.5 TMX
Birth
P10 Analysis
Rostral Corpus Callosum (CC)
B
nscKO^VC
nscKO^BIN
Dectin1
Hoechst
P10 CC
C
Dectin1+ cell Density CC (x10^-5 µm^2)
nscKO^naïve
nscKO^VC
nscKO^BIN
D
Iba1+ cell Density CC (x10^-4 µm^2)
ns
E
P10
VC
BIN
nscKO
F
%nscKO animals
13 12 =n
Sev HC
Mod HC
Mild HC
No HC
VC
BIN
G
HC severity score
H
Ctrl^VC
Ctrl^BIN
nscKO^VC
nscKO^BIN
Dectin1
Hoechst
P10 Caudal cortex
I
Cortical Column Size (x10^5 µm^2)
Ctrl^VC
J
R^2= 0.5189
pval <0.0001
HC severity score
Cortical Column Size (x10^5 µm^2)

Figure 6. Attenuation of microglia activation with bindarit reduces hydrocephalus severity in Ankrd11^{nscKO} mice. ***Please see associated Fig. S6.*** **A)** Schematic of experimental design. Dams were injected with TMX at E14.5. Resulting Ankrd11^{Ctrl} and Ankrd11^{nscKO} pups were injected subcutaneously daily with bindarit ([BIN] 100mg/kg) or vehicle-control (VC) from P2-9 and collected at P10. Box indicates approximate location of representative images in B. **B)** High magnification representative images of P10 rostral CC from Ankrd11^{nscKO} mice treated with BIN or VC, immunostained for Dectin1 (red) and counterstained with Hoechst (blue). Arrowheads indicate Dectin1+ cells. **C-D)** Quantification of Dectin1+ (**C**) and Iba1+ (**D**) cell density in Ankrd11^{nscKO} mice treated with BIN or VC. Grey dashed line indicates average marker+ cells in naïve Ankrd11^{nscKO} mice. **E)** Representative pictures of P10 Ankrd11^{nscKO} brains treated with VC or BIN. **F)** Proportion of hydrocephalus severity in BIN or VC treated Ankrd11^{nscKO} mice at P10. Number of mice for each condition is indicated at the top of the graph. **G)** Quantification of hydrocephalus (HC) severity score in Ankrd11^{nscKO} mice treated with BIN or VC, in which no HC = 0, mild HC = 1, moderate HC = 2 and severe HC = 3. **H)** Representative images of P10 caudal cortex from Ankrd11^{Ctrl} and Ankrd11^{nscKO} mice treated with BIN or VC, immunostained for Dectin1 (red) and counterstained with Hoechst (blue). Yellow dashed lines indicate borders of the caudal cortex. **I)** Quantification of cortical column size, as shown in (H), of Ankrd11^{nscKO} P10 mice treated with BIN and VC. Dashed line indicates area of Ankrd11^{Ctrl} caudal cortex after treatment with VC. **J)** Correlation plot between caudal cortical column size and HC severity score of P10 Ankrd11^{Ctrl} and Ankrd11^{nscKO} mice treated with BIN and VC. n≥3 mice per genotype from at least two independent litters. Error bars represent SEM. Data were analyzed using unpaired t-test (C, D, I), linear regression (J), Mann Whitney (G). *p<0.05, **p<0.01, ***p<0.001. ns=not significant. Scale bars represent 20 μm (B), 200 μm (H), and 2mm (E). BIN=Bindarit, CC=corpus callosum, E=embryonic day, GM=grey matter, HC=hydrocephalus, LV=lateral ventricle, P=postnatal day, SQ=subcutaneous, TMX=tamoxifen, VC=vehicle control.

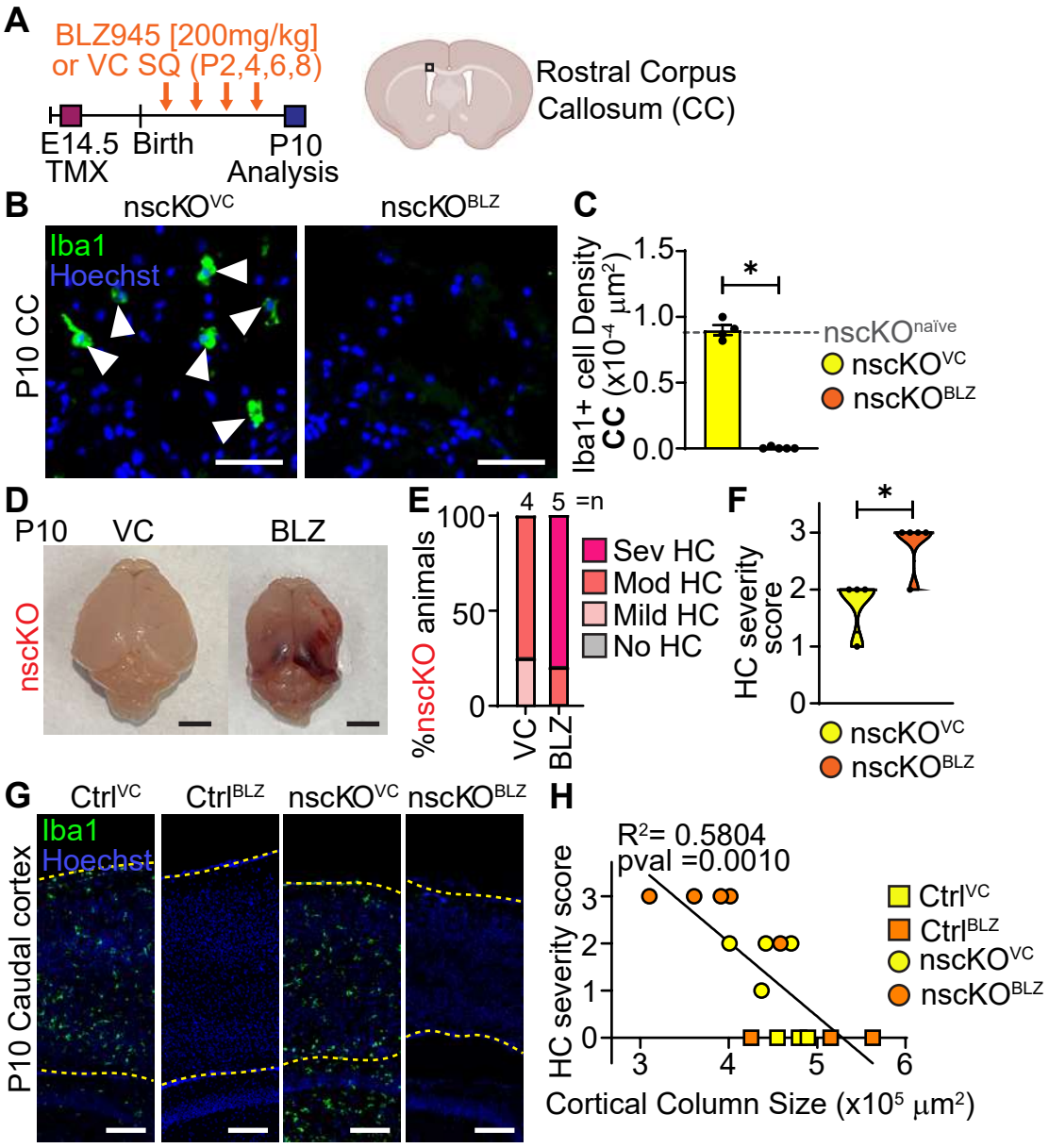
A
BLZ945 [200mg/kg]
or VC SQ (P2,4,6,8)
E14.5 TMX
Birth
P10 Analysis
Rostral Corpus Callosum (CC)
B
nscKO^VC
nscKO^BLZ
Iba1
Hoechst
P10 CC
C
Iba1+ cell Density CC (x10^-4 µm^2)
nscKO^naïve
nscKO^VC
nscKO^BLZ
D
P10
VC
BLZ
nscKO
E
%nscKO animals
4 5 =n
Sev HC
Mod HC
Mild HC
No HC
VC
BLZ
F
HC severity score
nscKO^VC
nscKO^BLZ
G
Ctrl^VC
Ctrl^BLZ
nscKO^VC
nscKO^BLZ
Iba1
Hoechst
P10 Caudal cortex
H
R²= 0.5804
pval =0.0010
HC severity score
Cortical Column Size (x10^5 µm²)
Ctrl^VC
Ctrl^BLZ
nscKO^VC
nscKO^BLZ

Supplementary Figure S6. Ablation of microglia with BLZ945 worsens hydrocephalus severity in Ankrd11^{nscKO} mice. ***Please see associated Fig. 6.*** **A)** Schematic of experimental design. Dams were injected with TMX at E14.5. Resulting Ankrd11^{Ctrl} and Ankrd11^{nscKO} pups were injected subcutaneously with BLZ945 ([BLZ] 200mg/kg) or vehicle-control (VC) at P2,4,6,8 and collected at P10. Box indicates approximate location of representative images in B. **B)** High magnification representative images of P10 rostral CC from Ankrd11^{nscKO} mice treated with VC or BLZ, immunostained for Iba1 (green) and counterstained with Hoechst (blue). Arrowheads indicate Iba1+ cells. **C)** Quantification of Iba1+ cell density in Ankrd11^{nscKO} mice treated with VC or BLZ. Grey dashed line indicates average marker+ cells in naïve Ankrd11^{nscKO} mice. **D)** Representative pictures of P10 Ankrd11^{nscKO} brains treated with VC or BLZ. **E)** Proportion of hydrocephalus severity in VC or BLZ treated Ankrd11^{nscKO} mice at P10. Number of Ankrd11^{nscKO} mice for each condition is indicated at the top of the graph. **F)** Quantification of HC severity score between Ankrd11^{nscKO} treated with VC or BLZ, in which no HC = 0, mild HC = 1, moderate HC = 2 and severe HC = 3. **G)** Representative images of P10 caudal cortex from Ankrd11^{Ctrl} and Ankrd11^{nscKO} mice treated with BLZ or VC, immunostained for Iba1 (green) and counterstained with Hoechst (blue). Yellow dashed lines indicate borders of the caudal cortex. **H)** Correlation plot between cortical column size and HC severity score of P10 Ankrd11^{Ctrl} and Ankrd11^{nscKO} mice treated with VC or BLZ. n≥4 mice per genotype from at least two independent litters. Error bars represent SEM. Data were analyzed using one-way ANOVA with Sidak's multiple comparison test (C), Mann Whitney (F), linear regression (H). *p<0.05, **p<0.01, ***p<0.001. ns=not significant. Scale bars represent 50 μm (B), 200 μm (G) and 2mm (D). BLZ=BLZ945, CC=corpus callosum, E=embryonic day, GM=grey matter, HC=hydrocephalus, LV=lateral ventricle, P=postnatal day, SQ=subcutaneous, TMX=tamoxifen, VC=vehicle control.

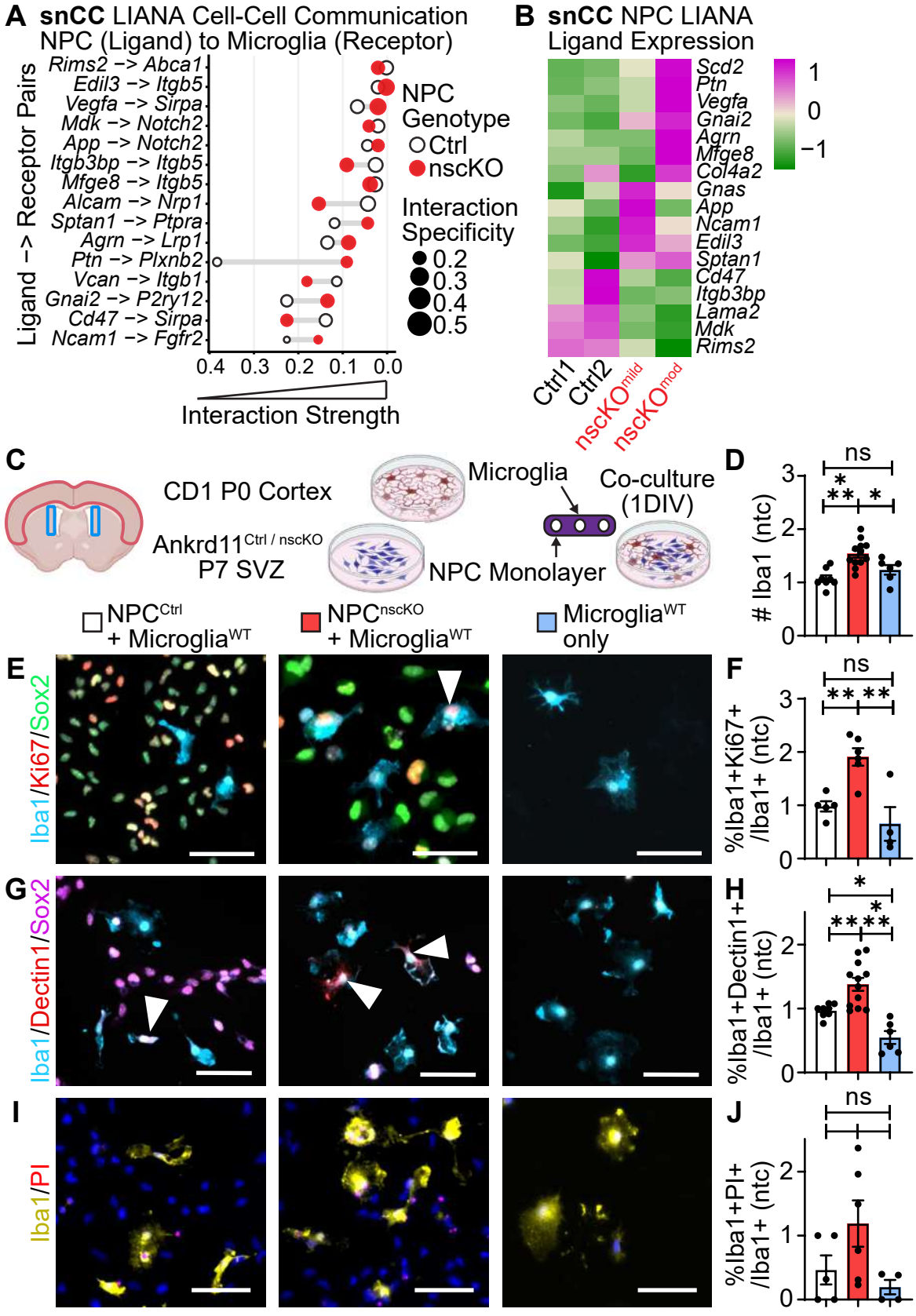
A snCC LIANA Cell-Cell Communication
NPC (Ligand) to Microglia (Receptor)
Ligand -> Receptor Pairs
Rims2 -> Abca1
Edil3 -> Itgb5
Vegfa -> Sirpa
Mdk -> Notch2
App -> Notch2
Itgb3bp -> Itgb5
Mfge8 -> Itgb5
Alcam -> Nrp1
Sptan1 -> Ptpra
Agrn -> Lrp1
Ptn -> Plxnb2
Vcan -> Itgb1
Gnai2 -> P2ry12
Cd47 -> Sirpa
Ncam1 -> Fgfr2
0.4 0.3 0.2 0.1 0.0
Interaction Strength
NPC Genotype
Ctrl
nscKO
Interaction Specificity
0.2
0.3
0.4
0.5
B snCC NPC LIANA
Ligand Expression
Scd2
Ptn
Vegfa
Gnai2
Agrn
Mfge8
Col4a2
Gnas
App
Ncam1
Edil3
Sptan1
Cd47
Itgb3bp
Lama2
Mdk
Rims2
1
0
−1
Ctrl1
Ctrl2
nscKOmild
nscKOmod
C
CD1 P0 Cortex
Ankrd11Ctrl / nscKO
P7 SVZ
Microglia
Co-culture
(1DIV)
NPC Monolayer
NPCCtrl
+ MicrogliaWT
NPCnscKO
+ MicrogliaWT
MicrogliaWT
only
D
Iba1 (ntc)
ns
E
Iba1/Ki67/Sox2
F
%Iba1+Ki67+
/Iba1+ (ntc)
G
Iba1/Dectin1/Sox2
H
%Iba1+Dectin1+
/Iba1+ (ntc)
I
Iba1/PI
J
%Iba1+PI+
/Iba1+ (ntc)

Figure 7. Ankrd11-deficient SVZ NPCs increase microglia proliferation and activation *in vitro*. *Please see associated Table S7.* **A)** Dumbbell coordinate plot of the top 15 SVZ NPC-to-microglia ligand–receptor interactions predicted by LIANA. Ligands are expressed by the source cell (P15 snCC SVZ NPCs Ankrd11^{Ctrl} or Ankrd11^{nscKO}), and the receptors are expressed by the target cell (P15 snCC combined microglia from both genotypes). Interaction strength indicates consensus value or LIANA aggregate rank; lower value equals higher ranked interactions. Colours indicate genotype of source cell, and size of circle indicates interaction specificity. Ligand-receptor pairs are shown on the left. Full list of ligand-receptor pairs in Table S7. **B)** Heatmap of average gene expression in snCC SVZ NPCs from (A) per animal. **C)** Schematic of experimental design. NPCs were cultured from P7 Ankrd11^{Ctrl} and Ankrd11^{nscKO} SVZ tissue (blue) as primary neurospheres (1°NS) for 6 days *in vitro* (DIV). 1°NS were then plated as monolayers for 1DIV. Microglia were cultured from P0 CD1 (WT) cortex (red) and maintained for 14 DIV. At 14 DIV, microglia were isolated and plated on top of NPC monolayer. NPCs and microglia were co-cultured for 24h. **D)** Quantification of average number of Iba1+ cells. **E, G, I)** Representative images of NPC-microglia co-cultures immunostained for Iba1 (cyan), Ki67 (red), Sox2 (green) (**E**), Iba1 (cyan), Dectin1 (red), Sox2 (Pink) (**G**) or Iba1 (yellow) (**I**). Live cultures in I were also stained with propidium iodide (PI; red) to detect cell death (**I;** please see materials and methods for more details). Cells in all images are counterstained with Hoechst in grey (**E, G**) or blue (**I**). Arrowheads indicate Iba1+marker+ cells. **F)** Proportion of Iba1+Ki67+ cells (% Iba1+Ki67/Iba1+ cells) from E. **H**) Proportion of Iba1+Dectin1+ cells (% Iba1+Dectin1+/Iba1+ cells) from G. **J**) Proportion of Iba1+PI+ cells (% Iba1+PI+/Iba1+ cells) from I. Data were normalized to control (ntc; Ankrd11^{Ctrl} + microglia^{WT}). n≥4 mice per genotype from at least two independent litters, except for panels A-E from P15 snCC (n=2 per genotype). Error bars represent SEM. Data were analyzed using one-way ANOVA Tukey's multiple comparisons post hoc test (D, F, H) and Kruskal-Wallis test (J). *p<0.05, **p<0.01, ***p<0.001. Scale bars represent 50 μm (E, G, I) CC=corpus callosum, DIV=days *in vitro*, L-SVZ=lateral subventricular zone, Mod=moderate, NPC=neural progenitor cell, NS=neurosphere, NPC=neural precursor cell, ntc=normalized to control, P=postnatal day, snRNA-seq=single nucleus RNA sequencing, TM=tamoxifen, WT=wild type.

Supplementary Files

This is a list of supplementary files associated with this preprint. Click to download.

- TableS7.P15snCCLIANANPCMicroglia.xlsx
- TableS2.P15NPCsnCCDEGnscKOCtrl.xlsx
- DataAccess.docx
- TableS3.P15NPCsnLSVZDEGnscKOCtrl.xlsx
- TableS1.P15EpendsnLSVZDEGnscKOCtrl.xlsx
- TableS6.P15MicrosnLSVZDEGnscKOCtrl.xlsx
- TableS5.P15MicrosnCCDEGnscKOCtrl.xlsx
- TableS4.P151NSBulkDEGnscKOCtrl.xlsx
- VideoS1Ctrl.avi
- VideoS2nscKO.avi